On the Scalability Limits of Communication Networks to the Nanoscale

Ignacio Llatser Martí

Nanonetworking Center in Catalunya

Universitat Politècnica de Catalunya

Advisors:

Dr. Eduard Alarcón

Dr. Albert Cabellos-Aparicio

A thesis submitted for the degree of

Doctor of Philosophy in Computer Architecture

October 31, 2013

to my parents, and to my brother Franc

Acknowledgements

Finding myself about to write the acknowledgements of this thesis, I just realize that my PhD is about to come to an end. It is now time to thank the many people who have accompanied me through this long and fruitful journey. First and foremost, I would like to express my deep and sincere gratitude to my extraordinary thesis advisors, Dr. Eduard Alarcón and Dr. Albert Cabellos-Aparicio. Their profound dedication and tireless work shaped this PhD thesis and inspired me throughout its development. Whenever I felt lost, their wise guidance served as a lighthouse that pointed me to the right direction. I consider myself extremely lucky to have had such excellent advisors of my PhD thesis.

Right before starting my PhD, I was in a sea of doubts about my future. I am very grateful to Dr. Josep Solé-Pareta for having invited me —already 4.5 years ago— to join his newly founded research group N3Cat and having convinced me that becoming a PhD student was the best choice I could make. I have never regretted this life-changing decision ever since. I would also like to thank Dr. Josep Solé-Pareta for his support and kindness throughout my stay in his research group.

Although scientific guidance and support are key to a successful PhD, almost as important is financial support. I acknowledge the Technical University of Catalonia for awarding me the FPI-UPC doctoral grant, the Spanish Ministry of Education for the FPU grant, and the State Public Employment Service for the unemployment benefits which allowed me to remain financially independent during my PhD studies. I would also like to thank the research group N3Cat for generously supporting my multiple trips to scientific conferences all over the world.

Naming the main highlights of my PhD is not an easy task, but I would definitely choose my research stays abroad as some of my best memories. I am grateful to Dr. Ian F. Akyildiz for having hosted me twice in his research group BWN at the Georgia Institute of Technology. He gave me interesting ideas and provided useful advice about my research. My kind colleagues at the BWN Lab made me feel welcome from the first day. Special thanks go to Dr. Josep Miquel Jornet and Dr. Massimiliano Pierobon, for the many enlightening research discussions and their help with the practical matters. The Spanish Ministry of Education provided funding, albeit with some delay, for these two research stays.

Cooperation is a key aspect in the world of scientific research. In this sense, I would like to express my sincere appreciation to Dr. Dmitry N. Chigrin for hosting me in his nano-photonics group at the University of Wuppertal and introducing me to the world of surface plasmons. Dr. Dmitry N. Chigrin has proved to be an understanding, supportive and kind mentor. I would also like to thank Dr. Christian Kremers for his scientific assistance and the German Academic Exchange Service (DAAD) for providing financial support for this research stay.

Here I would also like to acknowledge the members who kindly agreed to participate in my thesis examination panel, namely, Dr. Stephan Roche, Dr. Kaushik Chowdhury, Dr. Sasitharan Balasubramaniam, Dr. Ramón Bragós, Dr. Josep Vidal and Dr. David Jiménez. Thank you as well to Dr. Gianluca Reali and Dr. Kaushik Chowdhury for reviewing my thesis as external experts in the topic. They provided feedback in a very short time which contributed to improve the quality of this thesis.

Equally important have been the colleagues with whom I have had the pleasure to share part of this journey. I would particularly like to thank Sergi Abadal, Raül Gómez, Albert Mestres, Nora Garralda and Iñaki Pascual for their invaluable work and the inspiring discussions

about many of the topics contained in this thesis. The help from Florin Coras made completing the doctoral courses so much easier. Thanks to Albert López for being an excellent lab manager, always ready to help and find the best solution for every problem. Finally, Dr. Şükrü Kuran, Deniz Demiray and Luca Felicetti are outstanding students who visited our research group; I have been fortunate to learn from their knowledge and passion for research.

Sailing the sea of life and research is much more enjoyable if one happens to share the voyage with such exceptional friends. I would like to particularly thank Marc Oriol and Cristina Gené for being the most amazing roommates, Laura Vila for her wonderful presents, Eduard Huntingford for his invaluable advice and support and Òscar Senén for all the good moments that we have spent together. I am also incredibly grateful to Luciana Yabar for being my private chauffeur and to Martha Santamaría for her warm hospitality; they both made my stay in Atlanta a memorable one.

Certainly the list of acknowledgements could go on, but one has to stop somewhere. I cannot finish, however, without giving very special thanks to Judyth Luján for making the last part of this adventure even more exciting.

Above all, I want to show my endless love and gratitude to the people who have given me the strength and motivation to undertake the great journey of my PhD. Last, but most certainly not least, a big thank you goes to my parents, my brother Franc and the rest of my family, for their love and unconditional support throughout my life.

Abstract

The rapid progress of nanotechnology in the last decades has allowed the development of integrated nanosystems, capable of interacting at the nanoscale. Despite their unique capabilities, the small operation range of nanosystems limits their usefulness in practical macro-scale scenarios. Nanonetworks, the interconnection of nanosystems, will extend their range of operation by allowing communication among nanosystems, thereby greatly enhancing their potential applications.

An important question in this area concerns how communication networks will scale when their size shrinks. In order to answer this question, this thesis presents a scalability analysis of the performance metrics of communication networks to the nanoscale. The main performance metrics in the two main paradigms which have been proposed to implement nanonetworks, namely, diffusion-based molecular communication and graphene-enabled wireless communications, are identified.

The analyzed performance metrics in nanonetworks show unique scaling trends with respect to traditional wireless communications, thereby confirming the need of novel communication protocols and techniques specifically adapted to nanonetworks. The obtained results provide guidelines that may help researchers to design the future network architecture of nanonetworks.

Contents

Contents vi

List of Figures x

List of Tables xv

Nomenclature xviii

1 Introduction 1

1.1 Background 1

1.1.1 Nanotechnology 1

1.1.2 Nanonetworks 2

1.2 Applications of nanonetworks 3

1.2.1 Wireless Nanosensor Networks 3

1.2.2 Graphene-enabled Wireless Networks-on-Chip 5

1.3 State of the art 7

1.3.1 Molecular communication 7

1.3.2 Graphene-enabled wireless communications 14

1.4 Motivation 20

1.5 Main contributions 22

2 Characterization of the physical channel in diffusion-based molecular communication 26

2.1 Modulation scheme for DMC 27

2.2 Physical channel analysis 30

2.3 Detection methods for DMC with a pulse-based modulation . . . 32

2.4 Amplitude detection 34
2.4.1 Pulse delay 34
2.4.2 Pulse amplitude 35
2.4.3 Pulse width 36
2.5 Energy detection 38
2.5.1 Pulse energy 39
2.5.2 Pulse duration 41
2.6 Scalability of detection techniques in DMC 44
2.7 Summary and concluding remarks 48

3 Diffusion-based molecular communication networks 49
3.1 DMC network scenario 50
3.1.1 Main assumptions 51
3.1.2 Multiple transmitters 52
3.2 Networking challenges in DMC networks 53
3.2.1 Propagation delay 53
3.2.2 Channel attenuation 55
3.2.3 Channel distortion 55
3.2.4 Limited capabilities of nanosystems 56
3.2.5 Node mobility 57
3.2.6 High node density 58
3.3 Summary and concluding remarks 59

4 Analysis of graphene RF plasmonic antennas 60
4.1 Electrical conductivity of graphene 61
4.1.1 Numerical methods 63
4.2 Surface plasmon polaritons in graphennas 65
4.2.1 Properties of SPP waves in graphennas 67
4.3 Scattering properties of graphennas 69
4.4 Resonance tuning of graphennas 72
4.4.1 Dimensions of the graphene patch 72
4.4.2 Dielectric substrate 72
4.4.3 Graphene chemical potential 77

4.4.4 Temperature . . . 80
4.4.5 Relaxation time . . . 81
4.5 Comparison with metallic antennas . . . 83
4.5.1 Radiation diagram . . . 84
4.5.2 Resonant frequency . . . 84
4.6 Photoconductive graphennas in radiation . . . 88
4.6.1 Device description . . . 90
4.6.2 Photoconductor model . . . 91
4.6.3 Results . . . 92
4.7 Summary and concluding remarks . . . 98

5 The terahertz channel in graphene-enabled wireless communications 100
5.1 Effects of molecular absorption in short-range terahertz communications . . . 101
5.1.1 System model . . . 101
5.1.2 Results . . . 103
5.2 Scalability of the channel capacity in GWC to the nanoscale . . . 109
5.2.1 Graphene-enabled wireless communications . . . 109
5.2.2 Channel capacity at the nanoscale . . . 112
5.2.3 Limits of the channel capacity . . . 120
5.2.4 Scalability guidelines . . . 123
5.3 Summary and concluding remarks . . . 125

6 Conclusions and future work 127

Appendix A N3Sim, a simulation framework for diffusion-based molecular communication 132
A.1 Diffusion-based molecular communication . . . 133
A.2 Related work . . . 134
A.3 Simulator architecture . . . 136
A.3.1 Node models . . . 137
A.3.2 Particle model . . . 139
A.3.3 Simulation space . . . 140

A.4 Collision detection 142
A.4.1 State of the art 142
A.4.2 Algorithm implemented in N3Sim 143
A.4.3 Cost analysis 145
A.4.4 Cost evaluation 147
A.5 Simulation results 147
A.5.1 Normal and anomalous diffusion 148
A.5.2 Pulse shapes 149
A.5.3 Train of pulses 150
A.5.4 Molecular harvesting 152
A.6 Summary and concluding remarks 156

Appendix B Derived publications and theses **158**
B.1 Publications derived from this thesis 158
B.1.1 Journal publications 158
B.1.2 Conference publications 159
B.2 Co-supervised master theses 160

References **161**

List of Figures

1.1 Conceptual diagram of a nanonetwork using GWC and individual nanosystem. 4
1.2 Intrabody nanonetworks for healthcare applications and the interconnected office. 5
1.3 On-body nanonetworks envisaged by the Guardian Angels project. [23] 6
1.4 Schematic representation of a 16-core Graphene-enabled Wireless Network-on-Chip (GWNoC). [25] 7
1.5 Short-range molecular communication techniques: molecular signaling and molecular motors. 9
1.6 Medium-range molecular communication techniques: flagellated bacteria and catalytic nanomotors. 10
1.7 Long-range molecular communication techniques: axons and light transduction. 11
1.8 Schematic diagram of a DMC process. 12
1.9 Schematic diagram of a graphenna. 17
1.10 Total path loss in a standard medium with 10% of water vapor molecules. 20
1.11 Summary of the main results of this thesis. 23

2.1 Molecular concentration as a function of time measured by the receiver nanosystem. 29
2.2 Normalized channel impulse response. 30
2.3 Magnitude of the normalized channel transfer function in dB. . . 31
2.4 Channel group delay. 31

2.5 Magnitude of the normalized channel transfer function in dB as a function of the transmission distance. 32
2.6 Channel group delay as a function of the transmission distance. . 33
2.7 Pulse delay as a function of the transmission distance. 35
2.8 Pulse amplitude as a function of the transmission distance. 36
2.9 Pulse width as a function of the transmission distance. 37
2.10 Concentration measured by the receiver when a train of molecular pulses is transmitted. 39
2.11 Pulse energy as a function of the transmission distance. 40
2.12 Pulse duration as a function of the fraction of the pulse energy required to detect a pulse. 42
2.13 Required energy to detect a pulse, as a function of the fraction of the pulse energy required to detect a pulse. 43
2.14 Pulse duration as a function of the transmission distance. 44
2.15 Molecular concentration measured by receivers located at different distances from the transmitter. 47

3.1 Schematic diagram of a multipoint-to-multipoint DMC network. . 50
3.2 Concentration measured by a receiver nanosystem when two transmitters simultaneously emit a molecular pulse. 53

4.1 Sketch of the graphenna under consideration. 61
4.2 Total conductivity and intraband conductivity of graphene. 63
4.3 Extinction cross section per unit width of a graphenna, comparing the surface impedance model with the equivalent slab model. . . . 65
4.4 Dependence of the first resonance of an infinitely wide graphenna as a function of its length. 67
4.5 Plasmon compression factor in a graphenna as a function of the frequency and chemical potential. 68
4.6 Plasmon propagation length in a graphenna as a function of the frequency and chemical potential. 69
4.7 Scattering and absorption cross sections of a graphenna. 71
4.8 Dependence of the first resonant frequency of the graphenna on its length, for different widths. 73

4.9 Normalized extinction cross section of the graphenna placed on different substrates and for different substrate thicknesses. 74
4.10 Extinction cross section of a graphenna for different substrate sizes. 75
4.11 Different positions of the graphene patch with respect to the substrate. 76
4.12 Extinction cross section of a graphenna, for different positions of the graphene patch with respect to the substrate. 76
4.13 Graphene conductivity as a function of the frequency, for different values of the chemical potential. 78
4.14 Absorption cross section of a graphenna as a function of frequency, for different values of the chemical potential. 79
4.15 Dependence of the graphenna resonant frequency on the temperature. 81
4.16 Graphene conductivity as a function of the frequency, for different values of the relaxation time. 82
4.17 Absorption cross section of a graphenna for different values of the relaxation time. 83
4.18 Schematic diagram of the graphenna in transmission. 85
4.19 Radiation pattern of graphene and metallic antennas as a function of their width. 85
4.20 Scalability of the resonant frequency of graphene and metallic antennas as a function of their length. 87
4.21 Schematic representation of a graphenna fed with a photoconductive material. 90
4.22 Generated voltage by the photoconductive source, in the time and frequency domains. 92
4.23 Schematic model of the dipole graphenna considered. 94
4.24 Radiated power as a function of frequency for graphennas with different lengths, considering an electron mobility of 20000 cm^2/Vs. 95
4.25 Radiated power as a function of frequency for graphennas with different lengths, considering an electron mobility of 10000 cm^2/Vs. 96
4.26 Radiated power as a function of frequency for graphennas with different chemical potentials. 97

4.27 Maximum radiated power by the graphenna as a function of the average optical power in the photoconductive source. 97
4.28 Radiated power as a function of frequency for graphene bowtie antennas with different widths. 98

5.1 Molecular absorption as a function of frequency for different transmission distances. 103
5.2 Available bandwidth due to molecular absorption, as a function of the transmission distance. 104
5.3 Channel transfer function and impulse response of the molecular absorption for different transmission distances. 105
5.4 Width of the channel impulse response due to molecular absorption, as a function of the transmission distance. 106
5.5 Amplitude of the channel impulse response due to molecular absorption, as a function of the transmission distance. 107
5.6 Energy of the channel impulse response due to molecular absorption, as a function of the transmission distance. 108
5.7 Schematic diagram of a GWC network and a magnified individual nanosystem. 110
5.8 Quantitative values of the channel capacity as a function of the antenna length and the transmission distance, when a metallic antenna is considered. 119
5.9 Quantitative values of the channel capacity as a function of the antenna length and the transmission distance, when a graphenna is considered. 120
5.10 Feasible area of the channel capacity as a function of α and β. . . 122
5.11 Comparison of the scalability of the transmitted power by a metallic antenna and a graphenna, as a function of the antenna length. 124

A.1 Block diagram of the simulation framework *N3Sim*. 138
A.2 Schematic description of Baraff's algorithm for collision detection. 143
A.3 Schematic description of the algorithm used for collision detection in *N3Sim*. 144

A.4 Comparison of the computational cost of the collision detection algorithm used in *N3Sim* and a brute force approach. 148
A.5 Received signal when a molecular pulse is transmitted in a scenario of normal diffusion. 149
A.6 Received signal when a molecular pulse is transmitted in a scenario of anomalous diffusion. 150
A.7 Transmission of a Gaussian-shaped molecular pulse. 151
A.8 Transmission of a square-shaped molecular pulse. 151
A.9 Received signal when a train of molecular pulses is transmitted, in a scenario of normal diffusion. 152
A.10 Charge/drain operations of the reservoir of a harversting node. . . 153
A.11 Schematic diagram of a setup containing a transmitter, a receiver and a harvesting node. 153
A.12 Amplitude of the signal measured by the receiver, when a molecular pulse with different amplitudes is transmitted. 154
A.13 Amplitude of the signal measured by the receiver, as a function of the transmitted pulse amplitude, when using an unlimited harvesting node. 155
A.14 Maximum pulse frequency at the transmitter and achievable throughput at the receiver. 156

List of Tables

2.1 Communication metrics in DMC and traditional wireless communications. 47

3.1 Main guidelines for DMC networks. 59

4.1 Resonant frequency of a graphenna as a function of the chemical potential. 80
4.2 Main parameters of the photoconductive antenna. 93

5.1 Scalability of the performance metrics of molecular absorption in GWC. 108
5.2 Values chosen for the parameters in a typical scenario of GWC. . 119

6.1 Scalability of relevant performance metrics in DMC compared to traditional wireless communications, with respect to the transmission distance d. 128
6.2 Scalability of relevant performance metrics in GWC compared to traditional wireless communications, with respect to the antenna length L and the transmission distance d. 129

A.1 Main parameters of *N3Sim* 141

Nomenclature

Roman Symbols

A_{abs}	Molecular absorption
B	Bandwidth
c	Speed of light in vacuum
C	Channel capacity
$c_{\max}$	Pulse amplitude
D	Substrate thickness
d	Transmission distance
D_C	Medium diffusion coefficient
E	Electric field
e	Electron charge
E_p	Pulse energy
f	Frequency
f_R	Antenna resonant frequency
$h(t, d)$	Channel impulse response
$\hbar$	Reduced Planck's constant
h	Planck's constant
$H(f, d)$	Channel transfer function
i	Imaginary unit
K	Plasmon compression factor

k_0	Free-space wavenumber
k_B	Boltzmann constant
k_{SPP}	SPP wavenumber
L	Antenna length
L_{SPP}	Plasmon propagation length
P_{rad}	Power radiated by the antenna
P_T	Transmitted power
Q	Number of transmitted molecules
T	Temperature
t_D	Pulse duration
t_d	Pulse delay
t_w	Pulse width
V	Voltage at the antenna terminals
v_p	Wave propagation speed
W	Antenna width
Z_a	Antenna input impedance
Z_s	Surface impedance of graphene

Greek Symbols

α	Relative scaling trend between the transmission distance and the antenna length
β	Relative scaling trend between the transmitted power and the antenna length
Δ	Thickness of the equivalent slab model of graphene
δL	Penetration length of the electric field outside the antenna
ε	Relative permittivity (dielectric constant)
ε_0	Absolute permittivity

γ	Fraction of the pulse energy considered in the energy detection scheme
λ_{SPP}	SPP wavelength
λ_0	Free-space wavelength
μ_c	Chemical potential applied to graphene
μ_g	Electron mobility in graphene
ω	Angular frequency
σ	Electrical conductivity of graphene
σ_{abs}	Antenna absorption cross section
σ_{ext}	Antenna extinction cross section
σ_{sca}	Antenna scattering cross section
τ	Relaxation time of graphene
Θ	Asymptotical growth of a function

Acronyms

CMOS	Complementary Metal-Oxide-Semiconductor
DC	Direct Current
DMC	Diffusion-based Molecular Communication
EM	Electromagnetic
Graphenna	Graphene RF plasmonic antenna
GWC	Graphene-enabled Wireless Communications
GWNoC	Graphene-enabled Wireless Network-on-Chip
LT-GaAs	Low-Temperature-grown Gallium Arsenide
Nanonetwork	Nanoscale communication network
RF	Radio Frequency
SPP	Surface Plasmon Polariton
THz	Terahertz
WNSN	Wireless Nanosensor Network

Chapter 1

Introduction

This chapter begins with the introduction of the background of this thesis in Section 1.1. The rapid progress of nanotechnology has allowed the development of nanosystems with a microscopic size which may be interconnected by means of nanonetworks. Several potential applications of nanonetworks are outlined in Section 1.2. Section 1.3 describes the state of the art on the two main techniques that have been proposed to implement nanonetworks: diffusion-based molecular communication and graphene-enabled wireless communications. Finally, Section 1.4 expresses the motivation of this thesis and Section 1.5 describes its main contributions.

1.1 Background

1.1.1 Nanotechnology

Nanotechnology, first envisioned by the Nobel laureate physicist Richard Feynman in his famous speech entitled "There's plenty of room at the bottom" in 1959, is giving rise to devices and systems in a scale ranging from one to a few hundred nanometers. During the last few decades, emerging research areas such as nanoelectronics, nanomechanics and nanophotonics are allowing the development of novel nanomaterials, nanocrystals, nanotubes and nanosystems that promise to revolutionize many fields of science and engineering.

Molecular nanotechnology, popularized by Eric Drexler [1], is a particularly

advanced form of nanotechnology based on the ability to build molecular machines by means of mechanosynthesis. Since biology clearly demonstrates that molecular machines are possible (living cells themselves are an example), the manufacture of bio-inspired molecular machines using biomimetic techniques is envisaged in the near future.

Nanotechnology is a multidisciplinary field with almost uncountable potential applications. A few examples are presented next. First, in the biomedical domain, nanoparticles such as dendrimers, carbon fullerenes (buckyballs) and nanoshells are currently used to target specific tissues and organs [2]. Another area where nanotechnology plays an important role is environmental science, where molecular and genomic tools are used to uncover the complexity of the induced defense signaling networks of plants [3]. Finally, in the industrial field, molecular-scale filters and pores with well-defined sizes, shapes, and surface properties allow to engineer better functionality in molecular sieving [4].

The envisaged *nanosystems* are the most basic functional units able to perform very simple tasks at the nanoscale, including computing, data storage, sensing, actuation and communication. In the EM domain, the latest advances in nanotechnology have allowed the implementation of devices that perform some of these tasks, such as graphene nanosensors or lithium nanobatteries [5]. In the biological domain, cells are a clear example of living nanosystems. Therefore, even though a complete nanosystem has not been manufactured to date, simple artificial nanosystems are expected to become a reality in the near future.

1.1.2 Nanonetworks

Because of their tiny size, the operation range of nanosystems is limited to their close nano-environment. In consequence, a huge number of them will be required in order to perform meaningful tasks in a real scenario. These nanosystems will also need to control and coordinate their functions, leading to several research challenges in communication at the nanoscale.

Nanonetworks, the interconnection of nanosystems, provide means for cooperation and information sharing among them, allowing nanosystems to cover larger areas and fulfill more complex tasks [6, 7, 8]. The traditional mechanisms used in

traditional communication networks, such as mechanical, acoustic and EM communication, have been found inappropriate at the nanoscale, due to the difficulty of scaling down current transceivers and energy constraints [9]. A nanonetwork cannot thus be implemented by merely downscaling a conventional network; on the contrary, classical communication techniques need to undergo a profound revision before being applied to this new scenario. To date, several mechanisms have been proposed to interconnect nanosystems, leading to two novel network paradigms at the nanoscale: molecular communication [10, 11] and graphene-enabled wireless communications [5]. These two schemes are thoroughly reviewed in Section 1.3.

Nanonetworks have emerged as a novel research field which has attracted the interest of researchers from the domains of information and communication technology, nanotechnology and biology. A proof of the thriving research activity in this area is the appearance of dedicated journals [12] and the organization of specialized workshops and conferences [13].

1.2 Applications of nanonetworks

Nanonetworks will boost the range of applications of nanotechnology, bringing new opportunities in fields as diverse as Information and Communication Technology (ICT) (e.g., programable matter [14]), biomedical technology (e.g., cooperative drug delivery systems [2]) or environmental research (e.g., distributed air pollution control [4]).

1.2.1 Wireless Nanosensor Networks

One of the main application scenarios for nanonetworks which have been proposed to date is in the field of nanosensors [15, 16]. A nanosensor is a device that makes use of the unique properties of new nanomaterials to detect and measure events at the nanoscale. Since the detection range of nanosensors is limited to their close environment, communication among nanosensors will be needed to cover larger areas. Wireless Nanosensor Networks (WNSN), a particular case of nanonetworks but probably one of the most promising ones, implement this communication

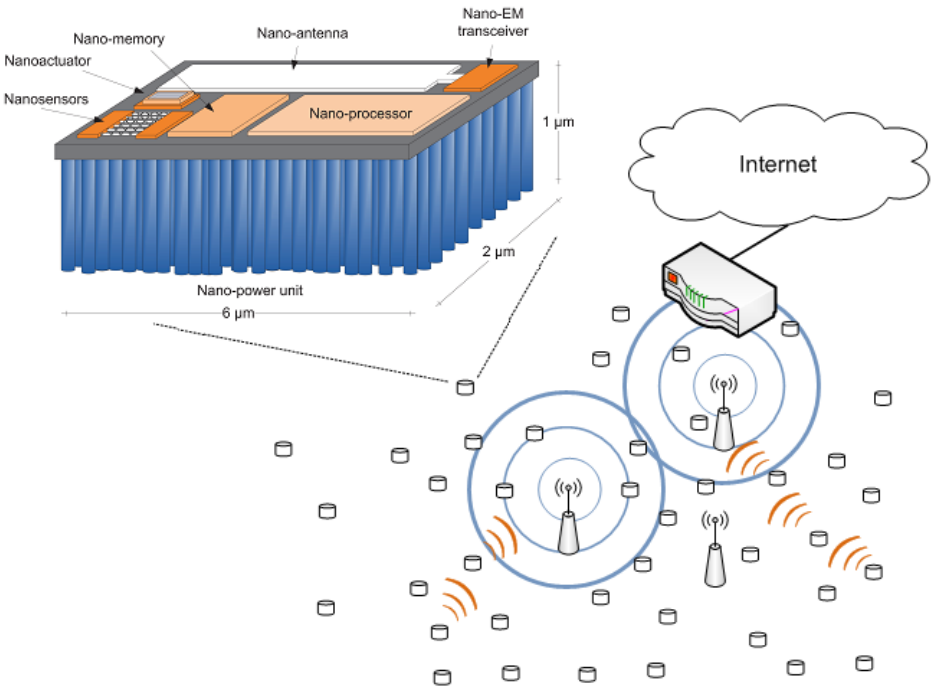

Figure 1.1: Conceptual diagram of a nanonetwork using graphene-enabled wireless communications. The upper left corner shows a magnified individual nanosystem. [5]

by encapsulating nanosensors into nanosystems, which communicate in order to cooperatively monitor physical or environmental conditions over a large field.

A sample conceptual diagram of a WNSN is depicted in Figure 1.1. The information is transmitted wirelessly among the nanosystem until reaching a central hub, which acts as an interface to the macro-scale world.

A biomedical scenario where WNSN could be applied is an intelligent disease detection and targeted drug delivery system (Figure 1.2, left), constituted by an intrabody distributed network of nanosensors and nanoactuators. Nanosensors that have already been successfully manufactured are able to detect lung cancer, asthma attacks, the influenza virus, or the parasite responsible for malaria [17, 18]. Several nanoactuators that have also been synthesized include nanoheaters based on magnetic nanoparticles able to kill cancer cells by heating them [19, 20], and magnetic nanoparticles and gold nanoshells which may be used as drug containers. The contained drugs are released through the application of local heat, which

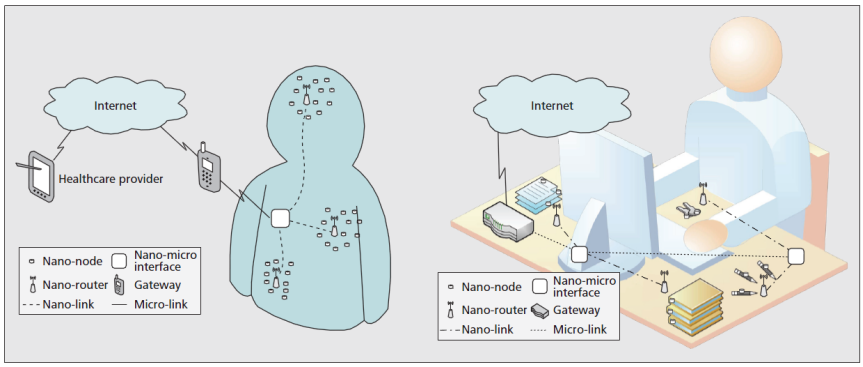

Figure 1.2: Intrabody nanonetworks for healthcare applications (left) and the interconnected office (right). [22]

melts the containers [21].

Another interesting application of WNSN is the interconnected office (Figure 1.2, right), where every single element normally found in an office is provided of a nanotransceiver which allows it to be permanently connected to the Internet, thereby allowing their remote tracking and control permanently. This application may lead to a new networking paradigm known as the "Internet of the nano-things" [22], defined by the interconnection of nanosystems with classical networks and ultimately the Internet.

A number of scenarios where WNSN could be useful are given by the research project "Guardian Angels for a smarter life" [23], aiming to develop ever more compact and streamlined technology that slips seamlessly into our daily lives. Nanosystems inserted into the fabric of clothing or in a simple bracelet, as shown in Figure 1.3, would enable the continuous monitoring of health conditions and the prevention of accidents. Other applications consider nanosensors which observe the ambient conditions for environmental threats, and devices which perceive the emotional or affective conditions of people.

1.2.2 Graphene-enabled Wireless Networks-on-Chip

The integration of wireless comunications in an on-chip scenario represents another promising application of nanonetworks. Indeed, nanonetworks implemented with the paradigm of graphene-enabled wireless communications can be effectively

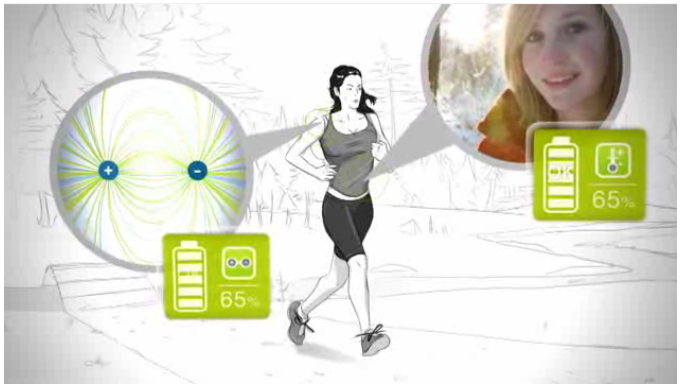

Figure 1.3: On-body nanonetworks envisaged by the Guardian Angels project. [23]

used as a way to communicate the different processors or cores of a chip multiprocessor. This new communication technique is known as Graphene-enabled Wireless Network-on-Chip (GWNoC, illustrated in Figure 1.4). Deployed over a state-of-the-art on-chip interconnection network [24], a GWNoC enables point-to-point, broadcast and multicast communications in the terahertz band, which potentially offers enough bandwidth in this data-intensive scenario. From the multicore architecture perspective, such feature creates a large range of possibilities with potential to cause a paradigm shift in how processors interact between them and with memory [25], for instance in terms of data/cache coherence, consistency or synchronization. Some of the main research challenges in this area include the development of new communication protocols suited to GWNoC, as well as novel scalable multicore architectures that minimize many of the issues present in multiprocessor environments.

GWNoC, where multi-core processors are equipped with antennas for communications, show potential to cause a paradigm shift in how processors interact between them and with memory, resulting into a radically new multicore architecture. Therefore, GWNoC represent an opportunity to revolutionize the area of interconnect technologies in multi-core processors.

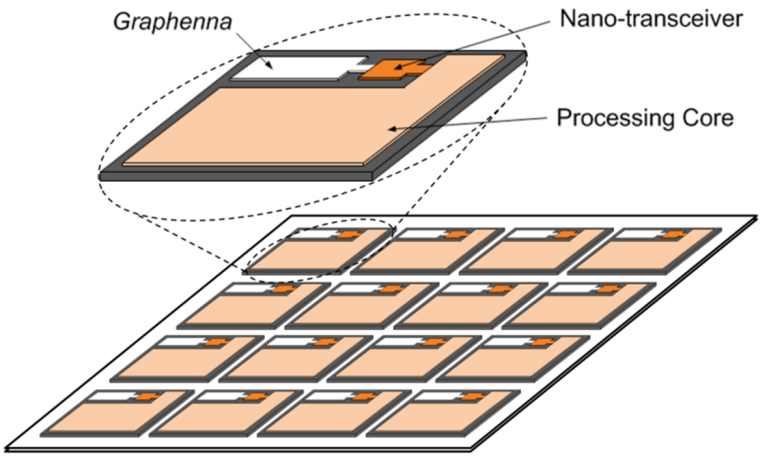

Figure 1.4: Schematic representation of a 16-core Graphene-enabled Wireless Network-on-Chip (GWNoC). [25]

1.3 State of the art

The main focus of this thesis is to study the scalability limits of communication networks to the nanoscale. With this purpose, the state of the art in the two paradigms that have been proposed to date to enable nanonetworks, namely, molecular communication [10, 11] and graphene-enabled wireless communications [5], is reviewed next.

1.3.1 Molecular communication

Molecular communication is inspired by communication among living cells [26]. A typical cell size is of 10 µm and a typical cell mass is 1 nanogram, in the same order of magnitude than the expected size of nanosystems. This fact has led researchers to study communication mechanisms among living cells with the objective of applying them to implement nanonetworks in biological scenarios.

The molecular communication techniques found in biology are very distance-dependent. In other words, different communication techniques must be used depending upon the distance between emitters and receivers. These techniques can be classified into three categories: short-range (nm to µm), medium-range (µm to mm) and long-range (mm to m) techniques:

- For the *short range*, two methods have been proposed [6]. The first one is molecular signaling, based on encoding the information in the emission of molecules which diffuse in the medium. The second technique is based on molecular motors, protein complexes that are able to transport molecules from transmitters to receivers through microtubules [27]. A schema of the communication process using short-range molecular communication techniques is depicted in Figure 1.5.

- Two mechanisms have also been proposed for *medium-range* molecular communication: flagellated bacteria [28, 29, 30] and catalytic nanomotors [31]. Both methods are based on encoding the information in DNA sequences (a DNA packet), which are carried from transmitter to receiver using bacteria or nanomotors, respectively. Figure 1.6 shows a diagram of these communication techniques.

- Finally, several techniques have been proposed for the *long range*, such as pheromones, pollen, spores and light transduction [32], which are used by many species to communicate. Examples include quorum sensing [33], a decision-making process used by bacteria to coordinate their behavior, and neuronal networks [34], where a group of neurons communicate by sending electrical and chemical signals through axons. Some of these methods are illustrated in Figure 1.7.

Diffusion-based molecular communication

Among the diverse techniques that have been proposed to implement molecular communication, Diffusion-based Molecular Communication (DMC) is the most relevant one. DMC is a widely studied molecular communication technique, since it allows modeling calcium signaling [26, 35, 36, 37], one of the most important communication mechanisms among living cells. Calcium signaling is based on the use of calcium ions (Ca^{2+}) to encode and transmit information. Moreover, DMC can also be used to model other types of molecular communication processes, such as quorum sensing or the propagation of pheromones, amongst others.

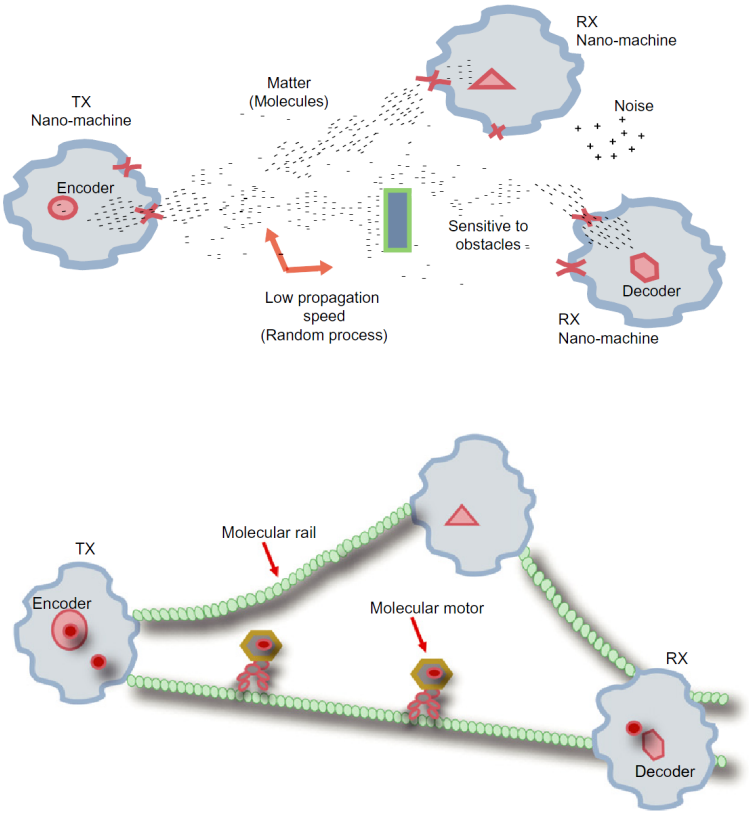

Figure 1.5: Short-range molecular communication techniques: molecular signaling (top) and molecular motors (bottom). [6]

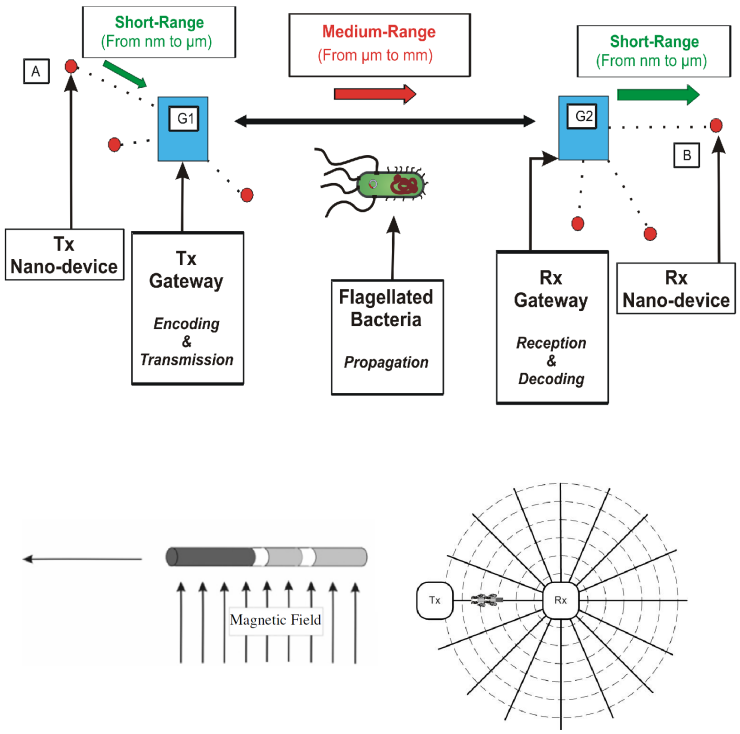

Figure 1.6: Medium-range molecular communication techniques: flagellated bacteria (top) and catalytic nanomotors (bottom). [28, 31]

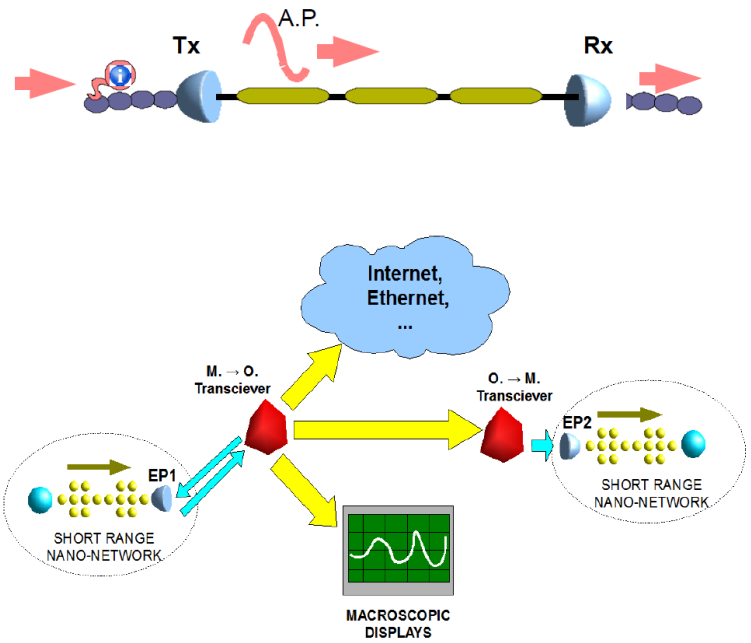

Figure 1.7: Long-range molecular communication techniques: neuronal networks (top) and light transduction (bottom). [32]

A DMC process can be described as a set of nanosystems which communicate by means of molecular diffusion in a fluid medium. As shown in Figure 1.8, a DMC process is composed of three main phases: emission, propagation and reception. First, transmitter nanosystems encode the information to be sent into the release pattern of molecules to the medium. The emitted molecules move following a random erratic trajectory, due to the collisions between them and the molecules of the fluid. As a consequence of this movement and of interactions among the emitted molecules (such as collisions and electrostatic forces), the emitted molecules diffuse throughout the medium. This diffusion causes the concentration of molecules to propagate and spread throughout the space. Finally, receivers are able to estimate the concentration of molecules in their neighborhood. This measurement activates specific signal transducing mechanisms which allow the receivers to decode the transmitted information.

In DMC, the evolution of the molecular concentration throughout space and time is modeled as a diffusion process. Depending on the scenario, different

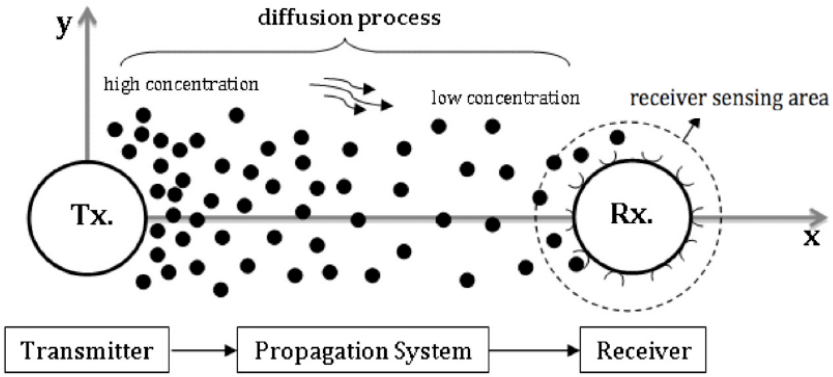

Figure 1.8: Schematic diagram of a DMC process. The transmitter nanosystem (left) emits molecules which propagate through molecular diffusion until they reach the receiver nanosystem (right). [38]

diffusion models may be used, which can be grouped into two categories: normal diffusion and anomalous diffusion [39].

On the one hand, *normal diffusion* refers to the case when the movement of the emitted molecules can be modeled by Brownian motion [40], which is valid when viscous forces dominate the motion of the emitted molecules and the interactions among them can be neglected. In this case, the movement of each of the molecules is uncorrelated and the diffusion process can therefore be macroscopically modeled with Fick's laws of diffusion [41].

On the other hand, *anomalous diffusion* appears when interactions among the emitted molecules affect their diffusion process. For instance, in a particular case of molecular signaling known as calcium signaling [36], based on the use of positive-charged calcium ions (Ca^{2+}), the electrostatic forces among these ions impact their diffusion process. Another example of anomalous diffusion includes the case in which the concentration of emitted particles is very high and the collisions among them affect their movement, a scenario known as *collective diffusion* [42]. In these cases, the diffusion process can no longer be modeled by Fick's laws of diffusion and it needs to be analyzed with other methods, such as correlated random walk [43].

The integration of the molecular transceivers needed for the emission and reception of information into nanosystems is inspired on the mechanisms developed

by nature for communication among living cells, such as the ligand-binding reception process [44]. Moreover, the use of chemically-driven transceivers ensures the bio-compatibility of the communication process, as well as an extremely high energy efficiency [45]. Bacteria populations have been proposed as transmitter and receiver nanosystems [46, 47, 48].

Several authors have provided analytical models for DMC, either focusing on the physical channel [49], or determining the channel capacity from an information-theoretical point of view [46, 50, 49, 51, 52, 53, 54]. Moreover, the definition of fundamental concepts such as noise [49, 44], caused by the randomness of the diffusion process, and interferences from multiple simultaneous transmissions [55, 56] in DMC has also been addressed.

Furthermore, an energy model is useful to determine the energy budget in DMC [57]; as opposed to the EM case, the energy is defined as the chemical energy (measured in ATP) required to produce the messenger molecules and release them to the environment. Several modulation techniques for DMC have also been proposed in the literature [58, 59].

A few works take a higher-level approach and consider the analysis of DMC networks. The definition of protocol primitives allows the design of novel protocols for DMC networks, such as the transmission of information by means of bacteria which follow specific attractants [10]. A unique feature of these networks is the node mobility, which is usually modeled as Brownian motion (analogously to the movement of molecules under normal diffusion) [60]. A promising research direction is the implementation of DMC networks inside the human body [61].

Some researchers consider particular application scenarios of DMC. For instance, extracellular communications in blood vessels can be modeled by a diffusion process together with a drag force, which corresponds to the flow of the blood stream [62]. Given the high concentration of calcium ions present in the extracellular environment, other carrier molecules such as cytokines are considered in this case [63].

A remaining challenge is the experimental validation of most of the existing models and protocols for DMC. By linking existing biological experiments in the fields of bacteria communication, membrane nanotubes and neuronal networks with the theoretical models of molecular communication, a fully opera-

tional molecular communication solution may be obtained in the future [64]. For example, preliminary experimental results obtained a microfluidic test-bed and a population of genetically engineered *Escherichia coli* bacteria have been reported [48]. In this work, a chemical stimulus of C6-HSL was delivered in one end of the flow channel for a pulse duration and the bacterial response was measured fluorescently at the other end. These results may allow the observation of the diffusion process in an in-vitro environment and the validation of analytical DMC models.

However, to the best of our knowledge, the existing literature does not capture all the particular characteristics of DMC networks. For instance, the expected simplicity of nanosystems will prevent the use of complex modulations or signal detection schemes, and the expectedly huge propagation delay will require rethinking the synchronization protocols of traditional wireless networks. Therefore, a framework that evaluates the performance of DMC networks while taking into account the uniqueness of their physical channel is needed to help designers of protocols and techniques for this networking model.

1.3.2 Graphene-enabled wireless communications

A different approach considers implementing wireless communications among nanosystems by means of EM waves [5, 22]. In this case, there are doubts about the feasibility of scaling current metallic antennas down to a few micrometers, mainly because of the low mobility of electrons in microscale metallic structures and especially because their resonant frequency would be extremely high [65]. The resonant frequency f of a free-standing metallic antenna can be obtained by solving the standard dispersion relation $c = \lambda f$, where c is the speed of light and λ is the wavelength. The first resonant frequency of this antenna corresponds to the case when the antenna length L is equal to half a wavelength, i.e., $L = \lambda/2$; then, it has the expression $f = c/2L$. In consequence, for the expected size of a nanosystem (a few µm) [5], the frequency radiated by a metallic antenna would be in the infrared and optical range (hundreds of terahertz). Such a high frequency would result in a very large bandwidth, but also in a huge channel attenuation which, given the expectedly very limited power of nanosystems, would

greatly reduce the transmission range of nanosystems. Moreover, it would be difficult to implement the transceivers able to operate at the optical frequencies required by such metallic antennas. These two reasons appear to render the practical implementation of wireless communications among nanosystems using metallic antennas unfeasible. In order to overcome these fundamental limitations, Graphene-enabled Wireless Communications (GWC) have been proposed to implement communication among nanosystems [66, 25]. An overview of graphene RF plasmonic antennas, which constitute the cornerstone of GWC, follows.

Graphennas: graphene RF plasmonic antennas

Graphene, a material consisting of a flat monoatomic layer of carbon atoms tightly packed in a two-dimensional honeycomb lattice, has attracted an intense attention of the research community due to its extraordinary mechanical, thermal, chemical, electronic and optical properties [67, 68, 69]. Due to its unique characteristics, graphene has given rise to a plethora of potential applications in diverse fields, ranging from electronics to chemistry.

In particular, the high electron mobility of graphene makes it an excellent candidate for ultra-high-frequency applications. For instance, prototypes of several graphene devices have been experimentally fabricated and measured in the last few years, such as graphene FET transistors working at frequencies of hundreds of gigahertz [70, 71, 72, 73, 74, 75, 76, 77], as well as graphene ambipolar devices for analogue and RF circuits [78, 79], such as LNAs [80], mixers [81] and frequency multipliers [82, 83]. Even complete graphene integrated circuits have been experimentally demonstrated [84] and have been the object of several patents [85, 86]. In consequence, graphene is considered to be among the main candidates to become the silicon of the 21^{st} century [87].

In the field of wireless communications, graphene has been proposed to implement miniaturized RF antennas [88]. In particular, graphene RF plasmonic antennas, or *graphennas*, with a size in the order of a few micrometers show plasmonic effects which allow them to radiate EM waves in the terahertz band (0.1-10 THz). This frequency band is up to two orders of magnitude below the optical frequencies at which metallic antennas of the same size resonate, thereby

enhancing the transmission range of graphennas and lowering the requirements on their future transceivers.

Preliminary studies on dipole antennas formed by carbon nanotubes found unique properties with respect to similar metallic antennas, due to the conductivity of carbon nanotubes and their plasmon effects [89, 90]. The main drawbacks of carbon nanotube antennas are their very low radiation efficiency and the difficulty of contacting them to feed an EM signal into the antenna.

Graphene patch antennas were analyzed for the first time by *Jornet et al.* by means of a tight-binding model of graphene [91]. Using a quantum mechanical framework, a patch antenna with dimensions of several hundred nanometers was found to resonate in the terahertz band, from 1 to 5 THz. Later, graphene nanoribbon antennas were analyzed based on the conductivity of graphene nanoribbons and the plasmonic properties of graphene [92]. The results showed again a resonant frequency in the terahertz band, at a much lower frequency than equivalent metallic antennas.

A radiation efficiency of up to 25% in a graphene patch antenna has been obtained by simulation, comparable to or better than metal implementations [93, 94]. At the same time, the antenna input impedance was found to be relatively high compared to metallic antennas, in the order of several hundred ohms; this aspect will reduce their impedance mismatch when graphennas are fed with photoconducting sources, which have a typical impedance of 10 kΩ [93, 94]. A comparison of the properties of graphennas at microwave and terahertz frequencies demonstrated that graphennas are able to operate in a wide frequency range [95].

Even though graphennas have only been analyzed to date from a theoretical perspective and by simulation, terahertz plasmonic resonances of graphene devices have been experimentally observed by several groups [96, 97, 98, 99]. Due to this fact, together with the plethora of experimental graphene devices previously mentioned, graphennas are expected to be successfully manufactured in the near future. Since graphennas are envisaged to provide wireless communication capabilities to future nanosystems, an analytical framework that provides guidelines and predicts the performance of GWC will prove useful for designers of graphennas, nanosystems and GWC networks.

In this thesis, a simple model for a graphenna is considered, composed of a

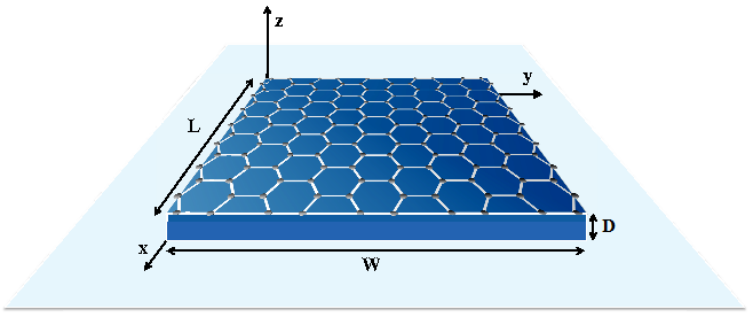

Figure 1.9: Schematic diagram of a graphene RF plasmonic antenna (graphenna).

finite-size graphene layer mounted over a metallic flat surface (the ground plane), with a dielectric material layer in between and an ohmic contact [91]. The conceptual design of the considered graphenna is shown in Figure 1.9, where L and W are the antenna length and width, respectively, and D is the thickness of the dielectric substrate.

The working principle of a graphenna in reception is as follows:

- When an EM wave irradiates the graphenna perpendicularly (wave propagation in the z-axis in Figure 1.9), it excites the free electrons on the graphene layer. The electronic response of the graphene layer to an EM field is therefore characterized by its conductivity. Because of the importance of the graphene conductivity in the performance of graphennas, the state of the art in graphene conductivity is reviewed in Section 4.1.

- At the interface between the graphene layer and the dielectric material, Surface Plasmon Polariton (SPP) waves are excited. SPP waves are confined EM waves that result from the coupling between surface electric charges at the interface between a metal and a dielectric, and an incident EM wave. Graphene plasmonics have been the focus of many theoretical and experimental works [100, 101, 96, 102, 103, 104, 105, 106, 107, 108, 109, 105].

- By exploiting the propagation of SPP waves in graphene, graphene plasmonic antennas can be developed. The main difference between a metallic antenna and a plasmonic antenna is that the electrical length of the plasmonic antenna is much smaller than that of a metallic antenna, due to the

much lower wavelength of SPP waves in the plasmonic antenna compared to free-space EM waves [110]. This results in far more compact plasmonic antennas which can be integrated into nanosystems. Plasmonic antennas are not a new concept, but have been investigated before [111, 112, 113, 114]. The novelty of graphennas is that they propagate SPP waves at frequencies in the terahertz band (0.1-10 THz), up to two orders of magnitude below the optical frequencies of SPP waves observed in classical plasmonic antennas, made of gold and other noble materials [115]. In addition, the properties of SPP waves in graphene can be tuned by material doping, which opens the door to tunable graphennas [116, 65, 92, 117, 118].

According to the antenna reciprocity theorem, the behavior of the graphenna in transmission can similarly be explained as follows. When a time-varying electric current excites the graphene layer, an SPP wave is generated at the interface with the dielectric material layer. If the length of the graphene patch corresponds to integer number of half plasmon wavelengths of the SPP wave, the plasmonic antenna resonates and the radiated EM field from the antenna is maximized. Ultimately, the radiation properties of graphennas, such as their radiation efficiency and their radiated power, depend on the properties of the SPP waves, which in turn depend on the material conductivity and need to be solved by means of multi-physics simulation.

Channel models for wireless communications in the terahertz band

Graphennas radiate EM waves with a frequency lying in the terahertz band. Therefore, the evaluation of the performance limits of GWC requires an analysis of the wireless terahertz channel at very short transmission ranges (below 1 meter), which is the expected operation range of graphennas.

Short-range high-bandwidth terahertz wireless communications have been proposed for indoor scenarios with the objective of their standardization within the IEEE 802.15 Terahertz Interest Group, but they are aimed for transmission distances of several meters. In those cases, the propagation of terahertz waves is usually modeled by means of ray tracing [119] and the atmospheric attenuation shows several peaks in the terahertz band [120].

However, these models are not directly applicable to a scenario of GWC, which usually comprise communication distances of less than 1 meter. At this short range, the phenomenon of molecular absorption will influence the propagation of the terahertz signals in the atmosphere [121].

Molecular absorption is the process by which part of the wave energy is converted into internal kinetic energy of the excited molecules in the medium. Indeed, since several molecules present in the standard atmosphere (such as water vapor molecules) have thousands of resonances in the terahertz band, they are excited by the terahertz EM waves radiated by graphennas, converting part of the radiation into internal vibrations [120]. Molecular absorption acts as an additional factor of attenuation to the propagated signal in wireless communications in the terahertz band. It can be modeled by the following analytical expression [121]:

$$\alpha(f, d) = \frac{1}{\tau_m} = e^{k(f)d} \tag{1.1}$$

where f is frequency, d is distance, τ_m is defined as the transmittance of the medium and k is the medium absorption coefficient. This last parameter depends on the medium composition, i.e., the particular mixture of molecules that the propagating wave finds along the channel. Figure 1.10 shows the total path loss in the terahertz channel, comprising both the free-space path loss and molecular absorption, as a function of frequency and distance.

In addition, the absorption from molecules present in the medium not only attenuates the transmitted signal, but it also introduces noise. Indeed, when a terahertz wave is propagating through the atmosphere, the internal vibration of the molecules in the medium turns into the emission of EM radiation of the same frequency that the incident waves that provoked this motion. Thus, molecular noise needs to be taken into account as a new source of noise in a scenario of GWC.

The highly frequency-dependent molecular absorption has a key impact on the communication performance of GWC. Moreover, its influence is highly dependent on the transmission distance, which determines the number of molecules that the radiated terahertz waves will find along their path.

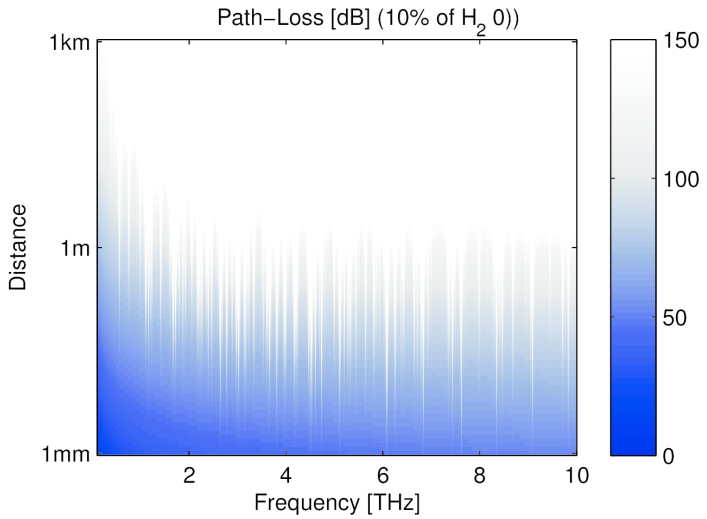

Figure 1.10: Total path loss in dB as a function of frequency and distance in a standard medium with 10% of water vapor molecules. [121]

1.4 Motivation

As described in the previous section, even though several analytical models of nanonetworks based on both DMC and GWC can be found in the literature, very few experimental results of communication among nanosystems have been reported to date. On the one hand, despite the latest advances in synthetic biology, an experimental setup of DMC among engineered nanosystems is still very challenging to build. In consequence, most of the existing literature in this area is focused in the proposal of communication protocols specially suited for DMC, information-theoretical studies of the performance of a DMC system, analytical channel models and simulation-based characterizations. On the other hand, even though a wide range of high-frequency graphene devices have been experimentally demonstrated, a complete GWC system has not been manufactured yet. The research in GWC networks is therefore also mostly based on analytical and simulation-based studies.

Given the theoretical nature of most literature in the field of nanonetworks, a key question naturally arises: what will be the performance of nanonetworks, particularly when compared to traditional wireless networks? The purpose of this thesis is to answer this question by means of a fundamental scalability study of

the performance metrics in a communication network to the nanoscale.

Scalability theories have hitherto set a framework for the development of circuits based on CMOS technology and derived a roadmap driving device designers to make circuits smaller such that the desired performance metrics can be optimized [122, 123, 124]. Essentially, the main parameters in a CMOS circuit, such as the minimum channel length, the substrate doping and the power supply voltage, were all scaled in each new CMOS technology generation by a scaling factor λ [124]. During the 1980s, CMOS circuits followed a scaling theory known as *constant voltage scaling* which maintained the power supply voltage accross generations. As consequence of the constant voltage scaling, the electrical field inside the transistors kept increasing as their dimensions were reduced. By the early 1990s, serious problems with excessive power dissipation and heating made more and more difficult to further scale down the dimensions of CMOS circuits. Fortunately, a scaling theory known as *constant field scaling* allowed overcoming these issues by reducing the power supply voltage by the same factor λ as the dimensions in each CMOS generation. This scaling law kept the electric field inside the transistors constant across generations and allowed a rapid improvement in the performance of microprocessors during that decade. In summary, these scaling theories for the downscaling of CMOS circuits made the well-known "Moore's law" possible.

The field of communications networks has also taken advantage of scalability theories to study their performance and design new protocols. As opposed to the case of electronic circuits, most existing solutions on network scalability in the literature consider scenarios in which the number of nodes in the network tends to infinity [125, 126, 127, 128, 129]. For instance, *Gupta and Kumar* [125] found that the throughput per source-destination pair of a wireless network with n randomly located nodes scales as $\Theta\left(1/\sqrt{n \log n}\right)$ as the number of nodes increases.

Inspired by these scalability theories, the scalability of the main performance metrics in a network of nanosystems is analyzed. In this thesis, however, as opposed to the case of most of the existing literature in network scalability, which considers the case when the network grows, the focus is placed on a scenario where the network size shrinks to the nanoscale. For both cases of DMC networks and GWC networks, the most relevant performance metrics are identified and their

depencence with the network dimensions are found.

As previously explained in Section 1.1.2, nanonetworks cannot be realized by simply reducing the size of traditional wireless networks. On the contrary, the physical channel of both DMC and GWC presents several fundamental differences with respect to traditional wireless communications. On the one hand, in a DMC scenario, information is encoded in molecules or DNA strings which are physically transported from the transmitter to the receiver by different mechanisms. On the other hand, in GWC, plasmonic effects appearing in graphene alter the radiation properties of graphennas. In consequence, graphennas are able to radiate EM waves in the terahertz band, a much lower frequency than what would be obtained if current metallic antennas were shrunk to the nanoscale. As a consequence of these singularities, the communication metrics of communication networks at the nanoscale will not necessarily be the same than their equivalent in traditional wireless and optical networks.

The scalability of these network performance metrics will determine whether the actual implementation of nanonetworks is *feasible*, thereby answering our initial question. Therefore, this thesis analyzes how the performance metrics of communication networks scale as their dimensions shrink, thereby exploring the scalability limits of communication networks to the nanoscale. The final objective is to derive guidelines that will help researchers to design future communication-enabled nanosystems and nanonetworks.

1.5 Main contributions

Several tasks are needed in order to find the scalability limits of communication networks to the nanoscale, which represents the main goal of the thesis. The main results of this thesis are depicted in Figure 1.11, where the vertical axis corresponds to the two communication paradigms that have been considered and the horizontal axis corresponds to the scale parameters considered, namely, the antenna length L and the transmission distance d. In DMC, the main result concerns the derivation of the analytical expressions of several communication metrics of DMC as a function of the transmission distance, assuming a modulation based on the emission of molecular pulses. In GWC, the resonant frequency

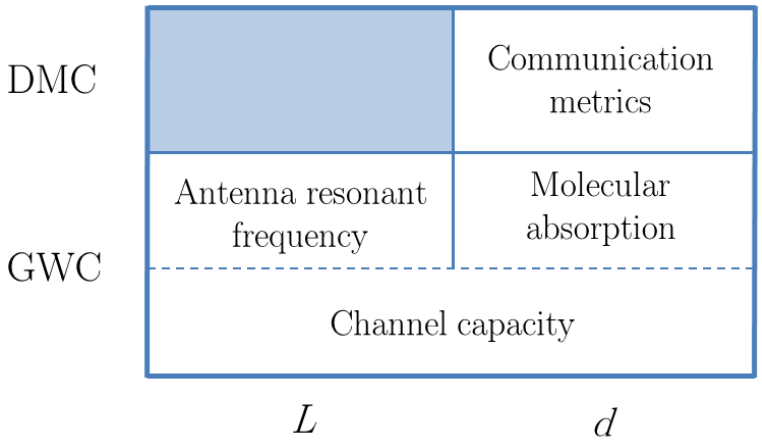

Figure 1.11: Summary of the main results of this thesis. The vertical axis corresponds to the paradigms of Diffusion-based Molecular Communication (DMC) and Graphene-enabled Wireless Communications (GWC), and the horizontal axis corresponds to the scale parameters considered: the antenna length L and the transmission distance d.

of graphennas is found to show novel scaling trends as a function of the antenna length, and molecular absorption introduces impairments which are largely dependent on the transmission distance. Finally, the channel capacity of GWC is found to scale both as a function of the antenna length and the transmission distance.

The contributions of this thesis are described in more detail as follows:

Physical channel model for DMC

Because of the fundamental differences between the physical channel of DMC with respect to that of EM communications, its characterization is first needed in order to address the scalability of DMC networks. With this purpose, a system of a point-to-point communication by means of DMC is considered. A simple modulation based on the transmission of short pulses which diffuse throughout the environment is proposed, as well as two pulse detection techniques, namely, amplitude detection and energy detection. These schemes are inspired in similar techniques in current impulse radio communications, but their definition is adapted to the new scenario of DMC.

Next, several important **communication metrics** in DMC, such as the pulse delay, the pulse amplitude and the pulse energy, are defined. Analytical expressions of these metrics are calculated and validated by simulation. Finally, the scalability of these metrics as a function of the transmission distance is obtained and compared to the case of traditional wireless communications. This contribution is detailed in Chapter 2.

Challenges and principles in DMC networks

Chapter 3 analyzes the implications of the unique properties of the DMC channel in the performance of DMC networks. The diffusion-based propagation of signals will create novel challenges in the design of DMC networks, such as the very high propagation delay or the random mobility pattern of nodes in these networks. At the same time, the unique characteristics of DMC also allow for the design of novel algorithms and schemes that take advantage of them, such as modulations, coding schemes and MAC protocols specifically conceived to optimize the performance of DMC networks.

Radiation properties of graphennas

Graphennas support the propagation of SPP waves, which show a significantly different behavior with respect to the propagation of EM waves in metallic antennas. In Chapter 4, a study of the plasmonic properties of graphennas is presented, by means of analytical models of the graphene conductivity and the dispersion relation of SPP waves in graphennas. The scattering and absorption cross sections of graphennas is also obtained analytically and by simulation.

Next, the implications of the plasmonic properties of graphennas in the scalability of GWC are considered. In particular, the scalability of the **resonance frequency of graphennas** with respect to several paramenters, such as the antenna dimensions, the quality of the graphene sample and the applied chemical potential is considered. A comparison of the scaling properties of graphennas with respect to metallic antennas as their size is reduced shows interesting insights. Indeed, the scaling trend of the resonant frequency in graphennas shows a significant improvement over the case of metallic antennas.

Furthermore, a realistic technique to feed a pulsed EM wave into a graphenna is proposed. A graphenna fed with a photoconductive source is designed and its radiated terahertz power is estimated by means of full-wave EM simulations.

The terahertz channel in GWC

Finally, Chapter 5 studies the terahertz channel at the very short range (from a few millimeters to a few meters), which corresponds to the expected operating scenario of graphennas. Two main aspects of the terahertz channel are considered. First, the effect of **molecular absorption**, a process by which part of the energy of terahertz waves is absorbed by molecules present in the atmosphere, in this scenario is evaluated. The scalability of molecular absorption in the channel bandwidth (in the frequency domain) and the channel impulse response (in the time domain) as a function of the transmission distance is found. Second, the scalability of the **channel capacity** in GWC is derived when the dimensions shrink to the nanoscale. The unique scaling properties of the resonant frequency of graphennas as their size is reduced are found to give GWC a scalability advantage, in terms of channel capacity, with respect to the case when metallic antennas are used.

Chapter 2

Characterization of the physical channel in diffusion-based molecular communication

This chapter focuses on a DMC scenario whose physical channel is governed by Fick's laws of diffusion. The impulse response, the transfer function and the group delay of this communication channel are derived. A pulse-based modulation scheme is then proposed and used to obtain analytical expressions of relevant communication metrics. Two schemes for the detection of the transmitted molecular pulses are proposed, namely, *amplitude detection* [130] and *energy detection* [131]. The analyzed communication metrics are the pulse delay, the pulse amplitude and the pulse width in the amplitude detection scenario, and the pulse delay, the pulse energy and the pulse duration, in the energy detection scheme. In both cases, quantitative expressions for the relevant communication metrics are analytically derived, validated by simulation and compared to their equivalent in traditional wireless communications. Finally, the scalability of the performance metrics corresponding to both signal detection mechanisms for DMC are compared to their equivalent in traditional wireless communications.

This chapter is organized as follows. Section 2.1 describes the considered DMC scenario and the proposed pulse-based modulation scheme. Section 2.2 represents the impulse response, the channel transfer function and the group delay of the

DMC channel. In Section 2.3, the amplitude detection and energy detection methods are introduced. Then, in Sections 2.4 and 2.5, analytical expressions of the relevant communication metrics are obtained in the amplitude detection and energy detection scenarios, respectively. Section 2.6 compares the scalability of these metrics in both scenarios with their equivalent in traditional wireless communications. Finally, Section 2.7 summarizes this chapter.

2.1 Modulation scheme for DMC

The DMC channel that will be characterized can be described as a couple of nanosystems which communicate through molecular diffusion in a fluid medium, as shown in Figure 1.8. A transmitter nanosystem encodes the information to be sent into a molecular release pattern. The emitted molecules cause a variation in their local concentration, which propagates throughout the medium. A receiver nanosystem is able to estimate the concentration of molecules in its neighborhood and, from this measurement, recover the release pattern and decode the sent information.

In the envisaged scenario, the concentration of emitted molecules is much lower than the concentration of the fluid molecules. Under these conditions, the interaction among the emitted molecules (e.g., collisions and electrostatic forces) can be neglected. An example of this kind of scenario is calcium signaling among cells, where extracellular concentration of calcium ions is in the millimolar range [36], while the concentration of water (the main component of extracellular fluid) is of 55.5 molar, more than 4 orders of magnitude higher.

In this case, which corresponds to the scenario of normal diffusion described in Section 1.3.1, each of the molecules released by a transmitter moves according to Brownian motion. Since the movement of each molecule is independent, molecular diffusion can be modeled by Fick's laws of diffusion [41] with a homogeneous diffusion coefficient both in space and time. In this case, the diffusion equations are linear [132].

Furthermore, the expected simplicity of nanosystems will prevent the use of complex modulation schemes in DMC, such as OFDM and spread-spectrum techniques. For this reason, a pulse-based modulation scheme for DMC is pro-

posed [130]. According to this scheme, whenever a transmitter nanosystem wants to communicate some information to its neighbors (e.g., after it detects an infectious virus [18]), it instantaneously releases a pulse of molecules. This creates a spike in the molecular concentration at the transmitter location, which then propagates through space and time. The propagation of this pulse can be analytically modeled by solving Fick's laws of diffusion. If the transmitter releases Q molecules at the instant $t = 0$, the molecular concentration at any point in space is given by [133]:

$$c(d,t) = \frac{Q}{(4\pi Dt)^{3/2}} e^{-d^2/4Dt} \tag{2.1}$$

where D_C is the diffusion coefficient of the medium, t is time and d is the distance from the transmitter location.

This expression is denoted as the *pulse equation*. Figure 2.1 shows a graphical representation of the molecular concentration measured by a receiver as a function of time, where the dashed blue line corresponds to the analytical result given by (2.1) and the red dots are simulation results, obtained using the simulation framework *N3Sim* (described in Appendix A). In this example, the diffusion coefficient is set to $D_C = 1\ \text{nm}^2/\text{ns}$, similar to that of ionic calcium in cytoplasm [134]. The transmitter is modeled as a point-wise source, whereas the receiver is represented by a sphere with a radius of 0.4 µm which is able to measure the average molecular concentration in its interior. The number of transmitted molecules is set to $Q = 5 \cdot 10^5$ and the transmission distance is $d = 3$ µm.

It can be observed that the concentration measured by the receiver is initially zero, but it quickly increases until reaching its maximum. The time instant at which this maximum occurs can be interpreted as the pulse delay. After the concentration peak is reached, the impulse response slowly decreases, forming a long tail due to the effect of diffusion. The difference between the expression of the pulse equation and the simulation results shows the presence of diffusion noise, which appears as a result of the stochastic nature of Brownian motion [135]. The diffusion noise represents the main limitation in the minimum molecular concentration that can be detected by a receiver, i.e., the receiver sensitivity. The expression of the diffusion noise $n(d,t)$ has zero mean and its standard deviation

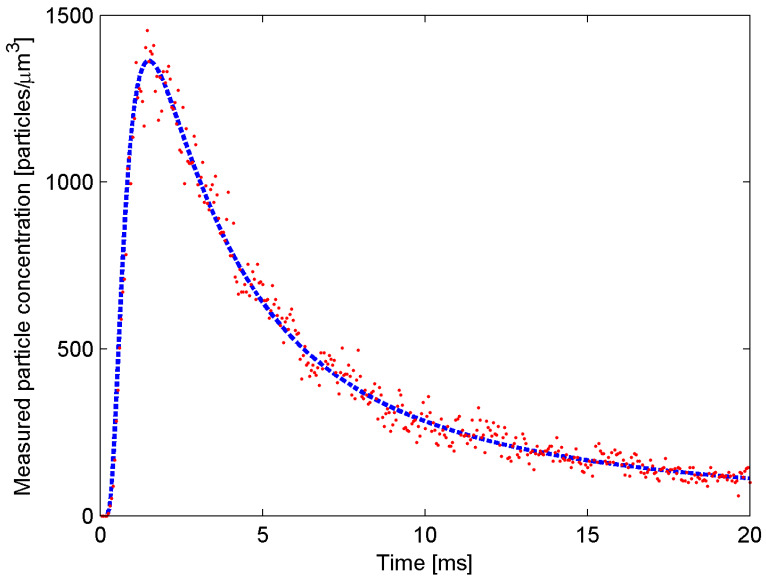

Figure 2.1: Molecular concentration as a function of time measured by the receiver nanosystem. The dashed blue line shows the analytical expression and the red dots correspond to simulation results.

is given by [135]:

$$\sigma\left[n(d,t)\right] = \sqrt{\frac{c(d,t)}{(4/3)\pi\rho^3}} \tag{2.2}$$

where ρ is the radius of the spherical receiver. Clearly, the diffusion noise has an inverse dependence on the receiver size: the larger the receiver is, the lower the diffusion noise will be.

As shown next, the pulse equation allows modeling important communication metrics in a DMC environment, which present fundamental differences with respect to traditional wireless communications and prove the uniqueness of the physical channel in DMC. Since the pulse equation considers the average value of the molecular concentration, this analysis will not be affected by the zero-mean diffusion noise.

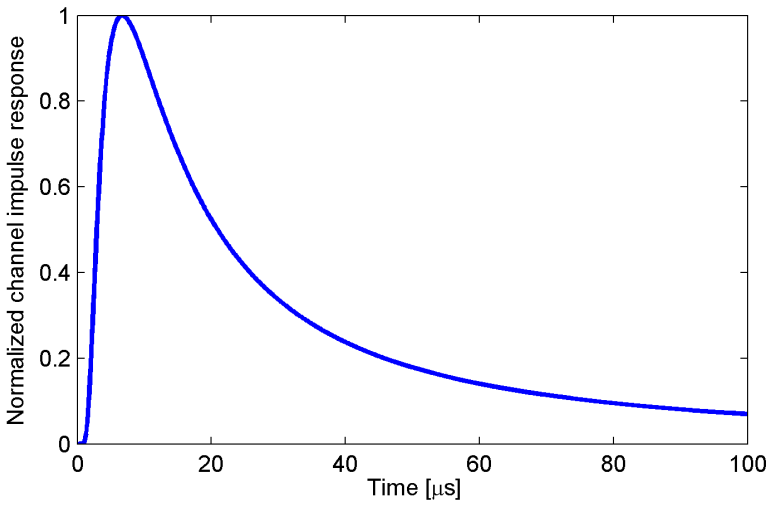

Figure 2.2: Normalized channel impulse response.

2.2 Physical channel analysis

The pulse equation (2.1) describes the concentration measured by a receiver located at a distance d from the transmitter as a function of time. Since the previously described DMC channel is linear and time-invariant [136], this measure can be interpreted as the channel response to an impulse of molecules, i.e., the channel impulse response $h(t, d)$. Figure 2.2 shows the impulse response of the DMC channel, normalized to values between 0 and 1. The transmission distance is set to $d = 200$ nm and the diffusion coefficient to $D_C = 1$ nm^2/ns.

The channel transfer function is then obtained by computing the Fourier transform of the impulse response. The magnitude of the channel transfer function $H(f, d)$, shown in Figure 2.3 in dB, can be interpreted as the channel attenuation. The results indicate that only low-frequency signals can be reliably transmitted through the channel. A notch at $f = 500$ kHz is observed, related to the delay caused by the diffusion process.

Figure 2.4 shows the group delay of the DMC channel. At low frequencies, two peaks appear: a positive peak at $f = 0$ Hz and a negative one at $f = 500$ kHz. The latter one is due to the delay that causes the notch in the channel transfer function at the same frequency. At higher frequencies, the channel group delay is approximately zero.

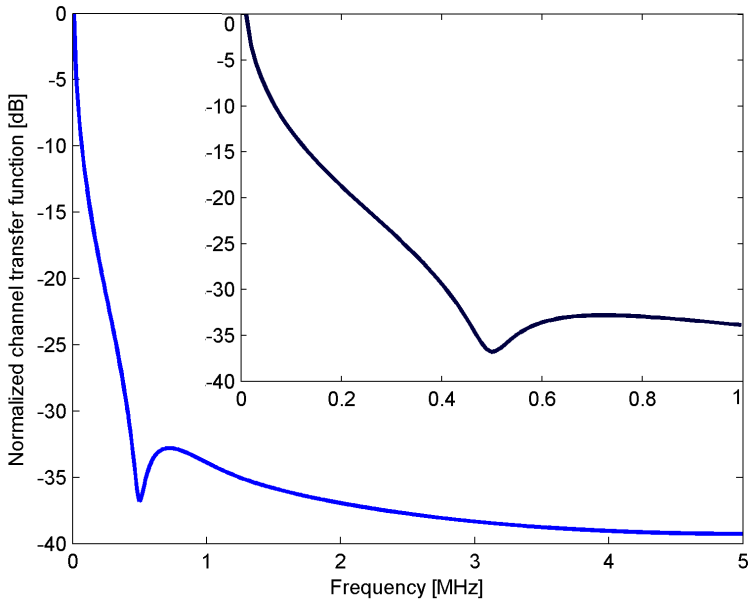

Figure 2.3: Magnitude of the normalized channel transfer function in dB. Inline: Magnified channel transfer function from 0 to 1 MHz.

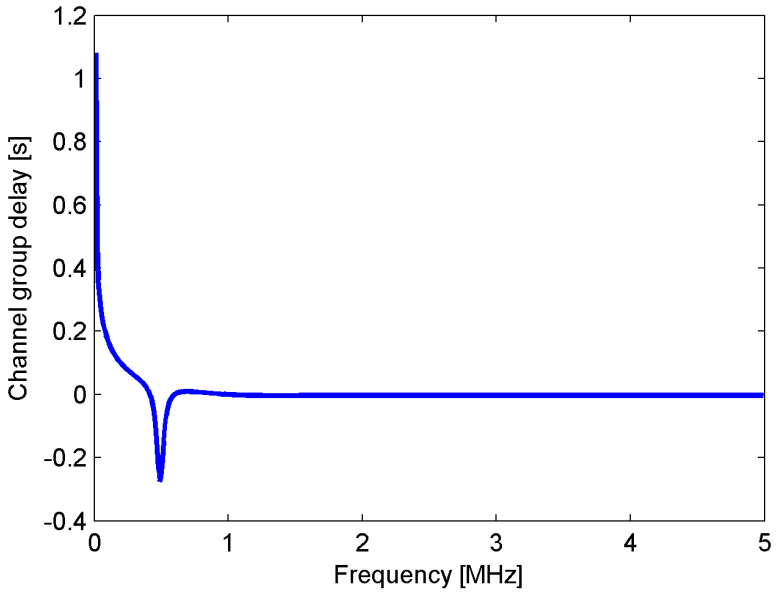

Figure 2.4: Channel group delay.

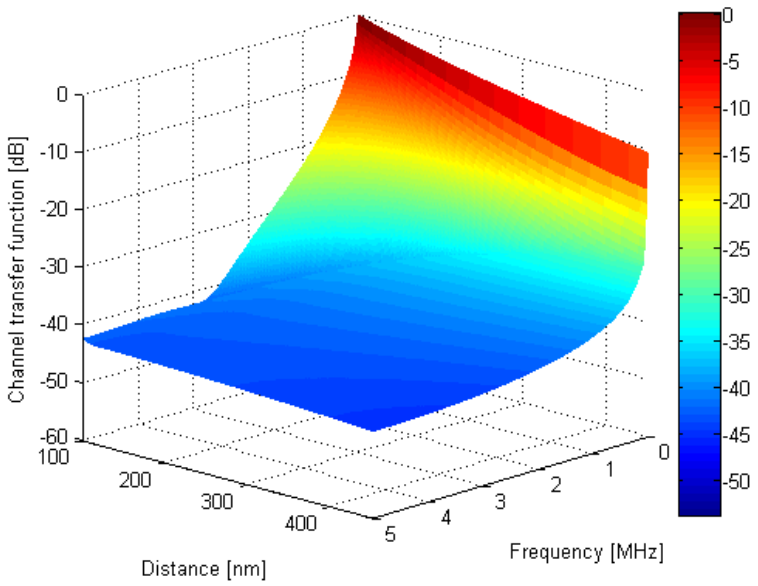

Figure 2.5: Magnitude of the normalized channel transfer function in dB as a function of the transmission distance.

Figures 2.5 and 2.6 plot the magnitude of the normalized channel transfer function and the group delay, respectively, as a function of both the frequency and the transmission distance. The transmission distance ranges from 100 to 450 nm. As expected, the channel attenuation increases both with the increase in frequency and in transmission distance. The channel group delay also increases with the the distance from the transmitter, and is nearly zero for frequencies higher than a few hundreds of kHz.

2.3 Detection methods for DMC with a pulse-based modulation

In this section, two methods are proposed for receivers to detect the transmitted pulses in a DMC network. First, using *amplitude detection* [130], receivers measure the variation of the local concentration of molecules over time. Then, the measured signal is interpreted as a bit "1" if its maximum concentration is over a given threshold, and as a bit "0" otherwise. The value of this threshold should

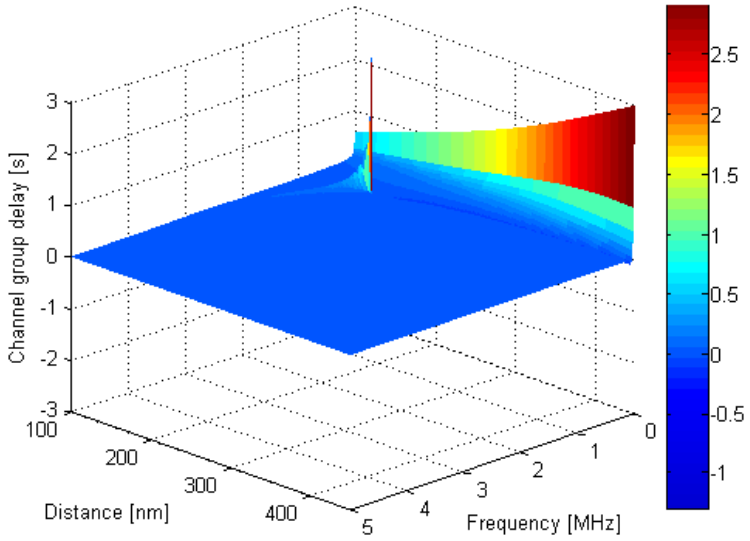

Figure 2.6: Channel group delay as a function of the transmission distance.

be selected as a function of the expected amplitude of the received signal.

An alternative technique for pulse detection in DMC is *energy detection* [131]. Making an analogy to EM communications, where the pulse energy is calculated as the integral of its power over time, the pulse energy in DMC is defined as the integral of the molecular concentration over time. Using this method, a receiver measures the energy of the molecular signal. The received signal is then interpreted as a bit "1" if its energy is over a given threshold, and as a bit "0" otherwise. A simple way for receivers to measure the pulse energy would be by accumulating the number of molecules received during the pulse duration.

Considering the pulse-based modulation scheme introduced in Section 2.1, the characteristics of the physical channel of DMC using both detection methods are explored next by analyzing the pulse equation (2.1). With this purpose, several metrics that will allow the assessment of the communication performance of DMC in different scenarios are identified. Analytical expressions for these metrics are obtained and validated by simulation with *N3Sim*. In order to make this analysis as general-purpose and technology-agnostic as possible, no constraints are set on the actual physical implementation of transmitters and receivers, nor on the size

and type of the emitted molecules.

2.4 Amplitude detection

Three relevant communication metrics in a DMC scenario using amplitude detection are analyzed next: 1) the pulse delay, which will determine the communication delay between the transmission and reception of molecular signals, 2) the pulse amplitude, which, as previously mentioned, will have a key impact on the detection of molecular signals, and 3) the pulse width, which will represent the main constraint for the achievable throughput using this technique.

2.4.1 Pulse delay

In order to find an expression for the pulse delay, the time instant for which the pulse equation (2.1) reaches its global maximum is computed. As observed in Figure 2.1, this function has only one local maximum, which is also its global maximum. The position of this maximum can therefore be computed by taking the time derivative of the pulse equation and finding the time instant at which it is equal to zero:

$$\frac{dc(d,t)}{dt} = \frac{d}{dt}\frac{Qe^{-d^2/4Dt}}{(4\pi Dt)^{3/2}} = 0. \tag{2.3}$$

From this equation, the time at which the pulse has its maximum is obtained by isolating the variable t. This time can be interpreted as the pulse delay t_d:

$$t_d = \frac{d^2}{6D_C}. \tag{2.4}$$

Note that the pulse delay is inversely proportional to the diffusion coefficient D_C. Hence, the higher the diffusion coefficient, the faster the molecular pulses will propagate.

In order to validate this result, the transmission of a pulse of $5 \cdot 10^5$ molecules is simulated using *N3Sim*. The diffusion coefficient is set to $D_C = 1$ nm^2/ns and the local molecular concentration is measured at distances from 1 to 4.5 µm, at intervals of 0.5 µm. Figure 2.7 shows a comparison between the analytical

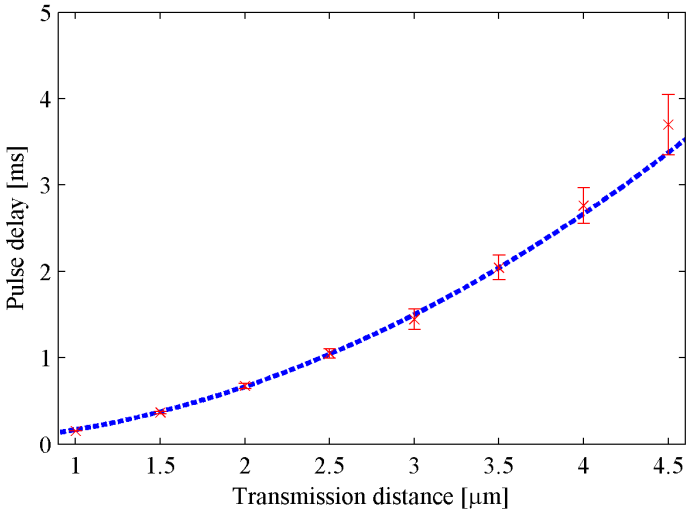

Figure 2.7: Pulse delay as a function of the transmission distance. The dashed blue line corresponds to the analytical expression and the red crosses show the simulation results with 99% confidence intervals.

expression of the pulse delay (dashed blue line) and the averaged results obtained with *N3Sim* after 30 simulation runs with 99% confidence intervals. These same simulation conditions will be used throughout this study, unless otherwise stated.

2.4.2 Pulse amplitude

It is also worth investigating the variation of the pulse amplitude over space, which may be interpreted as the channel attenuation. This amplitude is obtained by evaluating the pulse equation (2.1) at the time instant at which the pulse reaches its maximum value, which has been previously found in (2.4):

$$c_{\max} = c(d,t)|_{t=t_d} = \left(\frac{3}{2\pi e}\right)^{3/2} \frac{Q}{d^3}. \tag{2.5}$$

It is interesting to note that, as opposed to the pulse delay, the pulse amplitude is independent from the diffusion coefficient. In consequence, the diffusion coefficient of the medium will have no effect on the attenuation of the molecular pulses throughout space.

As previously, this result is validated by means of simulation. Considering

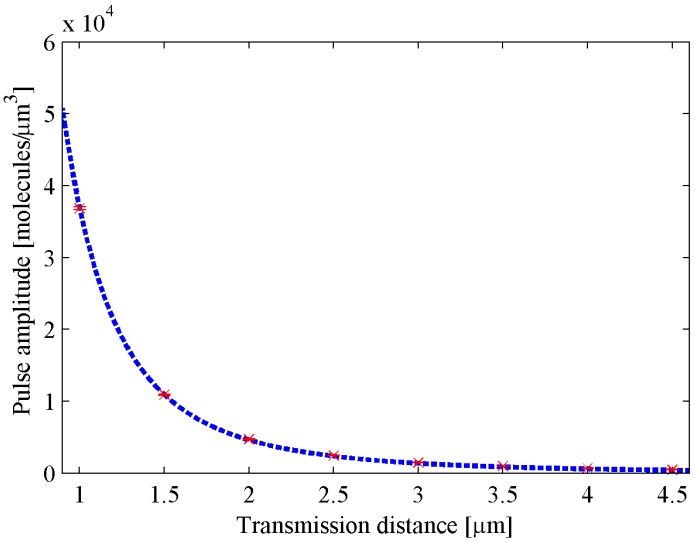

Figure 2.8: Pulse amplitude as a function of the transmission distance. The dashed blue line corresponds to the analytical expression and the red crosses show the simulation results with 99% confidence intervals.

a pulse transmission with the same characteristics as used to validate the pulse delay, the pulse amplitude is measured as a function of the transmission distance. Figure 2.8 shows a comparison of the analytical expression and the simulation results, which confirms the correctness of (2.5).

2.4.3 Pulse width

Another important metric in a scenario of DMC with amplitude detection is the pulse width, since it will be the main constraint on the achievable throughput. As it is usually done in EM communications, the pulse width is computed at the 50% level, i.e., the time interval at which the pulse has an amplitude greater than half of its maximum value:

$$c(d,t) = \frac{Q}{(4\pi Dt)^{3/2}} e^{-d^2/4Dt} = \frac{c_{max}}{2} = \frac{1}{2}\left(\frac{3}{2\pi e}\right)^{3/2} \frac{Q}{d^3}. \tag{2.6}$$

The following expression is obtained by isolating the time variable:

$$t = -\frac{d^2}{6DW\left(-\frac{1}{2^{2/3}e}\right)} \tag{2.7}$$

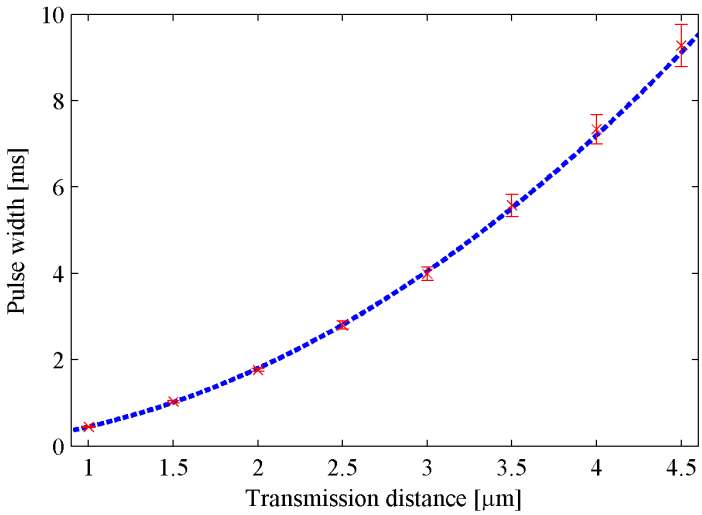

Figure 2.9: Pulse width as a function of the transmission distance. The dashed blue line corresponds to the analytical expression, and the red crosses show the simulation results with 99% confidence intervals.

where W is the Lambert W function [137]. This equation has two solutions, corresponding to the two time instants at which the pulse amplitude is equal to half of its maximum value. These instants are given by:

$$t_1 = \frac{0.0728}{D_C} d^2, \qquad t_2 = \frac{0.5229}{D_C} d^2. \tag{2.8}$$

Finally, the expression of the pulse width t_w is obtained by subtracting these two instants:

$$t_w = t_2 - t_1 = \frac{0.4501}{D_C} d^2. \tag{2.9}$$

In this case, as it happened with the pulse delay, the pulse width is inversely proportional to the diffusion coefficient of the medium. Therefore, the larger the diffusion coefficient is, the narrower the received pulses will be.

As before, the obtained expression is validated with *N3Sim*, using the same parameters as in the previous sections. Figure 2.9 shows that the simulation results are close to the values of the analytical expression, which confirms the validity of (2.9).

Achievable throughput

The expression of the pulse width also allows obtaining an estimate on the achievable throughput of the pulse-based modulation scheme in DMC. Let us consider the case where a nanosystem needs to transmit a bit stream. With this purpose, it may send a train of pulses by using different molecule types to represent the bits "0" and "1", respectively. In this case, the minimum separation between the transmitted pulses needs to be approximately equal to the pulse width at the receiver, so that pulses can be correctly distinguished and the information can be decoded (assuming that the transmitter and receiver are synchronized). The achievable throughput in this scenario is therefore approximately equal to the inverse of the pulse width at the receiver location.

The transmitter is able to compute the pulse width at the receiver by using Eq. (2.9) and it can set the interval between the transmitted pulses accordingly. For example, for a transmission distance of 200 nm, the received pulse width will be of 18 µs. Figure 2.10 represents the received signal when a train of pulses is transmitted by a nanosystem located 200 nm away with an interval between pulses equal to the pulse width at the receiver. The simulation results show a stream of distinguishable pulses and thus confirm that the transmitted signal can be correctly decoded by the receiver.

2.5 Energy detection

An alternative to the detection of molecular pulses by measuring their amplitude is that the receivers implement energy detectors to decode the transmitted information. In the scenario of energy detection, some of the metrics that have been identified in the amplitude detection case (such as the pulse delay) are still meaningful, but new communication metrics will become relevant as well.

In particular, in the amplitude detection case, the pulse amplitude determines the receiver sensitivity, i.e., the ability to distinguish whether the received signal represents a bit "0" or "1". In an energy detection scenario, however, a new communication metric needs to be analyzed to evaluate the receiver sensitivity, namely, the pulse energy.

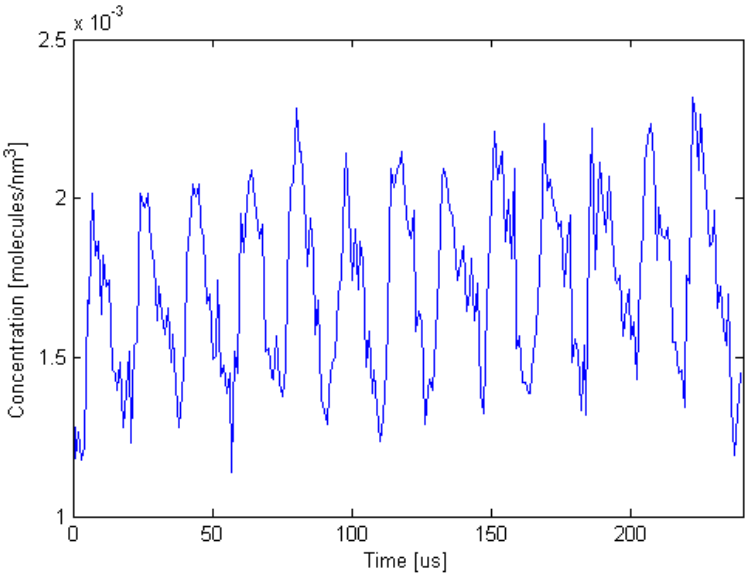

Figure 2.10: Concentration measured by the receiver when a train of molecular pulses is transmitted from a distance of 200 nm. The interval between pulses is equal to the pulse width at the receiver location.

Furthermore, as described in Section 2.4.3, the achievable throughput in DMC using amplitude detection is limited by the pulse width. As shown next, in an energy detection scenario, the pulse duration needs to be defined as the communication metric that will determine the maximum achievable throughput.

In what follows, analytical expressions for the two communication metrics that have just been identified, namely, the pulse energy and the pulse duration, are obtained. Further, they are validated by simulation and their impact in the performance of DMC using energy detection is discussed.

2.5.1 Pulse energy

The most important metric to consider in the energy detection case is the pulse energy; indeed, energy detectors will decode the received signals by measuring their energy and comparing it to a threshold, which will be a function of the expected pulse energy. Since the pulse energy in DMC is defined as the temporal sum of its molecular concentration, the energy of a molecular pulse can be

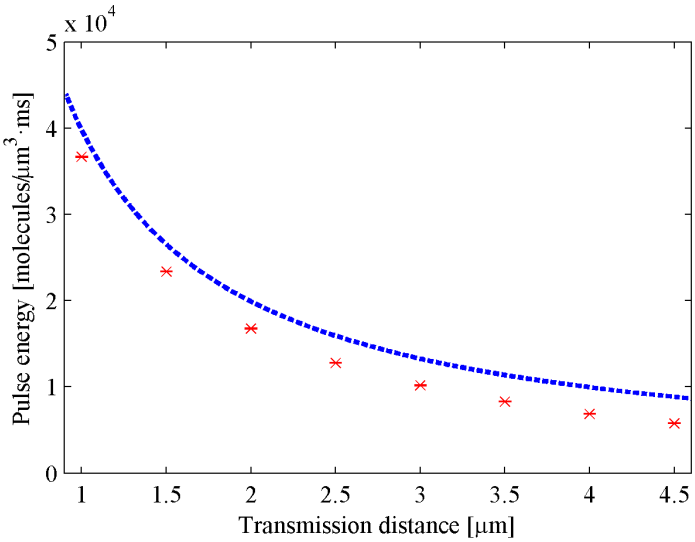

Figure 2.11: Pulse energy as a function of the transmission distance. The dashed blue line corresponds to the analytical expression, and the red crosses show the simulation results with 99% confidence intervals.

computed by integrating the pulse equation (2.1) over time:

$$E_p = \int_0^\infty c(d,t)\mathrm{d}t = \int_0^\infty \frac{Q}{(4\pi D_C t)^{3/2}} e^{-\frac{d^2}{4D_C t}} \mathrm{d}t = \frac{Q}{4\pi D_C d}. \tag{2.10}$$

In order to validate this result, as done in the previous sections, the transmission of a pulse of $5 \cdot 10^5$ molecules is simulated using *N3Sim*. Figure 2.11 shows a comparison between the analytical expression of the pulse energy (dashed blue line) and the averaged results after 30 simulation runs with 99% confidence intervals. In this case, even though the analytical and simulation results show a similar dependence with respect to the transmission distance, the values obtained by simulation are lower than the analytically-obtained pulse energy. The reason for this difference is that, since molecular pulses have an infinite tail due to the effect of diffusion (see Figure 2.1), a receiver would need an infinite time to measure the exact value of the pulse energy, i.e., that derived by solving the improper integral in (2.10). Since, in a practical scenario, receivers will only have a finite time to measure the pulse energy (e.g., the performed simulations have a duration of 50 ms), the pulse energy measured by a receiver will always have a lower value than the energy predicted by the analytical expression.

2.5.2 Pulse duration

As opposed to the pulse width in an amplitude detection scenario [130], it will be the pulse duration which will determine the achievable throughput in DMC using energy detection. As it was just observed, if the pulse duration were defined as the time needed by a receiver to measure the pulse energy E_p, it would have an infinite value. Instead, in order to allow receivers to detect molecular pulses in a finite amount of time, the pulse duration is defined as the time interval from the pulse transmission until the instant when a fraction γ of the pulse energy has reached the receiver location. In other words, the pulse duration is the time needed to measure an energy γE_p, where $0 \leq \gamma \leq 1$. The pulse duration t_D is computed by solving the integral equation:

$$\int_0^{t_D} c(d,t)\mathrm{d}t = \gamma E_p = \gamma \frac{Q}{4\pi D_C d} \tag{2.11}$$

which can be analytically solved and yields the following solution for the pulse duration:

$$t_D = \frac{d^2}{4D\ \mathrm{erfc}^{-1}(\gamma)^2} \tag{2.12}$$

where erfc^{-1} is the inverse complementary error function [138]. Figure 2.12 shows a semi-log plot of the pulse duration calculated by (2.12), as a function of γ, in a scenario of energy detection with a transmission distance $d = 2$ µm. As usual, the analytical results (solid blue line) are validated by simulation (black crosses). The pulse duration is also compared to the equivalent metric in the amplitude detection case, the pulse width (dashed red line), as obtained from (2.9).

As expected, the pulse duration increases monotonically with γ, the fraction of the pulse energy considered, and it tends to infinity when γ approaches one: $\lim_{\gamma \to 1} t_D = \infty$. Therefore, from the point of view of the pulse duration, lower values of γ yield a better performance. However, selecting a too low value of γ might cause detection errors due to diffusion noise [135]. Therefore, a realistic value for γ will probably be between 0.5 and 0.8. In the amplitude detection case, the pulse width is $t_w = 1.8$ ms. When comparing both scenarios, the pulse duration in the case of energy detection is found to be lower than the pulse width

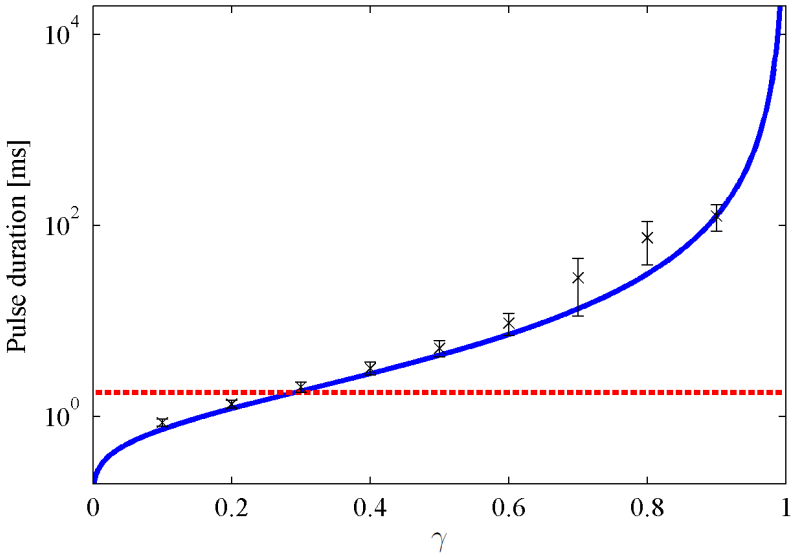

Figure 2.12: Semi-log plot of the pulse duration as a function of the fraction of the pulse energy required to detect a pulse γ. The solid blue line corresponds to the analytical expression, and the black crosses show the simulation results with 99% confidence intervals. The pulse width in an amplitude detection scenario (dashed red line) is shown for the sake of comparison.

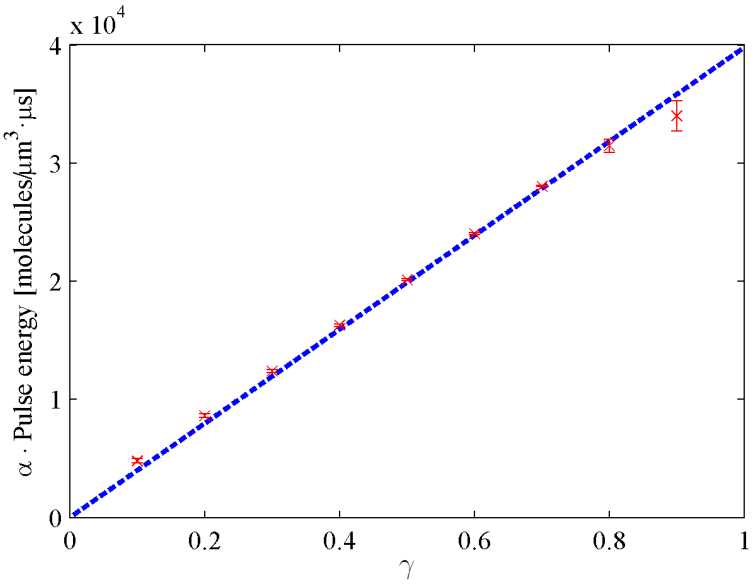

Figure 2.13: Required energy to detect a pulse, as a function of the fraction of the pulse energy required to detect a pulse γ. The dashed blue line corresponds to the analytical expression, and the red crosses show the simulation results with 99% confidence intervals.

for $\gamma < 0.292$, and higher otherwise. In particular, for realistic values of γ, the pulse duration will be significantly higher than the pulse width when amplitude detection is used. For instance, for energy detection with $\gamma = 0.7$, the pulse duration is almost one order of magnitude higher than the pulse width.

Furthermore, Figure 2.13 shows the required energy to detect a pulse γE_p, as a function of γ. The analytical results are obtained from (2.11) with a pulse of $Q = 10^3$ molecules transmitted to a distance $d = 2$ µm, whereas the simulations consider the energy measured by a receiver during the pulse duration t_D, as obtained from (2.12). Similarly, Figure 2.14 shows the pulse duration as a function of the transmission distance. In both cases, a very good agreement between the analytical results (blue dashed lines) and the simulations (red crosses) is observed, thus validating the derived expressions.

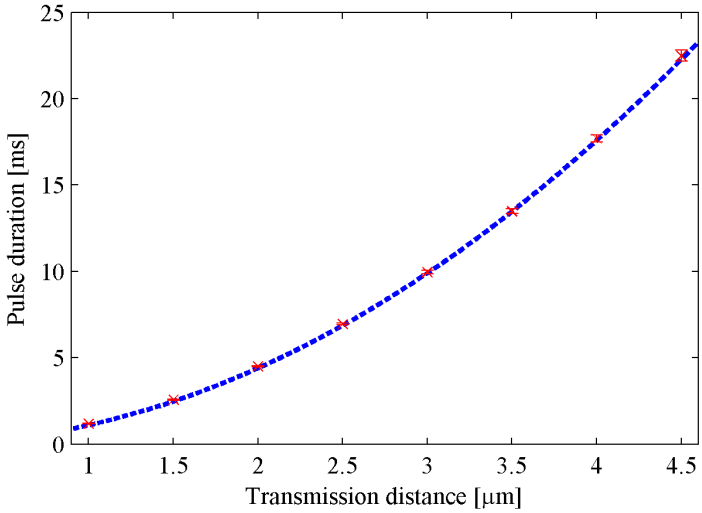

Figure 2.14: Pulse duration as a function of the transmission distance. The dashed blue line corresponds to the analytical expression, and the red crosses show the simulation results with 99% confidence intervals.

2.6 Scalability of detection techniques in DMC

It is of key interest to evaluate the scalability of the previously found communication metrics with respect to the transmission distance. Next, the results obtained in both the amplitude detection and energy detection cases in DMC are compared to their equivalent in traditional wireless communications.

Starting with the amplitude detection scenario, as observed in (2.4), the pulse delay is proportional to the square of the transmission distance, namely, $t_d = \Theta(d^2)$. The Big Theta notation means that the average propagation delay in DMC is proportional to the square of the transmission distance, even if its actual value will probably differ slightly due to the effect of random diffusion. This scalability trend is due to the stochastic nature of the Brownian motion underlying the diffusion process, which is fundamentally different from the constant wave propagation speed observed in EM communications. In the latter case, the propagation delay is obtained as the transmission distance divided by the wave propagation speed, namely, $t_d = \Theta(d)$.

Equation (2.5) shows that the amplitude of a molecular pulse is inversely proportional to the third power of the transmission distance, i.e., $c_{max} = \Theta(1/d^3)$.

This dependence shows again a difference with respect to the behavior of waves in traditional wireless communications, for which the free-space path loss is $A = \left(\frac{4\pi df}{c}\right)^2$, where f is the signal frequency and c the speed of light. Therefore, ignoring fading, the amplitude of EM pulses propagating in free space decreases proportionally to the square of the transmission distance, namely, $c_{max} = \Theta\left(1/d^2\right)$, in contrast with the behavior observed in a DMC scenario.

Furthermore, according to (2.9), the dependence of the pulse width in DMC on the transmission distance is $t_w = \Theta\left(d^2\right)$. Again, there is a clear difference with the wireless EM channel, for which the pulse width is independent from the transmission distance, namely, $t_w = \Theta(1)$. Also, the behavior of the DMC channel differs from that observed in optical communications, where chromatic dispersion causes the pulse width to increase proportionally to the transmission distance, i.e., $t_w = \Theta(d)$, at a slower rate than in DMC.

With respect to the pulse energy in DMC, equation (2.10) shows that it scales as $E_p = \Theta\left(1/d\right)$. In traditional wireless communications, since there is no signal distortion in a free-space environment, the scalability of the pulse energy is proportional to that of its amplitude, i.e., $E_p = \Theta\left(1/d^2\right)$. In this case, as opposed to the previous ones, DMC using energy detection shows a scalability advantage with respect to traditional wireless communications. Moreover, the pulse energy scales better than the pulse amplitude as the transmission distance increases. In other words, an energy detection scheme will allow successful transmissions at longer distances than one based on amplitude detection. Intuitively, the reason of this difference is that, even though the diffusion process severely reduces the amplitude of the transmitted pulses, it also increases their width; therefore, the energy of a molecular pulse decreases more slowly than its amplitude as the transmission distance increases.

Finally, (2.12) shows that the pulse duration scales with the transmission distance as $t_D = \Theta(d^2)$. As it happened with the pulse width, the signal duration in traditional wireless communications is independent of the transmission distance: $t_D = \Theta(1)$. In this case, the scalability pattern of the pulse duration matches that observed for the pulse width in the amplitude detection case. Therefore, even though in a typical scenario the pulse duration will be higher than the pulse width (as previously seen in Sec. 2.5.2), and thus the achievable throughput with en-

ergy detection will be lower than with amplitude detection, both pulse detection techniques show the same scalability trend in terms of the achievable throughput as a function of the distance.

In consequence, both methods, energy detection and amplitude detection, have their own advantages and drawbacks when they are used in DMC. On the one hand, the receiver sensitivity scales better in the energy detection scenario with respect to when amplitude detection is used. On the other hand, amplitude detection yields in general a higher achievable throughput than energy detection, even though they both scale identically with respect to the distance.

This guideline can be observed in Figure 2.15, which shows the reception of a molecular pulse for transmission distances of 2 µm (left) and 3 µm (right). The transmitted molecular pulse consists of $5 \cdot 10^6$ molecules released at time $t = 0$, and the pulse duration is calculated as the time after which a fraction $\gamma = 0.5$ of the total pulse energy is measured by the receiver. On the one hand, in terms of receiver sensitivity, the pulse amplitude c_{max} at a transmission distance of $d = 3$ µm is reduced by a factor of 70% with respect to its value for $d = 2$ µm, whereas the decrease in the pulse energy E_p is much less severe, at 33%. This observation is in agreement with the prediction that energy detection scales better than amplitude detection as the transmission distance increases. On the other hand, the pulse width t_w is found to have a lower value than the pulse duration t_D in both cases, which confirms that, for a given transmission distance, amplitude detection will allow a higher achievable throughput than energy detection in DMC networks.

To summarize, energy detection is envisaged as a more feasible alternative for DMC when the signal attenuation represents the main limitation, i.e., for long transmission distances. Conversely, amplitude detection may prove more useful in scenarios with low signal attenuation, i.e., for short transmission distances, since it will allow nanosystems to communicate information at a higher rate. Table 2.1 compares the scalability of the analyzed communication metrics in DMC and traditional wireless communications.

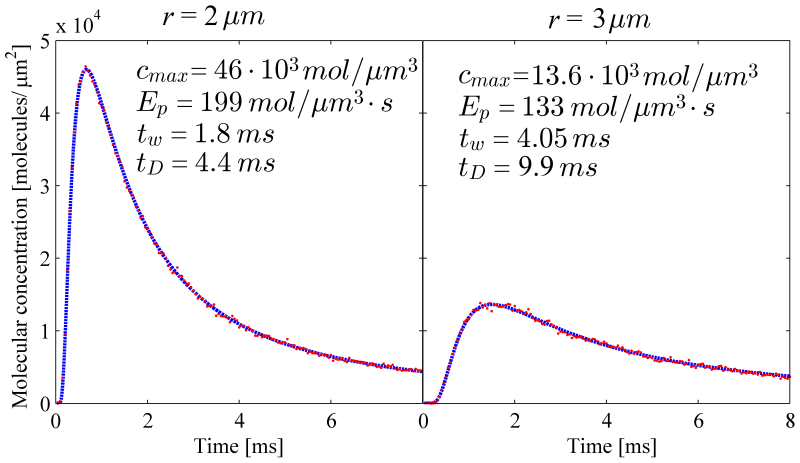

Figure 2.15: Molecular concentration as a function of time measured by a receiver located at a distance of 2 µm (left) and 3 µm (right) from the transmitter. A pulse of $5 \cdot 10^6$ molecules is transmitted at time $t = 0$. The blue dashed line shows the analytical results and the red dots correspond to simulation results. The impact of the transmission distance on the pulse amplitude c_{max}, the pulse energy E_p, the pulse width t_w and the pulse duration t_D can be observed.

Metric	**DMC**	**Traditional wireless communications**
Pulse delay	$\Theta(d^2)$	$\Theta(d)$
Pulse amplitude	$\Theta(1/d^3)$	$\Theta(1/d^2)$
Pulse width	$\Theta(d^2)$	$\Theta(1)$
Pulse energy	$\Theta(1/d)$	$\Theta(1/d^2)$
Pulse duration	$\Theta(d^2)$	$\Theta(1)$

Table 2.1: Communication metrics in DMC and traditional wireless communications. d stands for the transmission distance.

2.7 Summary and concluding remarks

In this chapter, the physical channel in DMC has been characterized and the performance of two techniques to detect transmitted signals in the proposed scenario, namely, amplitude detection and energy detection, has been evaluated. First, the envisaged scenario is described, where molecules emitted by transmitter nanosystems diffuse throughout the medium according to Fick's laws of diffusion. Next, the impulse response, the transfer function and the group delay of the DMC channel are obtained.

A pulse-based modulation scheme has been proposed which seems particularly well-suited to the DMC environment. Based on this scheme, the performance of two techniques to detect transmitted signals in DMC networks, namely, amplitude detection and energy detection, has been evaluated. For each of them, several metrics of key importance to evaluate the performance of a DMC system from the communication standpoint have been identified. These are the pulse delay, the pulse amplitude and the pulse width in the amplitude detection case, and the pulse delay, the pulse energy and the pulse duration in the scenario of energy detection. Analytical expressions for each of these performance metrics have been obtained and validated by simulation.

Finally, the differences in the scalability of the obtained metrics for DMC with respect to their equivalent in traditional wireless communications have been outlined. The comparison of the scalability of the performance metrics in the amplitude detection and energy detection scenarios brought to the conclusion that energy detection may be a more feasible alternative when the transmission distances are relatively high, whereas amplitude detection will allow achieving a higher transmission rate in scenarios with low transmission distances.

The future work in this direction might include the biological implementation of the proposed detection mechanisms, and the design of coding schemes and multiple access control protocols for DMC networks. Moreover, the analysis of different sources of molecular noise, such as considering a background molecular concentration or the interference when more than one transmitter is simultaneously emitting molecules, may provide further guidelines for designers of future DMC networks.

Chapter 3

Diffusion-based molecular communication networks

This chapter analyzes the main challenges and principles in the design of DMC networks. Chapter 2 outlined two alternatives for the detection of transmitted pulses: amplitude detection [130] and energy detection [139]. In each of these cases, several communication metrics become relevant, namely, the pulse delay, the pulse amplitude and the pulse width in the amplitude detection scenario, and the pulse delay, the pulse energy and the pulse duration, in the energy detection scheme.

The analysis of these communication metrics led to the conclusion that, due to the uniqueness of the physical channel of DMC with respect to that of traditional wireless communications, there exist fundamental differences in the scalability of the communication metrics in both scenarios. These differences will require revisiting most of the protocols and techniques developed for traditional wireless networks in order to adapt them to DMC networks. For this reason, in this chapter a systematic analysis of the networking challenges in DMC is carried out, identifying the principles over which DMC networks will take base. Throughout this analysis, a significant effort is made to take very few assumptions with respect to the biological implementation of the system; therefore, both the challenges and the DMC principles described are as technology-agnostic as possible.

The remainder of this chapter is organized as follows. Section 3.1 briefly

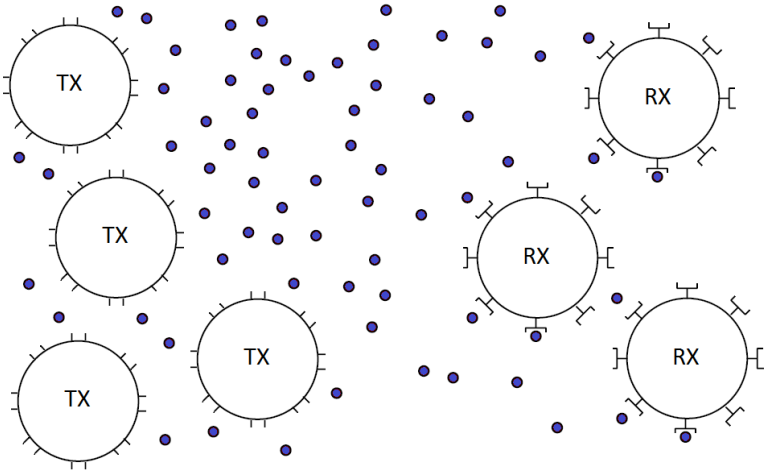

Figure 3.1: Schematic diagram of a multipoint-to-multipoint DMC network.

describes the scenario of DMC networks and enumerates the considered assumptions. Section 3.2 identifies the main aspects that make DMC networks radically different from traditional wireless networks, and the challenges they introduce in the design of protocols and techniques for DMC networks. Finally, Section 3.3 summarizes this chapter.

3.1 DMC network scenario

A DMC network consists of a set of nanosystems located in a fluid medium which communicate by means of a DMC process, as described in Section 2.1. In summary, a DMC process is composed of three main phases: first, transmitter nanosystems release a pattern of molecules which encodes the information; second, the emitted molecules cause a variation in their local concentration which propagates throughout the medium due to a diffusion process; and third, receivers estimate the transmitted signal by measuring the local concentration of molecules in their neighborhood. Figure 3.1 illustrates a scenario of multipoint-to-multipoint DMC network with multiple transmitters and receivers, as is envisaged in future nanonetworks.

Next, the main assumptions taken in the considered DMC network are described, and a technique that may allow simultaneous transmissions by different

transmitter nanosystems is briefly outlined.

3.1.1 Main assumptions

For this analysis, a DMC network scenario with the following assumptions is considered:

1. Digital communications are contemplated. In other words, the information to be transmitted is encoded in a bit stream. Other mechanisms could consider analog modulation schemes, for instance similar to the traditional AM or FM techniques [26].

2. In the envisaged scenario, the concentration of emitted molecules is much lower than the concentration of the fluid molecules. As described in Section 2.1, in this scenario the interactions among the emitted molecules can be neglected. In consequence, each of the molecules released by a transmitter moves according to Brownian motion, a stochastic process with independent increments which are normally distributed with zero mean. Since the movement of each molecule is independent, molecular diffusion can be modeled by Fick's laws of diffusion [41] with a homogeneous diffusion coefficient both in space and time.

3. Even though nanosystems are expected to have limited memory storage and be capable of performing only simple calculations, they are able to reproduce the algorithmic behavior of computers and compute the same set of mathematical operations. Indeed, the latest advances in synthetic biology are allowing the development of small biocomputers [140].

4. Motivated by the expectedly low complexity of nanosystems, which prevents the use of advanced modulations, a digital pulse-based modulation is assumed to encode the information, such as that described in Section 2.1. Even though most of the results derived in this work apply to any modulation type, this assumption allows the quantitative modeling of the signal propagation in DMC networks. According to this scheme, a transmitter

nanosystem encodes the information into pulses of molecules, which are instantaneously released to the environment. The release of a molecular pulse creates a delta in the molecular concentration at the transmitter location, and its propagation throughout the environment can be analytically modeled by solving Fick's laws of diffusion. The molecular concentration at the receiver location as a function of time, after the transmitter has released a pulse of molecules, is illustrated in Figure 2.1.

5. The focus is set on the application scenario of nanonetworks, where nanosystems represent the nodes of the network. Therefore, a general case of multipoint-to-multipoint communication among nanosystems, with multiple transmitters and receivers communicating in a shared medium, is considered.

3.1.2 Multiple transmitters

An interesting feature of DMC that may facilitate the construction of DMC networks is the use of different molecule types. Given the assumption that the emitted molecules do not interact among them, the proposed DMC scheme allows for simultaneous transmissions by multiple nanosystems. Interferences may be avoided by having transmitters use different molecule types, in a mechanism known as Molecular Division Multiple Access (MDMA) [32]. In order to demonstrate the feasibility of a scenario where multiple nanosystems are transmitting simultaneously, a simulation where two transmitters emit a pulse of molecules at the same time instant is performed. Figure 3.2 shows the concentration measured by a receiver in this scenario. The transmitter nanosystems are located at a distance of 300 and 400 nm, respectively, and they use different molecule types in order to avoid the collision of the transmitted pulses. Since the transmitted molecules do not interact, the pulses are orthogonal and they can be successfully decoded by the receiver nanosystem.

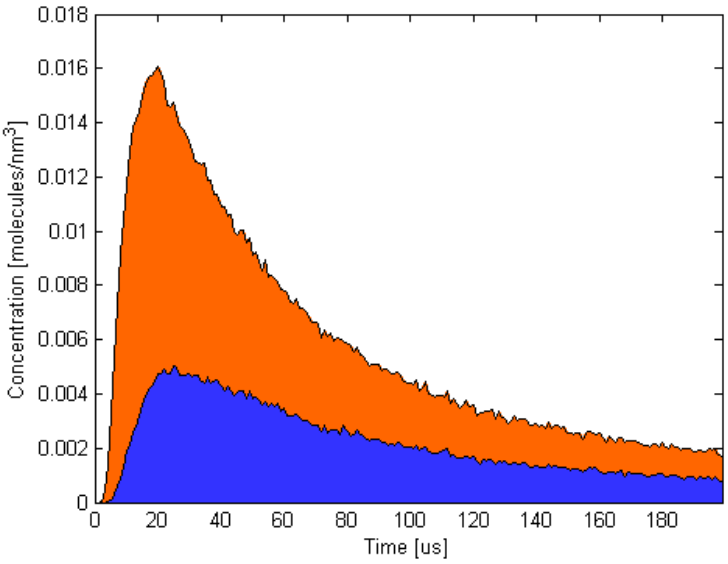

Figure 3.2: Concentration measured by a receiver nanosystem when two transmitters simultaneously emit a molecular pulse. Transmitter 1 (orange) is located at a distance of 300 nm, and transmitter 2 (blue) at 400 nm.

3.2 Networking challenges in DMC networks

In the DMC network scenario described in the previous section, key communication metrics, such as the attenuation, the delay and the energy, scale differently with respect to traditional wireless communications. A comparison of the scalability of the communication metrics in DMC and traditional wireless communications was shown in Table 2.1. Due to these differences, the main challenges that appear in the design of DMC networks are identified next.

3.2.1 Propagation delay

The rapid increase of the propagation delay as a function of the distance, $t_d = \Theta\left(d^2\right)$, will become a huge limitation in DMC networks. For instance, for transmission distances of just a few tens of micrometers, the delay will be in the order of 1 second, and given its increase with the square of the transmission distance, it will become excessive very rapidly. This high delay will almost prevent using handshake-based protocols, such as the TCP 3-way handshake, very common in

traditional wireless networks. For the same reason, retransmissions will also be very expensive in DMC. In traditional wireless communications, retransmissions, needed when a packet is not correctly received, are often implemented by means of negative acknowledgments. However, in scenarios where the propagation delay is specially high, such as DMC with a relatively long transmission distance, it is possible that even the use of acknowledgments becomes prohibitive. Therefore, the design DMC networks should prioritize maximizing the probability of correctly receiving the transmitted information, thereby minimizing the number of retransmissions needed.

Another particularity of DMC networks related to their expectedly high propagation delay concerns the Medium Access Control (MAC). In traditional wireless networks, the most widespread MAC protocol is CSMA, which is based in sensing the medium in order to verify the absence of traffic before transmitting. However, the high delay in DMC prevents the use of carrier sensing; for instance, at a given time instant, the transmitter may sense a channel free of molecules, but the medium may be busy at the receiver location.

An alternative MAC protocol which has been proposed for DMC is Molecular Division Multiple Access (MDMA) [32]. This technique uses different molecule types in order to perform several simultaneous transmissions, sharing the same medium but without interfering each other. Some concerns regarding this technique include the choice of molecule types to be used by different transmitters, so that they do not interact among them and that receivers are able to discern each of the received molecules from one another.

An additional related challenge is user synchronization. Synchronous communication protocols require that the transmitter and receiver are synchronized. However, the long and random propagation delay in DMC makes achieving synchronization among nodes a challenging task. Quorum Sensing, a mechanism used by bacteria and social insects to coordinate their behavior, might also be used to achieve synchronization in a DMC scenario [141]. However, due to the randomness of the diffusion process, there are doubts regarding the level of synchronization that can be achieved with this technique.

3.2.2 Channel attenuation

Another important bottleneck in the performance of DMC networks is the channel attenuation, which will limit the transmission range of nodes in a DMC network. The channel attenuation depends greatly on the method used by the receivers to detect the transmitted pulses of molecules. As previously described in Section 2.6, the pulse amplitude and the pulse energy scale very differently with respect to the transmission distance: $\Theta\left(1/d^3\right)$ and $\Theta\left(1/d\right)$, respectively. Therefore, in terms of channel attenuation, energy detection seems better suited to a DMC scenario than amplitude detection.

A complementary approach to combat channel attenuation considers using a cooperative approach for the transmission of pulses [142], as opposed to the selfish approach typical in traditional wireless networks. Following this approach, a group of nodes coordinate to simultaneously transmit a molecular pulse. As a result, their individual contributions aggregate into a pulse with a higher amplitude. Of course, this approach requires that the nodes are synchronized (e.g., by means of Quorum Sensing, as previously described). In any case, it should be investigated whether the performance of this new signal amplification technique for DMC outperforms that of protocols widely used in traditional wireless networks, such as multi-hopping.

3.2.3 Channel distortion

Because of the stochastic nature of Brownian motion, the physical channel of DMC distorts the transmitted pulses. The molecular concentration, as a function of time, measured by a receiver nanosystem after a transmitter releases a spike of molecules was depicted in Figure 2.1. This figure shows that the concentration measured by the receiver no longer resembles a spike, but it has an infinite tail. This huge distortion of the transmitted pulses presents a further challenge to their successful detection and represents the main limitation in the achievable throughput in DMC.

From an amplitude detection perspective, the channel distortion causes the width of the transmitted pulses to increase with the transmission distance. The pulse width will limit the minimum time interval between two consecutive pulses

and, therefore, will introduce an upper bound on the achievable throughput. On the other hand, using energy detection, it is the pulse duration which limits the maximum bandwidth. Even though both the pulse width and the pulse duration increase proportionally to the square of the transmission distance, i.e., $\Theta(d^2)$, the pulse duration was found to be around one order of magnitude higher than the pulse width in a typical scenario [139]. In consequence, and as opposed to what happened with regards to channel attenuation, amplitude detection offers a better performance than energy detection in terms of achievable throughput in DMC networks.

Furthermore, the pulse distortion also creates intersymbol interference (ISI). In contrast with traditional wireless communications, where the ISI can be greatly mitigated by means of adaptive equalization, the interference caused by the infinite tails of molecular pulses in DMC is hard to avoid. Therefore, novel techniques to minimize the effect of ISI in DMC need to be investigated, such as absorbing the molecules from the previous transmissions by the receivers, or using degrading molecules in order to simulate a Time To Live (TTL) mechanism in the emitted molecules.

3.2.4 Limited capabilities of nanosystems

Due to their reduced size, in the order of a few micrometers, nanosystems are expected to have strict limitations in terms of processing power, memory storage, available energy and number of molecules they can emit. As an example, a memory device with a record storage density of 3.6 Tbit/inch^2 has been demonstrated [143]. With this storage density, a memory device with a size of 10 µm^2 (in line with the expected size of the envisaged nanosystems) would have a capacity of just 7 kbytes.

These constraints will not allow the use of computationally complex modulations and protocols, such as the ones used in traditional wireless networks. On the contrary, they represent the main motivation for the use of simple opportunistic techniques, such as the pulse-based modulation assumed in this work. However, one cannot forget that the main drawback of these simple modulations and coding schemes is that, in order to achieve a target throughput, they require

a higher signal-to-noise ratio at the receiver than more complex techniques.

Furthermore, in order to minimize the number of retransmissions (because of the high propagation delay in DMC), error correcting codes will be needed. Given the limitations in terms of processing power of nanosystems, very simple error correcting coding schemes, such as repetition codes, may be the most suitable alternative in a DMC scenario.

3.2.5 Node mobility

In a typical scenario of DMC, such as an intra-body network [61], the network nodes will be suspended in a fluid medium. In this case, their movement can be modeled as Brownian motion, i.e., the node trajectory (as it happened with the emitted molecules) will have an unpredictable pattern. Note that, even though both the emitted molecules and the network nodes move according to Brownian motion, the latter will have a much lower diffusion coefficient due to their larger size, and therefore they will move at a much slower speed.

A paradigm that takes advantage of node mobility to improve the communication performance is that of Delay Tolerant Networks [144]. In these networks, whenever some information is ready to send, it is not immediately transmitted. Instead, the data is stored in memory and the transmission is postponed until the transmitter detects that its location is close enough to the intended recipients. Therefore, transmitters can select their emission time in order to achieve a successful communication.

In order to apply this technique, a mechanism to measure the distance between nanosystems is needed. Besides its other applications, Quorum Sensing could also be used for distance estimation in DMC. Indeed, using Quorum Sensing bacteria are able to estimate their local population by sensing the concentration of signaling molecules known as autoinducers, which are continuously released by the bacteria [145]. Similarly, receiver nanosystems could release a special type of molecules that would allow transmitters to estimate their distance to potential receivers. Another option to estimate the distance between nanosystems would be to measure the round-trip time of a pulse of molecules released by the transmitter [146].

However, as previously explained, nanosystems might not have enough memory and processing power to implement these techniques. Therefore, it seems difficult to exploit the node mobility to improve the communication performance of DMC networks.

3.2.6 High node density

A characteristic of most DMC networks in realistic scenarios will be the very high number of nodes located in a small region. For instance, for a transmission range of 100 µm, the number of nodes required to cover a volume of just 1 cm^2 is in the order of 10^6.

With such a high number of nodes, and given the limited capabilities of nanosystems, setting a unique address to each network node, as is done in traditional wireless networks, will become nearly impossible. For instance, aspects such as updating the routing tables of nanosystems or assigning a unique address to a new node entering the network, would become very challenging in the constantly-changing scenario of DMC networks. Instead, an alternative approach would be setting the address to identify the nanosystem *type* (e.g., nanosensor, nanoactuator, etc.), rather than the individual nanosystem. This way, the previous challenges would be greatly simplified.

Moreover, protocols where nodes compete to access a shared medium do not seem applicable in DMC networks, for two main reasons. First, due to the high number of nodes, it is expected that many of them would be simultaneously competing for the channel at any time. Second, due to the high propagation delay, after every transmission the channel would be busy for a long period of time before it can be reused by another transmitter.

A more feasible alternative for dense networks are cooperative protocols, which have already been proposed for dense wireless networks [147]. Another example of a cooperative approach is the already-mentioned Quorum Sensing.

Limitation	Challenge	Proposed technique
Propagation delay	MAC	MDMA
Propagation delay	Synchronization	Quorum Sensing
Attenuation	Signal detection	Energy detection
Distortion	Bandwidth	Amplitude detection
Distortion	ISI	TTL / Molecule absorption
Node simplicity	Modulation	Pulse-based modulation
Node simplicity	Coding	Repetition codes
Node density	Addressing	Nanosystem type addressing
Attenuation / density	Signal transmission	Cooperative amplification

Table 3.1: Main guidelines for DMC networks.

3.3 Summary and concluding remarks

This chapter has considered a DMC network where nodes transmit information using a pulse-based modulation. Based on this scenario, some of the most relevant design challenges and principles that will appear in future DMC networks have been described. In order to make the obtained results general and technology-agnostic, as few assumptions as possible have been taken.

Fundamental differences between of DMC and traditional wireless communications, such as the propagation delay, the channel distortion and the node mobility, have been identified. Due to the uniqueness of the physical channel of DMC, a new network architecture needs to be developed for DMC networks. Indeed, many of the protocols and techniques used in traditional wireless networks cannot be directly applied to this novel networking paradigm, and more suitable alternatives for a DMC scenario have been proposed. These results, which are detailed in Section 3.2 and summarized in Table 3.1, provide useful guidelines for designers of future DMC networks.

Chapter 4

Analysis of graphene RF plasmonic antennas

This chapter presents a systematic study of graphene RF plasmonic antennas, or *graphennas* [66, 148, 65]. A graphenna, shown in Figure 4.1, is modeled as a rectangular patch made of graphene with length L and width W, supported by a dielectric substrate of thickness D. The graphenna is illuminated by a plane wave linearly polarized along the patch length.

As outlined in Section 1.3.2, graphennas with a size of a few µm show plasmonic effects which allow them to radiate EM waves in the terahertz band. For this reason, they are envisaged to allow the implementation of wireless communications among nanosystems.

The remainder of this chapter is organized as follows. In Section 4.1, the expression used to model the electrical conductivity of graphene is presented, and two different approaches to numerically model a graphene patch are described and compared. Section 4.2 analyzes the propagation of SPP waves in graphene, by means of their dispersion relation, and some of their main properties. This model is used to obtain the resonant frequency of a graphenna both analytically and numerically. Section 4.3 evaluates the extinction, absorption and scattering cross sections of a graphenna. Section 4.4 contains a parametric study of the graphenna resonances. The dependence of several key properties of graphennas is found as a function of several parameters, such as the antenna dimensions and

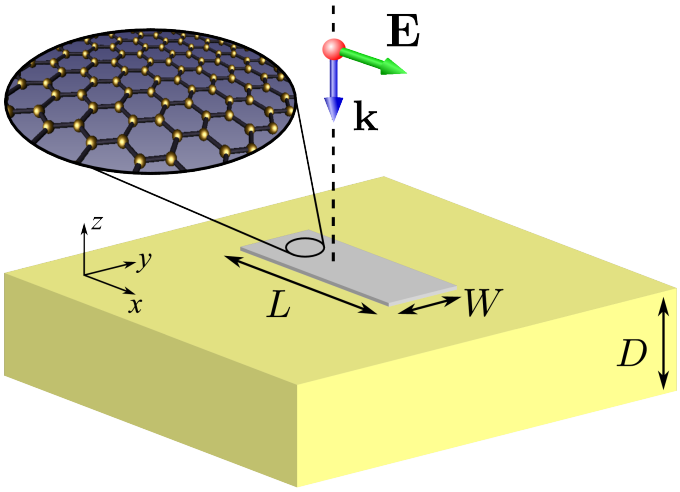

Figure 4.1: Sketch of the graphenna under consideration.

the applied chemical potential. The results show that the radiation properties of graphennas can be dynamically tuned in a wide range. In Section 4.5, the resonant frequency and the radiation diagram of both antenna types are compared. Section 4.6 describes a technique to feed an EM signal into graphennas by means of a photoconductive source. Finally, Section 4.7 summarizes this chapter.

4.1 Electrical conductivity of graphene

The radiation properties of graphennas are mainly determined by the highly frequency-dependent character of the graphene electrical conductivity. The conductivity of graphene has been studied both for DC and for frequencies that range from the terahertz band (0.1-10 THz) up to the visible spectrum [149, 150, 151, 152, 153]. In particular, the infrared conductivity of graphene sheets at zero chemical potential has been found to be essentially independent of the frequency and equal to $\sigma_0 = \pi e^2/2h$ (where e refers to the electron charge and h refers to the Planck constant). This result has been experimentally validated by different groups [154, 155, 156]. However, this expression is only valid for photon energies larger than 0.5 eV [149] or, equivalently, for frequencies higher than 120 THz. The graphene conductivity at lower frequencies has been shown to drastically change with the frequency, the temperature or the carrier density.

Graphennas are envisaged to have a length and width in the order of a few micrometers [91, 66, 93]. Since it has been experimentally demonstrated that edge effects on the graphene conductivity only appear in structures with lateral dimensions considerably smaller than 100 nm [157], in this analysis the edge effects are disregarded and the electrical conductivity model developed for infinitely large two-dimensional graphene sheets is used.

The surface conductivity of an infinite graphene film in the far infrared/terahertz range can be calculated by means of the Kubo formalism [158, 151]. Within the random-phase approximation, the surface conductivity can be represented in a local form with a Drude-like intraband contribution. This conductivity model has also been experimentally validated [159, 160, 161]. The graphene conductivity σ is obtained as the addition of its intraband contribution σ_{intra}, given by [100]

$$\sigma_{\text{intra}}(\omega) = \frac{2e^2}{\pi\hbar}\frac{k_B T}{\hbar}\ln\left[2\cosh\left[\frac{\mu_c}{2k_B T}\right]\right]\frac{\mathrm{i}}{\omega + \mathrm{i}\tau^{-1}}, \tag{4.1}$$

and the interband contribution σ_{inter}, which is given by [100]

$$\sigma_{\text{inter}}(\omega) = \frac{e^2}{4\hbar}\left(H\left(\frac{\omega}{2}\right) + \mathrm{i}\frac{4\omega}{\pi}\int_0^\infty \mathrm{d}\epsilon\,\frac{H(\epsilon) - H(\omega/2)}{\omega^2 - 4\epsilon^2}\right) \tag{4.2}$$

where $\hbar$ is the reduced Planck's constant, k_B the Boltzmann constant, T the temperature, μ_c the applied chemical potential and τ the relaxation time of graphene. The relaxation time is obtained as $\tau = \hbar\mu_g\sqrt{\pi n}/ev_F$, where μ_g is the electron mobility in graphene, which depends on the quality of graphene and the dielectric substrate, amongst others, $n = 4\pi(\mu_c/hv_F)^2$ the number of electrons and $v_F = c/300$ the Fermi velocity. $H(\epsilon)$ is defined as

$$H(\epsilon) = \frac{\sinh(\hbar\epsilon/k_B T)}{\cosh(\mu_c/k_B T) + \cosh(\hbar\epsilon/k_B T)}. \tag{4.3}$$

The electrical conductivity of graphene presents a clear dependence on two key parameters: the relaxation time τ, which is directly related to the quality of the graphene sample, and the chemical potential μ_c, which depends on the electrostatic bias voltage applied to graphene. The influence of these two parameters in the performance of graphennas is evaluated in Section 4.4.

In the frequency region of interest (below 5 THz), the intraband contribution

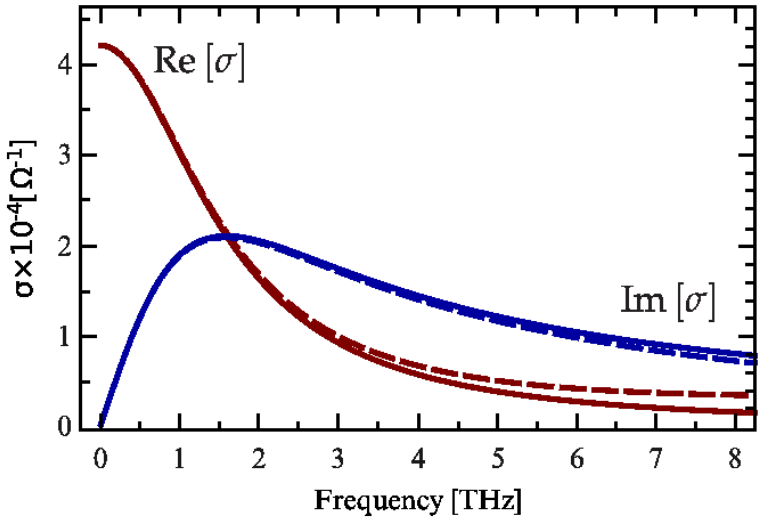

Figure 4.2: Real and imaginary part of the total conductivity (solid lines) and the intraband conductivity (dashed lines) of graphene at room temperature ($T = 300$ K) and zero electrostatic bias ($\mu_c = 0$ eV).

(4.1) dominates [162, 65]. This is shown in Figure 4.2, where the frequency dependence of the real and imaginary part of the intraband conductivity σ_{intra} and the total conductivity σ are compared at room temperature ($T = 300$ K), relaxation time $\tau = 0.1$ ps and zero electrostatic bias ($\mu_c = 0$ eV) [65].

4.1.1 Numerical methods

The evaluation of the radiation performance of a graphenna is performed by means of numerical calculations with the EM simulation tool FEKO [163], based on the method of moments with surface equivalence principle. The EM fields in the graphenna are solved by coupling the phenomenological model of the electrical conductivity of graphene with the Maxwell's equations. The major challenge here is to model an infinitesimally thin graphene layer using a finite-size discretization of the space, as needed to perform numerical calculations.

In what follows, two methods that can be used to model a graphene sheet in an EM simulation framework are proposed and compared. The first technique consists in approximating a graphene layer by an equivalent thin slab with a small, but finite, thickness. The propagation of the electromagnetic fields within the slab

is modeled by assigning to it a normalized effective conductivity $\overleftrightarrow{\sigma}$ [108, 100]

$$\overleftrightarrow{\sigma} = \begin{pmatrix} \sigma/\Delta & 0 & 0 \\ 0 & \sigma/\Delta & 0 \\ 0 & 0 & 0 \end{pmatrix} \tag{4.4}$$

where Δ is the thickness of the equivalent slab and the graphene sheet is located in the x-y plane, as in Figure 4.1. The tensor structure of the conductivity (4.4) together with the relation $\lim_{\Delta\to 0} 1/\Delta = \delta(z)$ ensure that, in the infinitesimally thin slab limit, the induced current is purely two-dimensional. The main drawback of this method is that a realistic model of graphene will have a length L much larger than its thickness Δ, resulting in a very high aspect ratio ($L/\Delta \sim 1000$). The numerical computation of the electromagnetic fields in such a structure will therefore require a very high mesh density, leading to a high computational cost.

As an alternative to treat this problem with lower computational costs, the graphene sheet can be modeled as an equivalent impedance surface [66, 164]. The surface impedance $Z_s = 1/\sigma$ connects the tangential component of the electric field on the surface with the electric surface current, $\mathbf{E}_\tau|_{z=0} = Z_s \mathbf{J}_{\text{surf}}$. Taking into account that the current induced in the graphene layer is purely superficial and it is related to the tangential component of the electric field via the surface conductivity σ as $\mathbf{J}_{\text{surf}} = \sigma\, \mathbf{E}_\tau|_{z=0}$, the boundary conditions at the graphene interface can be defined as

$$\hat{\mathbf{n}} \times \left[\mathbf{H}|_{z=+0} - \mathbf{H}|_{z=-0}\right] = \mathbf{J}_{\text{surf}} = \frac{1}{Z_s}\, \mathbf{E}_\tau|_{z=0}\,, \tag{4.5}$$

where $\mathbf{n}$ is the unit vector in the normal direction to the surface and $\mathbf{H}$ is the magnetic field. The boundary conditions (4.5) fully determine the electromagnetic problem and can be solved numerically using a computational scheme of choice.

Figure 4.3 contains a comparison between the equivalent slab model and the surface impedance model. The solid lines show the extinction cross section (see Section 4.3 for details) of the graphenna as a function of frequency when the antenna is modeled as a 10 µm-wide graphene patch with a length $L = 5$ µm and an effective conductivity as defined in (4.4), for different antenna thicknesses:

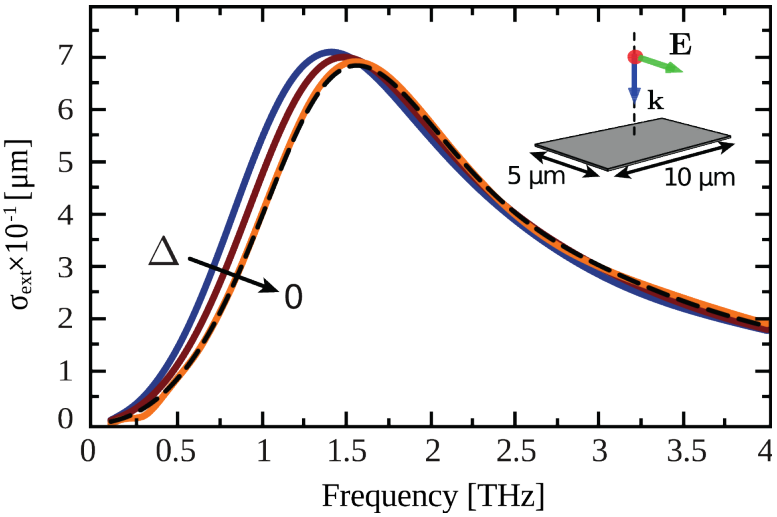

Figure 4.3: Extinction cross section per unit width of a 10 μm wide graphenna with length $L = 5$ μm. Results of the surface impedance model (dashed black line) and the equivalent slab model (solid lines) are shown at room temperature ($T = 300$ K) and zero electrostatic bias ($\mu_c = 0$ eV). The thicknesses of the equivalent graphene slab Δ are 500 nm, 200 nm and 5 nm, from left to right.

500 nm, 200 nm and 5 nm, from left to right. The dashed line corresponds to the surface impedance model. It can be seen that the equivalent slab model converges to the surface impedance model as the equivalent slab thickness is reduced, while simultaneously requiring a denser mesh (higher computational costs) for a smaller equivalent thickness. In what follows, the surface impedance model is used to numerically characterize the graphene patch, due to its accuracy and efficiency.

4.2 Surface plasmon polaritons in graphennas

In order to understand the resonant behavior of graphennas, a simple Fabry-Perot (FP) model for the graphene patch is considered. An infinite graphene layer placed on the air-dielectric interface supports transverse-magnetic (TM) Surface Plasmon Polariton (SPP) waves with a dispersion relation given by [107]

$$\frac{1}{\sqrt{k_{\mathrm{SPP}}^2 - \frac{\omega^2}{c^2}}} + \frac{\varepsilon}{\sqrt{k_{\mathrm{SPP}}^2 - \varepsilon\frac{\omega^2}{c^2}}} = -\mathrm{i}\frac{\sigma(\omega)}{\omega\varepsilon_0} \tag{4.6}$$

where $k_{\mathrm{SPP}} = 2\pi/\lambda_{\mathrm{SPP}}$ is the SPP wavenumber and $\omega = 2\pi f$ its angular frequency. ε_0 and ε are the absolute permittivity of free space and the dielectric constant of the substrate, respectively. The graphene conductivity has a crucial impact in the dispersion relation and, ultimately, in the relationship between wavelength and frequency of SPP waves in graphennas.

In the case of a free-standing graphene layer ($\varepsilon = 1$), the dispersion relation is simplified to the following expression [108]:

$$n_{\mathrm{eff}}(\omega) = \sqrt{1 - 4\frac{\mu_c}{\varepsilon_0}\frac{1}{\sigma(\omega)^2}} \tag{4.7}$$

where $n_{\mathrm{eff}} = k_{\mathrm{SPP}}/k_0 = \lambda_0/\lambda_{\mathrm{SPP}}$ is known as the effective SPP index, which denotes the relationship between the SPP wavenumber k_{SPP} and the free-space wavenumber k_0 and, equivalently, the ratio between the free-space wavelength λ_0 and the SPP wavelength λ_{SPP}. The effective mode index in graphene is in the order of 10^2 [108], yielding a reduction of the size of resonant graphennas of up to two orders of magnitude with respect to equivalent metallic antennas.

Even though the air-dielectric interface does not support SPP waves, the termination of the graphene patch acts as a mirror and a FP type resonator can be realized when the following condition is satisfied:

$$L = L' + 2\delta L = m\frac{\lambda_{\mathrm{SPP}}}{2} = m\frac{\pi}{k_{\mathrm{SPP}}} \tag{4.8}$$

where L is the effective antenna length, obtained from the physical antenna length L' and the distance of the field penetration outside the antenna δL, and m is an integer.

Solving the dispersion relation (4.6) with the FP condition (4.8) for a given effective antenna length L results in a set of m complex frequencies ω_m (resonator modes). The coupling of the incident radiation with those modes leads to the resonances of the graphenna. Taking into account that the modes of the resonator are orthogonal, they can be modeled as a set of independent driven harmonic oscillators with angular frequencies $\omega_{0m} = \sqrt{(\mathrm{Re}[\omega_m])^2 + (\mathrm{Im}[\omega_m])^2}$, corresponding to the graphenna resonant frequencies, and damping rates $\gamma_m = -2\mathrm{Im}[\omega_m]$, which relate to the attenuation of the SPP waves in the graphenna.

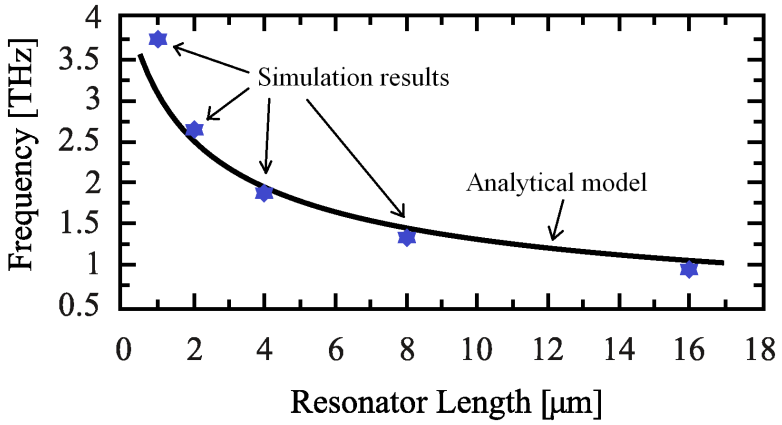

Figure 4.4: Dependence of the first resonance of an infinitely wide graphenna as a function of its length. The solid line is as calculated using the analytical model and the stars correspond to the resonance frequencies obtained by simulation.

Therefore, this model can be used to estimate the spectral position of the resonances in a graphenna. Alternatively, the antenna resonant frequency of graphennas can also be obtained as the frequency at which its absorption cross section is maximized (see Section 4.3). As an example, Figure 4.4 shows the position of the first resonance of a graphenna as a function of its length. The analytical expression is compared with the results of numerical simulations. The antenna is modeled as an infinitely wide graphene patch with a physical length $L' = 5$ μm and the penetration length is set to $\delta L = 0.5$ μm. A plane wave linearly polarized along the patch length and normally incident to the antenna is considered. The simulation results show a very good agreement with the analytical model.

4.2.1 Properties of SPP waves in graphennas

Since the operation of the graphenna is based on the SPP resonances, it is important to analyze the properties of SPP waves in graphennas. Two important performance metrics of plasmonic antennas are the *plasmon compression factor* and the *plasmon propagation length*. The plasmon compression factor K is defined as the quotient between the free-space wavelength and the plasmon wavelength: $K = \lambda_0/\lambda_{\mathrm{SPP}}$ or, equivalently, the quotient between the real part of the SPP wavevector and the free-space wavevector $K = \mathrm{Re}[k_{\mathrm{SPP}}]/k_0$. Moreover,

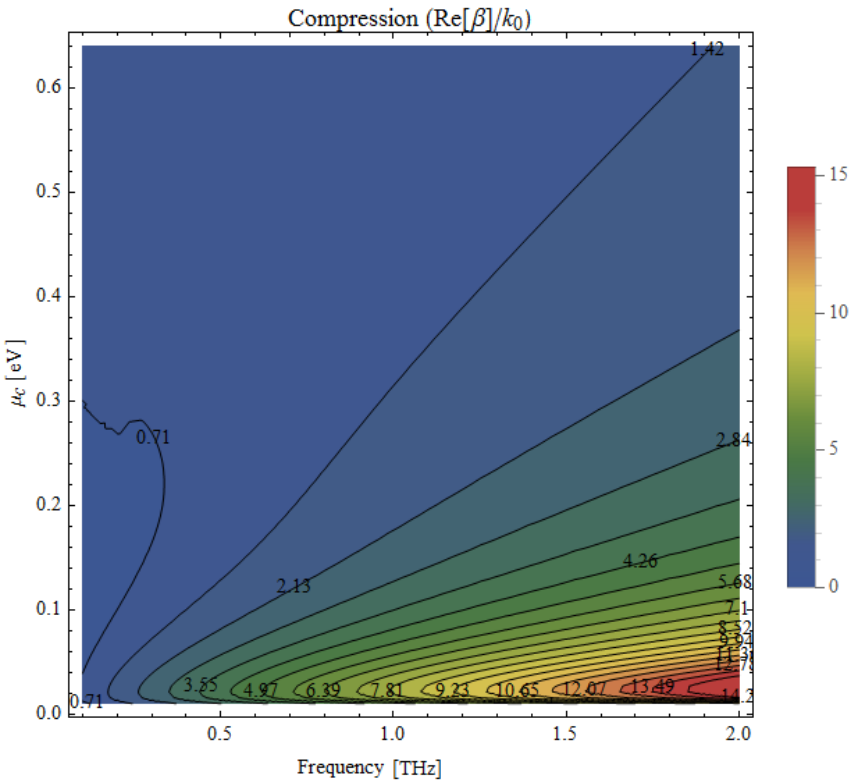

Figure 4.5: Plasmon compression factor in a graphenna as a function of the frequency and chemical potential.

this parameter determines the size difference between a graphenna and a metallic antenna resonating at the same frequency, i.e., $K = L_0/L$, where L_0 is the metallic antenna length and L that of the graphenna. Figure 4.5 shows the plasmon compression factor as a function of the frequency and the chemical potential. A graphene layer with an electron mobility of 10000 cm^2/Vs over a dielectric substrate with dielectric constant $\varepsilon = 4$ are considered. A desired high compression factor is observed for high plasmon frequencies and a low (but non-zero) chemical potential.

The plasmon propagation length L_{SPP} is defined as the distance for the SPP intensity to decay by a factor of $1/e$. L_{SPP} is usually expressed in terms of the plasmon wavelength, yielding the expression $L_{\text{SPP}}/\lambda_{\text{SPP}} = \text{Re}[k_{\text{SPP}}]/4\pi\text{Im}[k_{\text{SPP}}]$. Figure 4.6 shows the plasmon propagation length in units of the corresponding SPP wavelength, with the same parameters as in the previous case. Opposite to

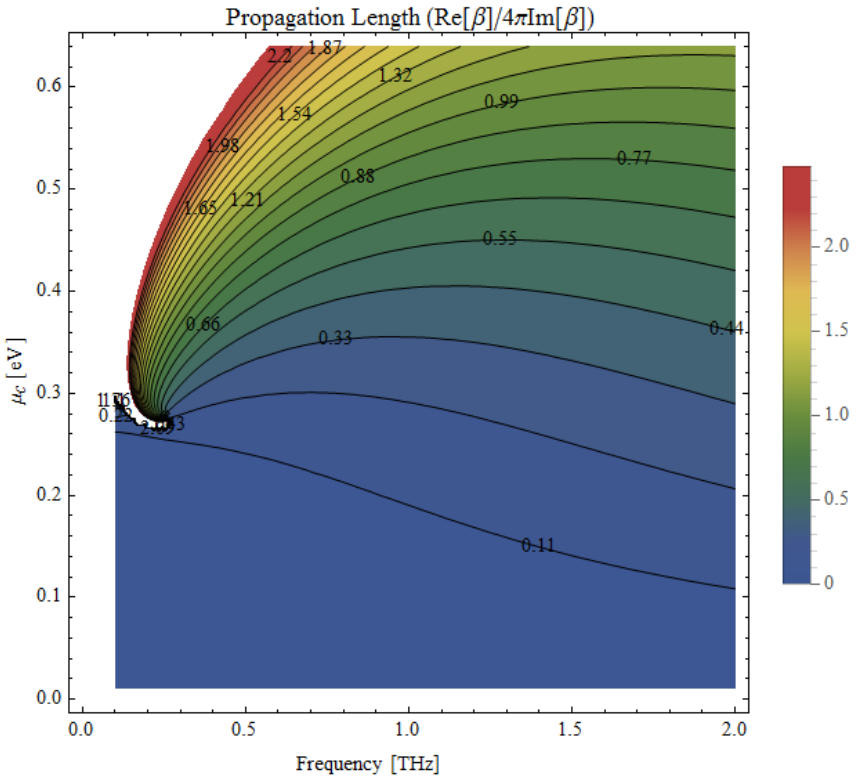

Figure 4.6: Plasmon propagation length in a graphenna as a function of the frequency and chemical potential.

the case of the plasmon compression factor, the plasmon has a longer propagation length (of above one plasmon wavelength) in the low frequency and high chemical potential potential region. Therefore, there exists a trade-off between the plasmon compression factor and its propagation length: graphennas operating at a high frequency and low chemical potential will allow a higher miniaturization with respect to metallic antennas, whereas graphennas working a low frequency and high chemical potential will exhibit lower losses and, in consequence, a higher radiation efficiency.

4.3 Scattering properties of graphennas

In order to study the performance of a graphenna, it is interesting to investigate its scattering, absorption and extinction cross sections. The scattering (absorption)

cross section is defined as a ratio of the scattered (dissipated) power to the incident power, namely

$$\sigma_{sca} = \frac{\oint_S d^2r\, \mathbf{S}_s \cdot \mathbf{n}}{|\mathbf{S}_{inc}|}, \tag{4.9}$$

and

$$\sigma_{abs} = \frac{\oint_S d^2r\, \mathbf{S} \cdot \mathbf{n}}{|\mathbf{S}_{inc}|}. \tag{4.10}$$

where the surface integration is performed over a surface enclosing the graphenna. $\mathbf{n}$ is the surface normal and $\mathbf{S}$, $\mathbf{S}_s$ and $\mathbf{S}_{inc}$ are the Poynting vectors of the total, scattered and incident fields, respectively. The extinction cross section is given by the sum of the scattering and the absorption cross sections:

$$\sigma_{ext} = \sigma_{scat} + \sigma_{abs}. \tag{4.11}$$

The cross sections of a graphenna can be obtained from its complex resonant frequencies ω_m, derived in Section 4.2. Introducing the dipole polarizabilities of the oscillators α_m as

$$\vec{\mu}_m = \frac{f_m}{\omega_{0m}^2 - \omega^2 - \mathrm{i}\gamma_m\omega}\mathbf{E}_{inc} = \alpha_m \mathbf{E}_{inc} \tag{4.12}$$

with f_m being the oscillator strength, the scattering and absorption cross sections of the graphenna can be calculated as a sum of the normalized scattered and dissipated power of N individual oscillators [115], namely

$$\sigma_{sca} = \frac{\omega^4}{6\pi\varepsilon_0^2 c^4}\sum_{m=1}^{N}|\alpha_m|^2 \tag{4.13}$$

and

$$\sigma_{abs} = \frac{\omega}{\varepsilon_0 c}\sum_{m=1}^{N}\mathrm{Im}\alpha_m. \tag{4.14}$$

Figure 4.7 shows the calculated scattering (dashed green line with dots) and absorption (solid blue line with dots) cross sections of a graphenna with an ef-

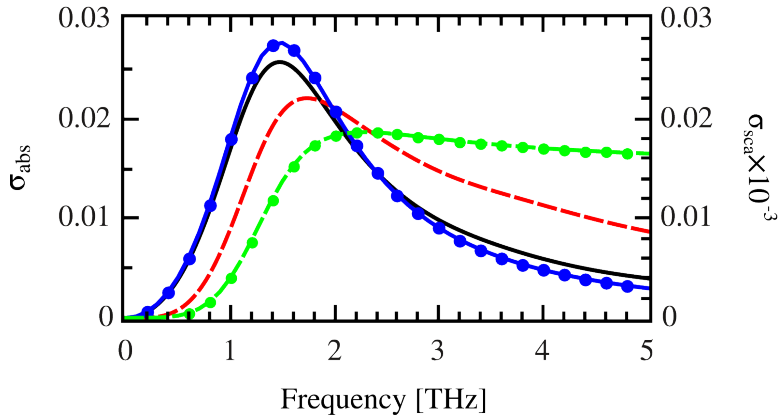

Figure 4.7: Scattering (dashed green line with dots) and absorption (blue line with dots) cross sections of a graphenna on an infinite silicon substrate obtained using the Fabry-Perot model, as compared with the scattering (dashed red line) and absorption (black line) cross sections obtained using numerical simulations.

fective length $L = 1$ µm and width $W = 100$ µm normalized to its geometrical area. The graphenna is supported by an infinite silicon substrate with dielectric constant $\varepsilon = 11.9$. Room temperature ($T = 300$ K) and zero electrostatic bias ($\mu_c = 0$ eV) are assumed.

The results obtained with the analytical model are compared with the scattering (dashed red line) and absorption (solid black line) cross sections calculated by numerical simulation. The effective length of the antenna is set to $L = 1.36$ µm, where the penetration length $\delta L = 0.18$ µm has been estimated empirically. With the oscillator strength f_m used as a fit parameter, a reasonable agreement with the numerical results can be achieved even if only the first mode of the resonator ($f_1 = 0.073$) is taken into account.

The results show that the interaction of the terahertz radiation with the graphenna is dominated by the absorption, with the scattering being three orders of magnitude weaker due to the large wavelength mismatch between the electromagnetic excitation in the graphene layer and in the far field. The total extinction cross section is equal to a few percents of the graphenna area and demonstrates a clear resonant character. The obtained absorption cross sections are consistent with experimental results reported for graphene micro-ribbon arrays [96].

4.4 Resonance tuning of graphennas

One of the main advantages of graphennas is the wide tunability of their resonant behavior. Indeed, the radiation properties of graphennas can be easily controlled by adjusting the graphenna design parameters. Next follows an analysis of how key characteristics of graphennas, such as the resonant frequency, depend on several design parameters. These parameters include the dimensions of the graphene patch and the dielectric substrate supporting it, the chemical potential applied to graphene and its relaxation time. The obtained results allow the derivation of guidelines for the design of future graphennas.

4.4.1 Dimensions of the graphene patch

The dependence of the resonant frequency on the graphenna length is shown in Figure 4.8 for different graphenna widths. The graphenna is modeled as a graphene patch on infinite silicon substrate at room temperature and zero electrostatic bias. For a given length, graphennas with a smaller width possess resonances at lower frequencies. This effect might be attributed to the higher confinement of surface plasmons in a narrow graphene patch, which in turn leads to higher effective permittivity and lower resonance frequency. At the same time, the resonance shifts towards higher frequencies for shorter graphennas, in full agreement with the resonance condition (4.8).

These results suggest that, by adjusting the dimensions of the graphenna (in particular its length), its radiation frequency can be tuned in a wide spectral range.

4.4.2 Dielectric substrate

The influence of the dielectric substrate on the resonant frequency of graphennas is considered next. The dielectric constant and thickness of the substrate are found to influence both the spectral position and magnitude of the resonance. In Figure 4.9 (top), the extinction cross section of the graphenna with length $L = 1$ µm and width $W = 0.5$ µm supported by different infinite substrates is shown: silicon (ε=11.9), silica (ε=4.0) and vacuum (ε=1). As expected from

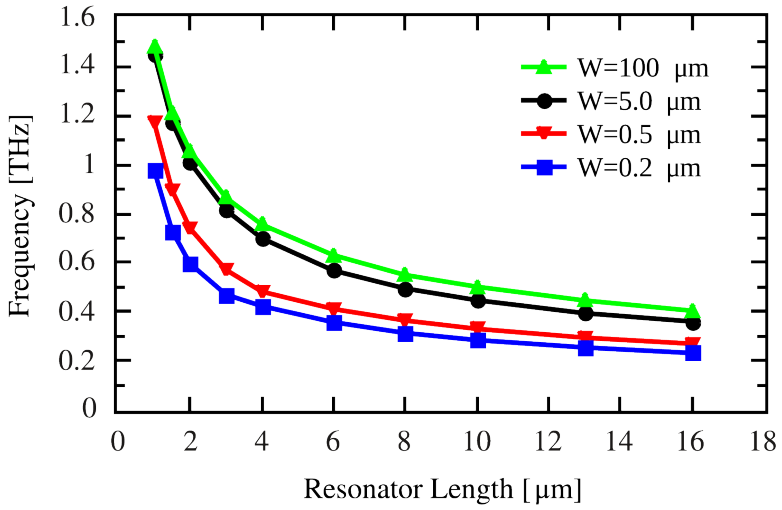

Figure 4.8: Dependence of the first resonant frequency of the graphenna on its length, for different widths: $W = 100$ µm, $W = 5$ µm, $W = 0.5$ µm and $W = 0.2$ µm.

the SPP dispersion relation (4.6), an increase of the dielectric constant of the substrate shifts the resonance towards lower frequencies, while simultaneously reducing the extinction efficiency. For a silicon substrate, a fourfold reduction of the total extinction cross section, and in consequence of the antenna efficiency, can be observed in comparison to the antenna suspended in air.

This reduction can be partially compensated by adjusting the substrate thickness. In Figure 4.9 (bottom), the extinction cross section is shown for the graphenna on silicon substrate with different thicknesses. Due to constructive interference in the substrate, the extinction cross section can restore its value corresponding to the free-standing graphenna, while the resonant frequency remains almost constant. In particular, if the resonance of the substrate coincides with the antenna resonance ($D = 37.5$ µm), a fivefold enhancement of the extinction cross section can be achieved.

In a more realistic graphenna model, the graphene patch is deposited over a finite substrate. Using this model, the dependence of the antenna extinction cross section on the substrate size is evaluated next. The antenna is made of a graphene patch with a size of 5x0.5 µm located on the center of a silicon substrate with a square shape and a thickness of 1 µm. Figure 4.10 shows the extinction cross

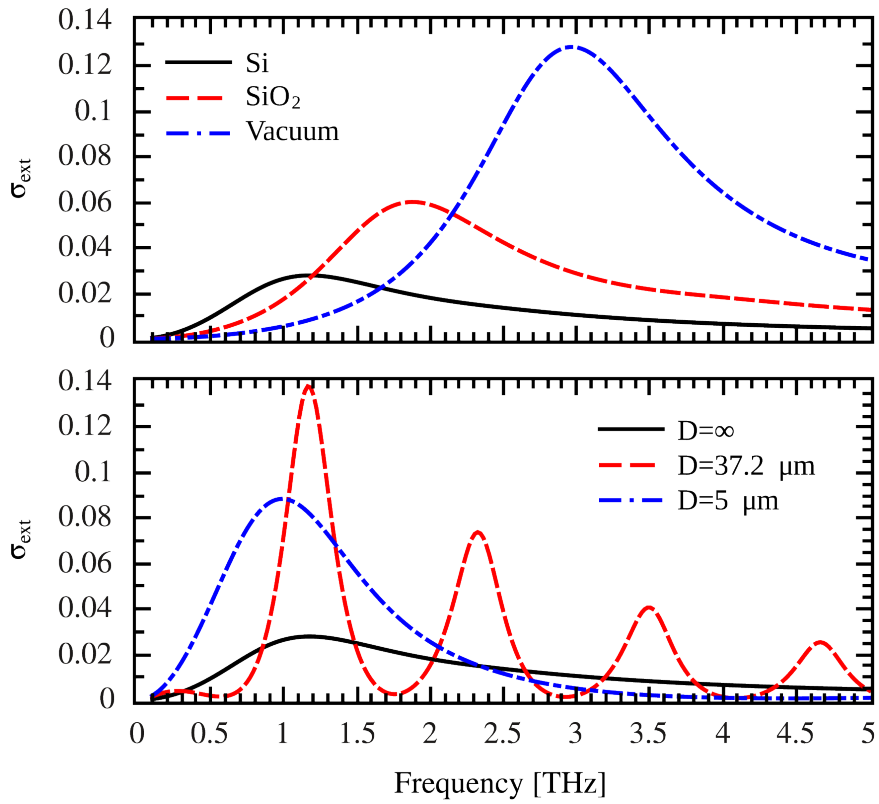

Figure 4.9: Top: Normalized extinction cross section of the graphenna placed on different substrates, silicon (ε=11.9), silica (ε=4.0) and vacuum (left to right). Bottom: Normalized extinction cross section for different thickness of silicon substrates, $D = \infty$ (solid), $D = 37.5$ µm (dashed) and $D = 5$ µm (dashed-dotted).

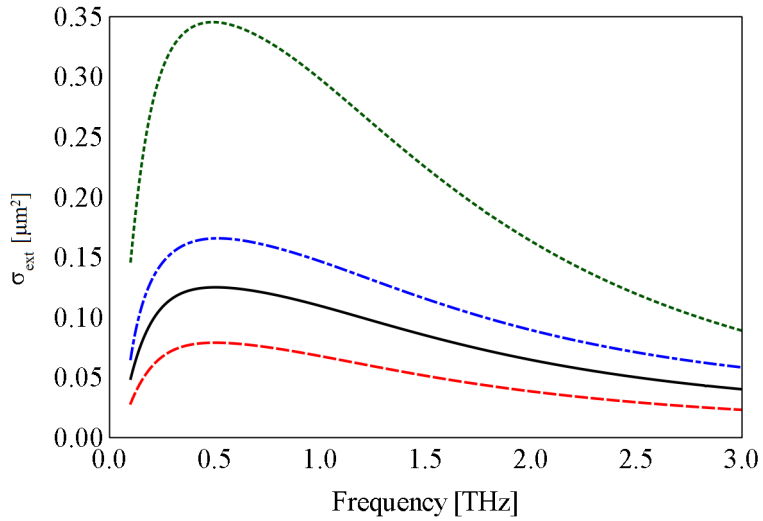

Figure 4.10: Extinction cross section of a graphenna for different substrate sizes: 6x6 µm, 10x10 µm, 16x16 µm and infinite (below to above).

section of this graphenna for different substrate sizes, from 6x6 µm to infinity. On the one hand, it can be seen that a larger substrate improves the antenna performance, since the extinction cross section increases with the substrate size, up to a certain limit. On the other hand, the antenna resonant frequency is shown to remain almost constant at 0.5 THz, independently of the substrate size.

Another interesting aspect to evaluate is the influence of the position of the graphene patch relative to the substrate in a graphenna. The considered substrate has dimensions of 6x6 µm and a thickness of 1 µm. The graphene patch measures 5x0.5 µm and is located in three different positions, as shown in Figure 4.11: in the center of the substrate (4.11a), at 1.25 µm from the center (4.11b) and at 2.5 µm from the center (4.11c). Figure 4.12 shows the antenna extinction cross section as a function of frequency, for each of these three configurations. As it can be observed, the extinction cross section increases as the graphene patch is located closer to the side of the substrate. Moreover, the resonant frequency becomes slightly higher when the patch is farther from the center.

These results indicate that, on the one hand, as the dielectric substrate becomes larger, the power absorbed by the graphenna increases up to a certain extent. On the other hand, for a given substrate size, the optimal location for on-

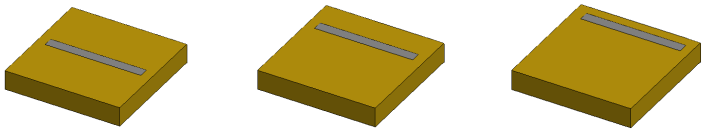

(a) (b) (c)

Figure 4.11: Different positions of the graphene patch with respect to the substrate: patch in the center of the substrate (a), at 1.25 µm from the center (b) and at 2.5 µm from the center (c).

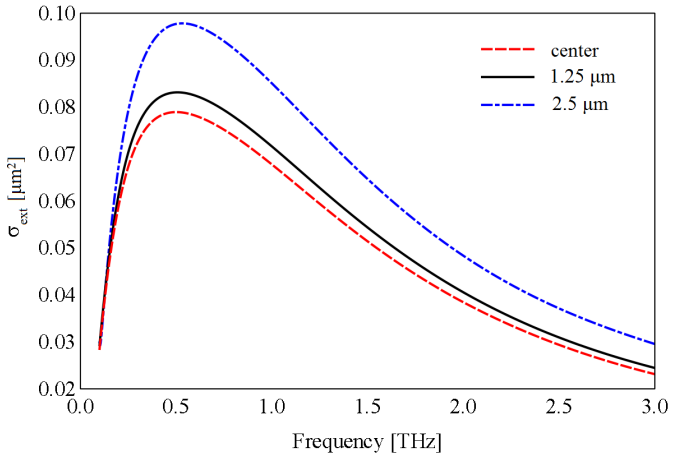

Figure 4.12: Extinction cross section of a graphenna, for different positions of the graphene patch: in the center of the substrate (blue solid line), at 1.25 µm from the center (green dashed line) and at 2.5 µm from the center (red dotted line).

chip graphennas may be near the edge of the substrate. Moreover, the width of the dielectric substrate can be optimized in order to achieve a maximum radiation efficiency.

4.4.3 Graphene chemical potential

Another parameter of great interest to evaluate the performance of the graphenna is the chemical potential of the graphene patch, i.e., the level in the distribution of electron energies at which a quantum state is equally likely to be occupied or empty.

The results obtained so far have assumed a model of graphene with zero chemical potential. However, as shown in equation (4.1), varying the chemical potential of graphene will affect the electrical conductivity of the graphenna, which is one of the main factors that determine its radiation performance. The chemical potential of graphene can be easily controlled by means of doping and/or by applying an electrostatic bias voltage, thereby allowing to dynamically tune the radiation properties of graphennas. The influence of the chemical potential of graphene on the resonant frequency of graphennas is examined next.

Figure 4.13 shows the real and imaginary parts of the frequency-dependent graphene conductivity, calculated for different chemical potentials. A realistic range of values for the chemical potential, from 0 to 2 eV, has been chosen based on existing results in the literature [165, 166]. It can be observed that the conductivity of graphene can be indeed controlled by changing the chemical potential; in particular, increasing the chemical potential results in higher values of both the real and imaginary parts of the conductivity.

The strong dependence of the graphene conductivity on the chemical potential opens the possibility to tune the resonant frequency of the graphenna. Figure 4.14 shows the absorption cross section of a graphenna with length 5 µm and width 0.5 µm as a function of frequency, calculated by numerical simulation. The graphene conductivity models shown in Figure 4.13, obtained varying the chemical potential from 0 to 2 eV, were considered. Moreover, the absorption cross section of a metallic antenna, modeled as a gold antenna with the same size as the graphenna and a thickness of 20 nm, is shown with a dashed gray line.

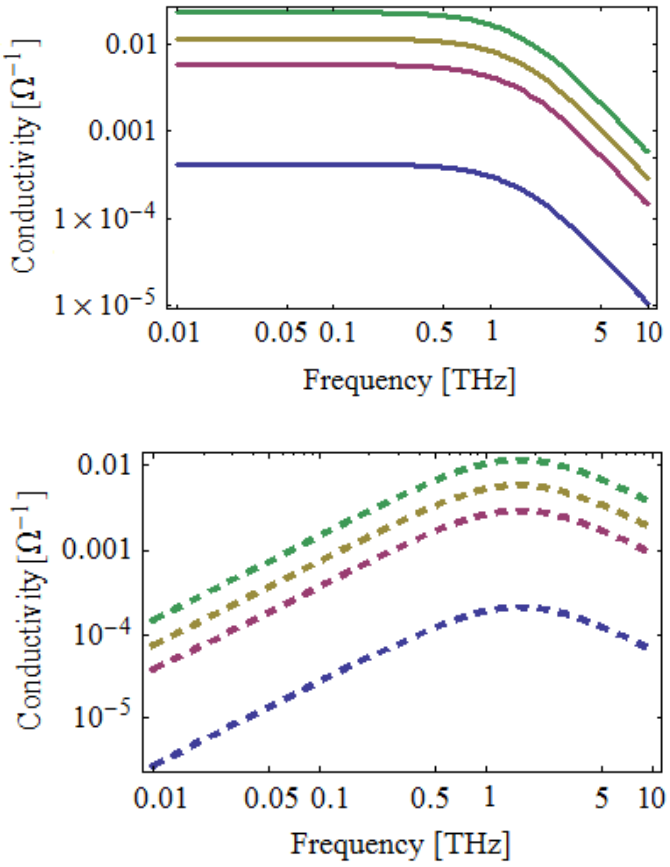

Figure 4.13: Log-log plots of the real (above) and imaginary (below) parts of the graphene conductivity as a function of the frequency, for different values of the chemical potential: 0 eV (blue line), 0.5 eV (purple line), 1 eV (yellow line) and 2 eV (green line).

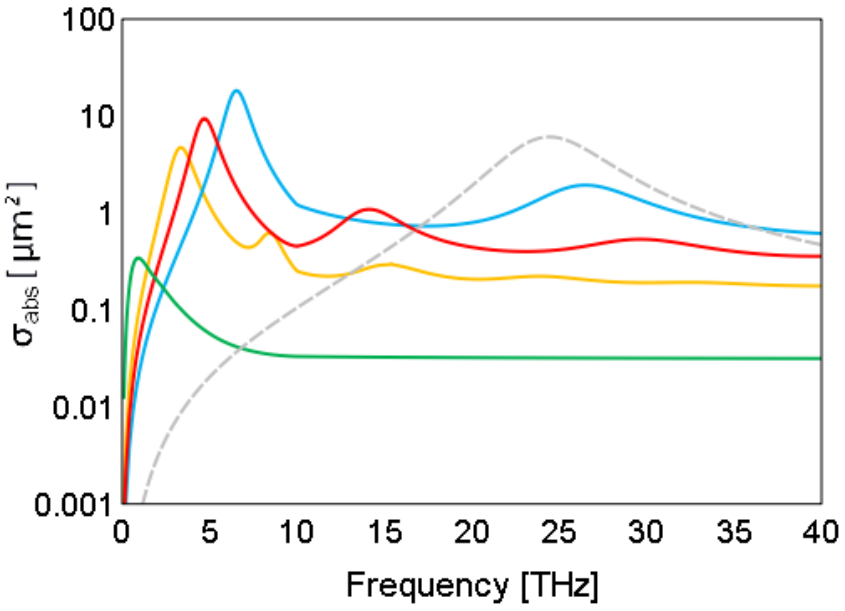

Figure 4.14: Absorption cross section (in logarithmic scale) of a graphenna as a function of frequency, for different values of the chemical potential: 0 (green line), 0.5 (yellow line), 1 (red line) and 2 eV (blue line). The results are compared to that of an equivalent gold antenna with the same size (gray dashed line).

Chemical potential	Resonant frequency
0 eV	0.918 THz
0.5 eV	3.356 THz
1 eV	4.704 THz
2 eV	6.541 THz

Table 4.1: Resonant frequency of a graphenna with length 5 µm and width 0.5 µm as a function of the chemical potential.

As it can be observed, the maximum absorption cross section increases by a factor of 50 as the chemical potential changes from 0 to 2 eV. Furthermore, as shown in Table 4.1, the resonant frequency of the graphenna also increases dramatically with the chemical potential applied to the graphene layer. However, in any case, the resonant frequencies of graphennas remain well below that of a metallic antenna with the same size, around 25 THz.

In summary, in terms of chemical potential, there is a trade-off between the amount of power that a graphenna can absorb and its resonant frequency. On the one hand, graphennas with zero chemical potential resonate at a low frequency but with a small absorption cross section, which will limit their achievable radiation efficiency. On the other hand, graphennas with a higher chemical potential posses greater absorption capabilities, but their resonant frequency also increases, which will reduce their potential transmission range. A compromise between these two magnitudes will therefore need to be reached by designers of future graphennas to implement wireless communications among nanosystems.

4.4.4 Temperature

The dependence of the graphenna resonances with respect to the temperature is found to be small. As shown in Figure 4.15, graphennas possess a high temperature stability. For instance, for a structure made of a graphene patch with dimensions 1x0.5 µm over a semi-infinite dielectric substrate with dielectric constant ε=11.9, a 100 K temperature variation results in a resonant frequency shift of only 0.15 THz. A zero chemical potential ($\mu_c = 0$ eV) is considered.

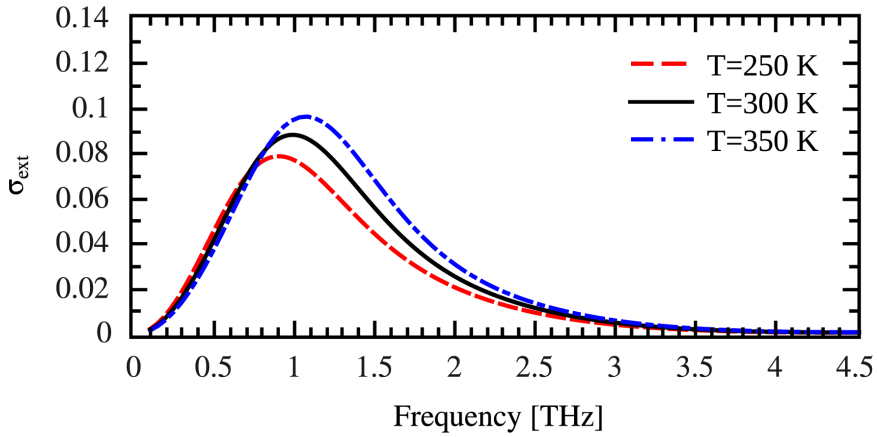

Figure 4.15: Dependence of the graphenna resonant frequency on the temperature.

4.4.5 Relaxation time

The relaxation time of a material is the time that it takes for a charge distortion as fluctuation to relax to a uniform charge density after it has been introduced in the material. The relaxation time in graphene depends, amongst others, on the quality of the graphene sample and it is a fundamental parameter of its conductivity model (4.1). Several authors consider different values for the relaxation time of graphene, ranging from 10^{-14} s to 10^{-11} s [167, 168, 169, 170]. Since there does not seem to exist a common agreement for the value of the relaxation time in graphene, its influence on the radiation properties of graphennas is considered next.

Figure 4.16 shows the real and imaginary parts of the frequency-dependent graphene conductivity, for different relaxation times based on values found in the literature [167, 168, 169, 170]. The relaxation time is seen to possess a strong influence on the graphene conductivity, whose value changes up to 3 orders of magnitude depending on the relaxation time.

The absorption cross section of graphennas is shown in Figure 4.17 for different relaxation times. Interestingly, the chosen value for the relaxation time τ has a huge impact on the resonant character of the graphenna and its bandwidth. In particular, for $\tau = 10^{-14}$ s, the graphenna does not resonate in the terahertz band. When $\tau = 10^{-13}$ s, a wide resonance around 1 THz is observed, with

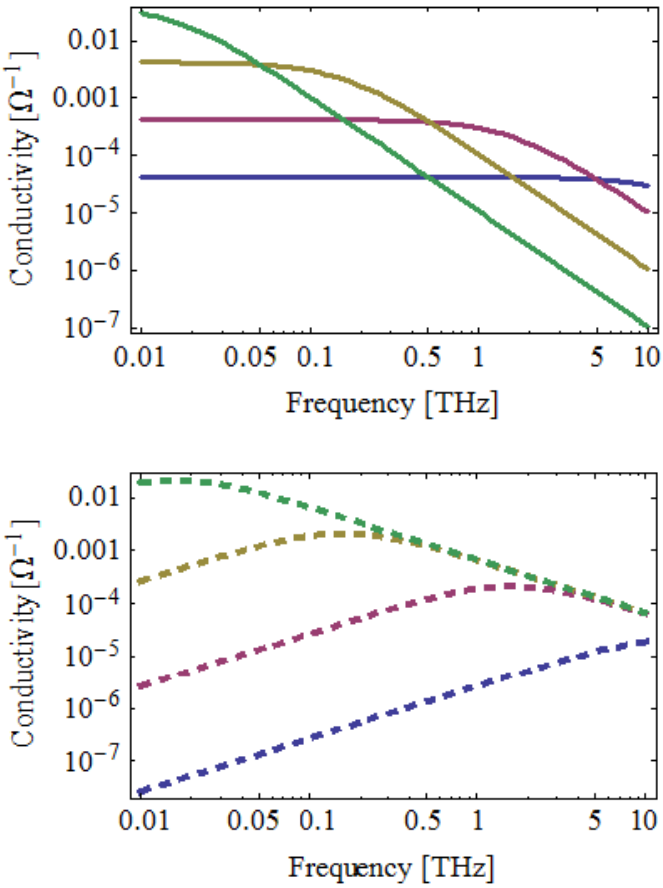

Figure 4.16: Log-log plots of the real (above) and imaginary (below) parts of the graphene conductivity as a function of the frequency, for different values of the relaxation time: 10^{-14} s (blue line), 10^{-13} s (purple line), 10^{-12} s (yellow line) and 10^{-11} s (green line).

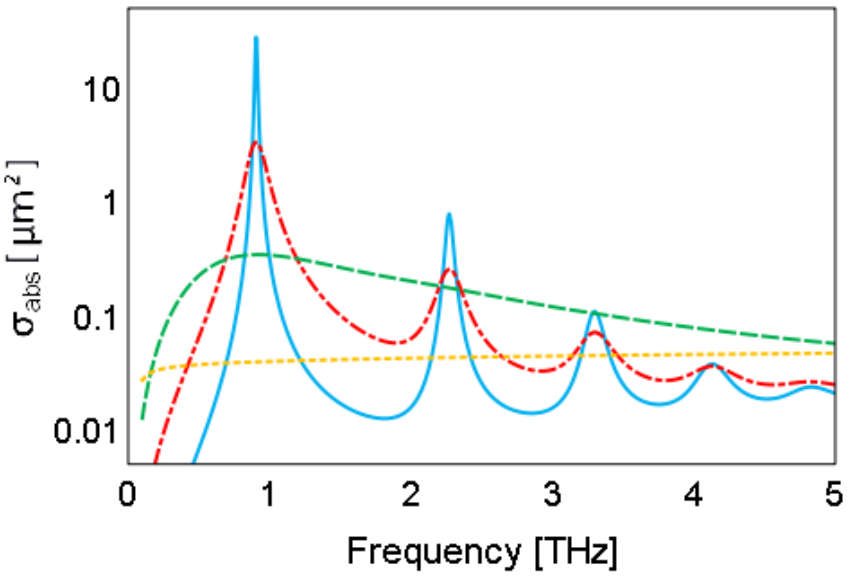

Figure 4.17: Absorption cross section (in logarithmic scale) of a graphenna as a function of frequency, for different values of the relaxation time: 10^{-14} s (yellow dotted line), 10^{-13} s (green dashed line), 10^{-12} s (red dot-dashed line) and 10^{-11} s (blue solid line).

a -3 dB bandwidth of 1.9 THz. As the relaxation time continues to increase, higher-order resonances appear and a more intense resonant behavior is observed. Furthermore, the -3 dB bandwidth diminishes dramatically, to 0.16 THz in the case of $\tau = 10^{-12}$ s, and to 0.019 THz for $\tau = 10^{-11}$ s.

Given that the main application envisaged for graphennas consists of wireless communications among nanosystems, a bandwidth as large as possible is desired in order to maximize the channel capacity. In conclusion, the optimal value of the relaxation time for graphennas is around $\tau = 10^{-13}$ s, in order to achieve a resonant behavior while maintaining a radiation bandwidth as large as possible.

4.5 Comparison with metallic antennas

In order to quantify the advantages of graphennas with respect to metallic miniaturized antennas, it is of particular interest to compare their radiation properties. In particular, two particularly relevant properties of graphennas and metallic an-

tennas, namely, their radiation diagram and resonant frequency, are compared next.

4.5.1 Radiation diagram

The radiation diagram of graphennas is studied next [148]. With this purpose, a terahertz signal is driven into the antenna, modeled as a freestanding graphene patch, by means of a pin feed. A simulation study of the transmitting graphenna is performed, which allows obtaining its radiation pattern. The antenna has a fixed length $L = 5$ µm, while its width takes the values $W = 1$, 2 and 5 µm (the geometry for the case $W = 1$ µm is shown in Figure 4.18). The pin feed is located at a distance of 0.1 µm from one of the shorter edges of the antenna. Figure 4.19a shows the radiation pattern of a graphenna with the described properties, in the plane parallel to the graphene patch.

Figure 4.19b shows the radiation pattern of an equivalent metallic antenna, modeled as a perfect electric conductor patch of the same dimensions. The radiation pattern is computed at a frequency of 1.3 THz, which approximately corresponds to the resonant frequency of a graphenna of the previous dimensions. Even though the metallic antenna is expected to resonate at a higher frequency band, the analysis is performed at the same frequency for the sake of comparison. As it can be seen, in both cases the radiation pattern is similar to that of a half-wave dipole antenna, and the differences between the patterns of graphene and the metallic antennas are minimal.

In conclusion, as it could be expected, future graphennas will not differ significantly with respect to equivalent metallic antennas in terms of their radiation pattern.

4.5.2 Resonant frequency

Next, the resonant frequency of metallic and graphene antennas is compared. In particular, the focus is set on the scalability of the antenna resonant frequency with respect to its length [171].

In order to study the resonant frequency of metallic miniaturized antennas, a patch antenna consisting of a free-standing gold slab placed on an air-dielectric

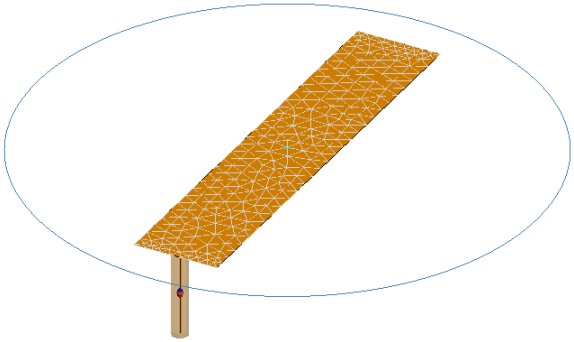

Figure 4.18: Schematic diagram of the graphenna in transmission. The antenna is composed of a graphene patch with a length $L = 5$ µm and a width $W = 1$ µm, and a pin feed located at 0.1 µm from the antenna edge. The blue circle shows the plane in which the radiation diagram is measured.

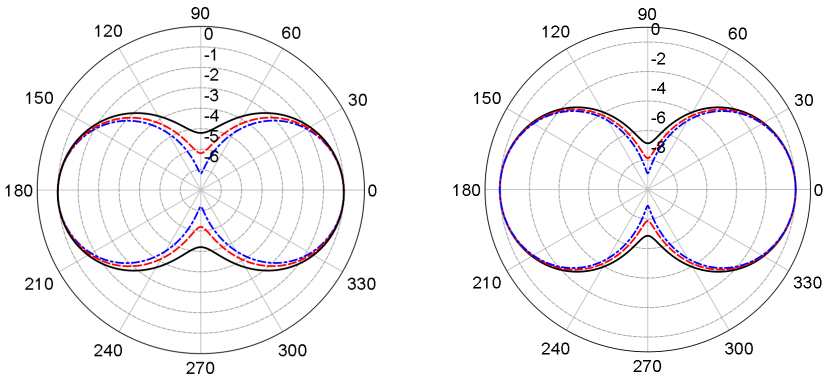

(a) Graphenna (b) Metallic antenna

Figure 4.19: Radiation pattern of graphene (a) and metallic (b) antennas as a function of their width. The plots show the normalized gain in dB, in the plane parallel to the antenna patch, for an antenna with a length $L = 5$ µm. The results correspond to antenna widths of $W = 1$ µm (blue solid line), 2 µm (green dashed line) and 5 µm (red dotted line).

interface is considered, a structure commonly used for plasmonic nano-antennas in the optical range. The resonant frequency of this antenna can be found by analyzing its dispersion relation, given by the following expression [172]:

$$\tan\left(\Delta\sqrt{1-b}\right) = \frac{\frac{n_g^2}{n_s^2}\sqrt{\frac{b}{1-b}} + n_g^2\sqrt{\frac{b+a}{1-b}}}{1-\frac{n_s^2}{n_g^4}\frac{\sqrt{b(b+a)}}{1-b}} \tag{4.15}$$

where Δ stands for the thickness of the gold slab, n_g is the refractive index of gold, n_s that of the substrate, $a = (n_s^2 - 1)/(n_g^2 - n_s^2)$ is defined as the asymmetry measure and $b = (k_{\mathrm{SPP}}^2/k_0^2 - n_s^2)/(n_g^2 - n_s^2)$ is the normalized mode index.

The resonant frequencies of both antennas can then be obtained by combining the respective dispersion relations (4.6) and (4.15) with the resonance condition (4.8). Furthermore, they can also be calculated by numerical simulation [163], measuring the frequency at which the numerically calculated absorption cross section of the antenna is maximized.

After solving the dispersion relations of graphennas and metallic antennas, their resonant frequencies are found to show a very different behavior in the frequency range of interest. Figure 4.20 compares the resonant frequency of graphene and metallic antennas as a function of their length. The antennas are modeled as simple free-standing rectangular patches without dielectric substrate; in the case of metallic (gold) antennas, a thickness of $\Delta = 20$ nm is assumed, in agreement with experimental works [113]. The blue line shows the first resonant frequency of a graphenna, as obtained from equation (4.6), while the yellow line corresponds to the resonance of a metallic antenna, calculated by means of its respective dispersion relation (4.15).

These results indicate that, in the terahertz range, not only the resonant frequency of a graphenna is more than one order of magnitude lower than that of a metallic antenna with the same size, but also the scalability of the antenna resonant frequency as a function of its length is very different. It can be found by curve fitting that the resonant frequency of a metallic antenna f_{Rm} is inversely proportional to its length in the considered frequency range. In a graphenna, however, a different trend is observed; its resonant frequency f_{Rg} scales inversely

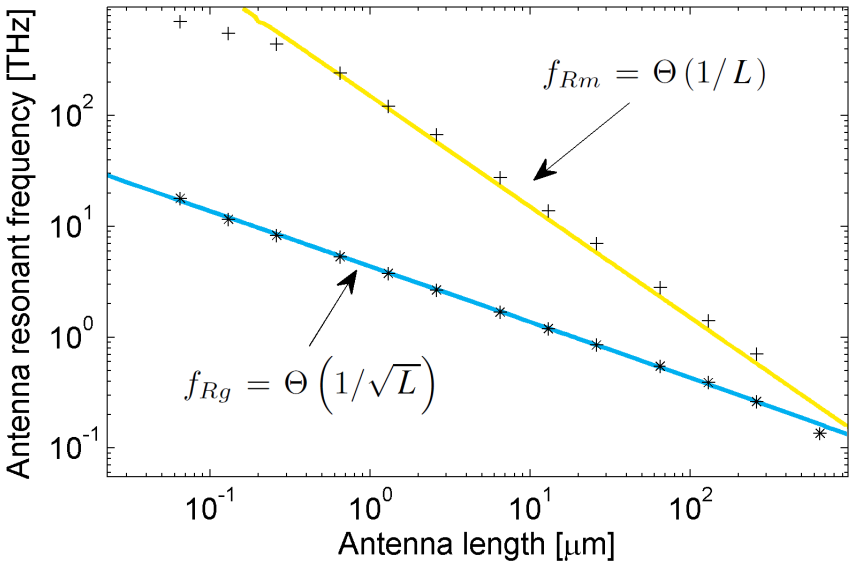

Figure 4.20: Scalability of the resonant frequency of graphene (blue line) and metallic (yellow line) antennas as a function of their length. The simulation results for graphene (stars) and metallic (crosses) antennas are also shown.

proportional to the square root of the antenna length:

$$f_{Rm} = \Theta(1/L) \qquad f_{Rg} = \Theta\left(\frac{1}{\sqrt{L}}\right). \tag{4.16}$$

Interestingly, the scalability of the resonant frequency seen in graphennas is also different from the behavior observed in plasmonic nano-antennas made of noble metals and operating in the optical domain, whose resonant frequency is inversely proportional to the antenna length [173, 114, 112]. Their unique scalability trend turns out to be one of the strongest factors that motivate the use of graphennas to implement wireless communications among nanosystems. Indeed, as the graphenna size is reduced, its resonant frequency increases at a slower pace as compared to a metallic antenna. For instance, as shown in Figure 4.20, metallic antennas with a length of 1 μm resonate at a frequency of 150 THz, in the short-wavelength infrared range. By comparison, a graphenna with the same size would have a resonant frequency of only 3.8 THz, almost two orders of magnitude below the resonant frequency of a metallic antenna. In short, this study confirms that graphennas of micrometric size will be able to

radiate electromagnetic waves in the terahertz band, at a much lower frequency and therefore with a higher transmission range than equivalent metallic antennas.

Moreover, the obtained dependences for the resonances of graphene and gold antennas have been validated by numerical simulation. A graphenna is modeled as a free-standing graphene patch with an infinite width, whereas a metallic antenna is modeled as a free-standing thin gold slab with an infinite width and a thickness of 20 nm. Similar to the case of graphene, the conductivity of gold was obtained with a Drude model.

In Figure 4.20, the crosses show the simulation results of the resonant frequency of graphennas with a length ranging from 50 nm to 1 mm. The penetration length δL has been estimated as a 15% of the antenna length, based on the numerical simulations. The same results for metallic antennas are shown as stars. As it can be observed, in both cases the simulation results show a very good agreement with the resonant frequencies obtained by solving the respective dispersion relations. Moreover, the simulations allow measuring the evolution of the antenna resonant frequency in the regions where the numerical results diverge from the scalability trends observed by solving the dispersion relation. In particular, as it can be seen in Figure 4.20, the scalability of the resonant frequency of graphennas with a length larger than 100 µm does no longer scale as $f_{Rg} = \Theta\left(1/\sqrt{L}\right)$, but it tends to converge with the behavior observed in metallic antennas. Moreover, for metallic antennas with a length smaller than 0.2 µm, as the resonant frequency reaches the threshold at which SPP waves start appearing in gold, its value starts diverging from the scalability trend $f_{Rm} = \Theta\left(1/L\right)$ observed for lower frequencies.

Graphennas have been also modeled with a tight-binding model and their resonant frequency has been found to scale similarly with respect to the antenna dimensions [91], which validates the trend observed from the analysis of the plasmonic effects in graphennas.

4.6 Photoconductive graphennas in radiation

At the time of this writing, graphennas have not been experimentally demonstrated. One of the main challenges in the manufacture of a graphenna is that,

because of its typical resonant frequency in the terahertz band, the antenna must be fed with a suitable terahertz source that can contact it with a reasonable efficiency. Significant research efforts have been devoted to push the limit of RF sources to higher frequencies, as well as to manufacture optical sources with longer emission wavelengths. Following the RF approach, resonance tunneling diodes [174, 175] and chains of frequency multipliers [176] provide compact terahertz sources, but they still show a poor efficiency and limited bandwidth. In the optical domain, quantum-cascade lasers have shown a significant progress, extending their operational frequency to 1 THz at room temperature [177] and to higher frequencies at cryogenic temperatures [178]. Additionally, optical down-conversion of ultrashort laser pulses by means of photoconductor materials has demonstrated a sustained increase in performance in the last decades [179, 180]. In this approach, an ultrashort laser pulse illuminates the surface of a photoconductor generating photocarriers, which move under the influence of an external electrical bias field. The resulting photocurrent forms a picosecond pulse which, with the help of an antenna attached to the photoconductor converts into free-space terahertz radiation.

Among the different approaches for terahertz sources, optical down-conversion is one of the best suited for graphennas, for two main reasons. First, such terahertz sources have typically a very high impedance, in the order of several kΩ, which lies in the same order of magnitude of the input impedance of graphennas [93], thereby improving the impedance matching between both devices. Second, ultrafast photoconductive antennas operate in pulsed mode, which is also the proposed fundamental mechanism for EM communications among nanosystems [181]. In what follows, a graphenna fed with a photoconductive source is designed and its radiated terahertz power is estimated by means of full-wave EM simulations [182]. The findings show that the terahertz signal radiated by the proposed device has a power in the µW range, i.e., in the same order of magnitude as traditional photoconductive antennas. These results validate the proposed approach and paves the way towards the experimental fabrication of graphennas.

Next, the proposed device is described and the photoconductive source is modeled. Using this model together with the graphenna model introduced in

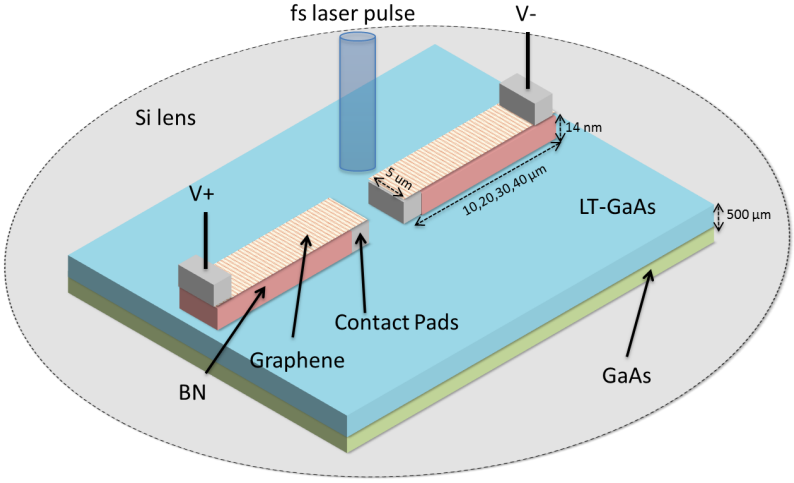

Figure 4.21: Schematic representation of a graphenna fed with a photoconductive material.

Section 4.2, and by means of full-wave EM solvers, the radiated terahertz power by a photoconductive graphenna is estimated as a function of material, illumination and antenna geometry parameters.

4.6.1 Device description

Figure 4.21 depicts a schematic representation of the proposed dipole graphenna fed with a photoconductor. When a femtosecond laser pulse excites the biased semiconductor –low-temperature-grown gallium arsenide (LT-GaAs) [183]– with a photon energy greater than its bandgap, electrons and holes are produced at the illumination point in the conduction and valence bands, respectively. The rapid changes of the density of the photocarriers and their acceleration to the applied DC bias produce a picosecond voltage pulse.

This picosecond pulse excites SPP waves at the interface between the graphene layer and the dielectric material. This SPP wave propagates along the graphenna producing a free-space terahertz radiation. As shown in Figure 4.21, the dielectric material is boron nitride (h-BN) in order to achieve a high electron mobility [184]. A high electron mobility is an important requirement for graphennas, given its strong dependence with the antenna efficiency, as further discussed in the results section. Finally, the silicon lens is a common technique used to improve the

directivity of the radiated signal [185].

4.6.2 Photoconductor model

This section presents a model of the time-dependent voltage generated by a photoconductive source, based on a Drude-Lorentz model [179]. The trapping time τ_c of the photocarriers in LT-GaAs is shorter than the recombination time of electrons and holes. Then, the charge density $n(t)$ can be obtained as

$$\frac{dn(t)}{dt} = -\frac{n(t)}{\tau_c} + G(t) \tag{4.17}$$

where $G(t)$ is the generation rate of the carriers as a result of the laser pulse. The excitation time of the laser pulse is typically in the order of tens of femtoseconds. The velocity of the carriers $v(t)$ can be expressed as

$$\frac{dv(t)}{dt} = -\frac{v(t)}{\tau_s} + \frac{e}{m}E_{loc} \tag{4.18}$$

where τ_s is the momentum relaxation time and E_{loc} is the local electric field, which can be expressed as $E_{loc} = E_{bias} - P_{sc}(t)/\eta\epsilon$, where E_{bias} is the applied bias field, ϵ is the permittivity of the semiconductor material and η is a geometric factor. Finally, the polarization $P_{sc}(t)$ caused by the separation of the electron and hole has the following expression:

$$\frac{dP_{sc}(t)}{dt} = -\frac{P_{sc}(t)}{\tau_r} + j(t) \tag{4.19}$$

where τ_r is the recombination time of electrons and holes and $j(t)$ is the generated photocurrent density.

Based on this fundamental principles and under the assumption that the momentum relaxation time τ_s is small, *Khiabani et al.* [186] developed an equivalent circuit model using lumped elements that provides accurate estimates of the power radiated by photoconductive antennas –in agreement with published experimental data– taking into account the underlying physical behavior. With this model, the time-dependent voltage at the antenna terminals V can be expressed as:

$$V(t) = Z_a \cdot j(t)\beta \cdot V_c(t) \tag{4.20}$$

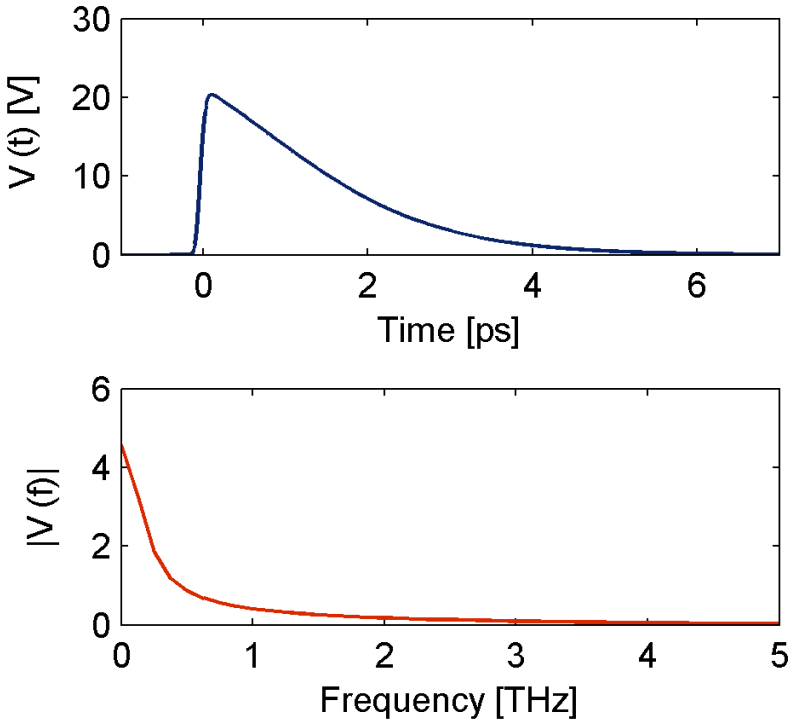

Figure 4.22: Generated voltage by the photoconductive source, in the time domain (above) and frequency domain (below).

where Z_a is the antenna input impedance (assumed independent of the frequency), V_c is the voltage at the antenna gap (derived from its equivalent circuit [186]) and β is the active area in the semiconductor through which the photocurrent flows.

Figure 4.22, calculated with the equation of the pulse voltage 4.20, shows the generated voltage both in the time and frequency domain. This pulse-shaped signal excites SPP waves at the graphenna which result in free-space radiation. The main parameters of the photoconductive antenna are shown in Table 4.2, which have been taken assuming realistic values from the literature [186].

4.6.3 Results

Some results of the radiated power by the photoconductive graphenna, as a function of several parameters from both the antenna and the photoconductive source,

Parameter	Symbol	Value
Electron mobility for LT-GaAs	μ_{GaAs}	200 $\text{cm}^2\text{V}^{-1}\text{s}^{-1}$
Average optical power	P_{av}	2 mW
Laser frequency	ν_{opt}	375 THz
Laser repetition rate	f_{rep}	80 MHz
Laser pulse duration	τ_l	100 fs
Carrier lifetime	τ_c	1 ps
Carrier recombination time	τ_r	100 ps
Bias voltage	V_{bias}	30 V
Antenna gap length	L	10 µm
Antenna gap width	W	10 µm
Antenna impedance	Z_a	10 kΩ

Table 4.2: Main parameters of the photoconductive antenna.

as shown next. The power of the terahertz pulse generated by the photoconductive source is obtained as $P = V^2/Z_a$, where V is calculated by solving the model previously presented in Section 4.6.2. Then, the power radiated by the graphenna is obtained by taking into account the two main impairments introduced by the graphenna. First, the impedance mismatch loss between the photoconductive source and the graphenna: $M_L = 1 - \rho^2$, where ρ is the reflection coefficient $\rho = (Z_a - Z_s)/(Z_a + Z_s)$. Second, the antenna radiation efficiency ε_R, calculated numerically by simulation [163]. The power radiated by the antenna P_{rad} is then obtained as

$$P_{rad} = M_L \cdot \varepsilon_R \cdot P \tag{4.21}$$

The graphennas are modeled as center-fed graphene planar dipoles with a width of 5 µm and different lengths, over an infinite LT-GaAs substrate with a thickness of 500 µm and a dielectric constant $\varepsilon = 12.9$. The electrically-thin h-BN substrate (with a thickness of 14 nm, less than $\lambda/1000$) has a negligible impact in the simulation results. Figure 4.23 shows a diagram of the antenna model used in the simulations.

For this analysis, the parameters for the photoconductive source in Table 4.2 are considered, unless otherwise specified. The impedance of the photoconductive source is obtained from the source conductance as $Z_s(t) = 1/G_s(t)$ [187].

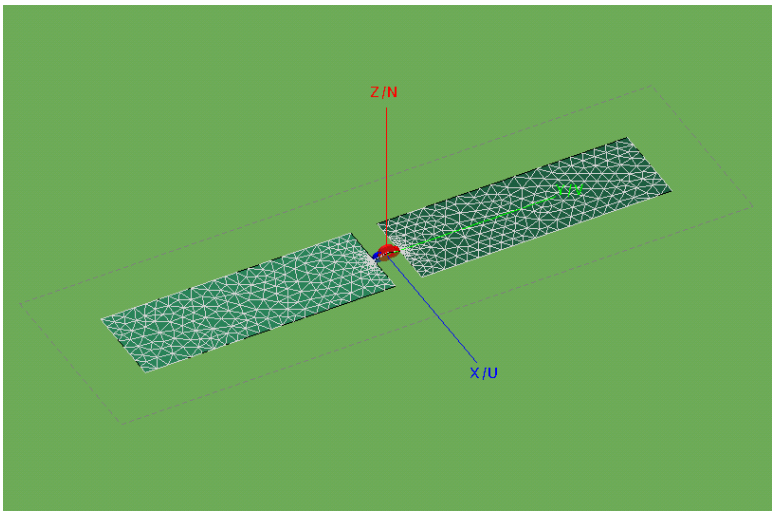

Figure 4.23: Schematic model of the dipole graphenna considered.

Considering a photoconductive source with the described parameters, the source impedance has a minimum value of 2.24 kΩ, consistently with typical values for photoconductors. The antenna input impedance is obtained by numerical simulation and it ranges from 0.73 kΩ to 3.15 kΩ, presenting values up to two orders of magnitude higher than comparable metallic antennas.

Figure 4.24 shows the average radiated power as a function of frequency for graphennas with lengths of 10, 20, 30 and 40 µm (from right to left) and width of 5 µm, fed by the previously described photoconductive source. Conservative values are taken for the electron mobility of the graphene layer, $\mu_g = 20000$ cm^2/Vs, and the chemical potential, $\mu_c = 0.4$ eV. Electron mobilities of graphene over boron nitride of up to 40000 cm^2/Vs have been experimentally observed at room temperature [184]. The spectrum of the radiated signal presents a clear resonance due to the highly frequency-selective behavior of the graphene dipole antenna. Similarly to the behavior observed in metallic antennas, the resonant frequency of a graphenna decreases as its length increases, although, as shown in Section 4.5.2, the resonant frequency of graphennas shows a unique scaling trend with respect to the their length.

As shown in equation (4.21), the power radiated by the graphenna depends on three main factors: the output power of the photoconductive source, the impedance mismatch loss and the antenna radiation efficiency. The results in the

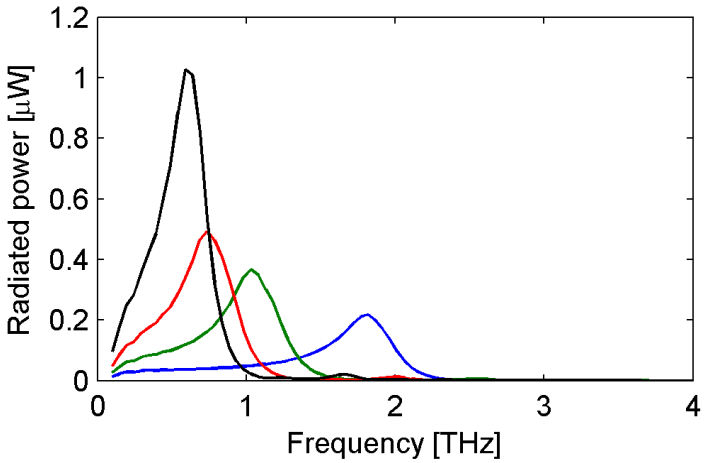

Figure 4.24: Radiated power as a function of frequency for graphennas with lengths of 10, 20, 30 and 40 µm (right to left) and electron mobility μ_g = 20000 cm^2/Vs, fed by a photoconductive source.

considered scenario indicate that, on the one hand, longer antennas resonate at lower frequencies where the power density of the pulses generated by the photoconductive source is mostly concentrated (see Figure 4.22), yielding a higher output power. On the other hand, longer graphennas also have a higher impedance mismatch and lower radiation efficiency than their shorter counterparts, which reduces the final radiated power. Overall, the higher output power of photoconductive sources in lower frequencies dominates and, as shown in Figure 4.24, the radiated power by graphennas increases with the antenna length, reaching a maximum of 1 µW for an antenna length of 40 µm.

Figure 4.25 shows the average radiated power by the graphenna, with the same conditions as in the previous case but with a lower electron mobility of μ_g = 10000 cm^2/Vs. As expected, a decrease in the value of the radiated power is observed with respect to the previous case, mainly due to the reduced radiation efficiency of the graphennas with lower electron mobility. The maximum radiated power is now of 0.27 µW, corresponding to a graphenna with a length of 40 µm.

The influence of the chemical potential of graphene on the power radiated by graphennas is considered next. The application of a chemical potential to the graphene layer results in a higher conductivity and, in consequence, the radiation efficiency of the graphenna is greatly enhanced. At the same time, the impedance

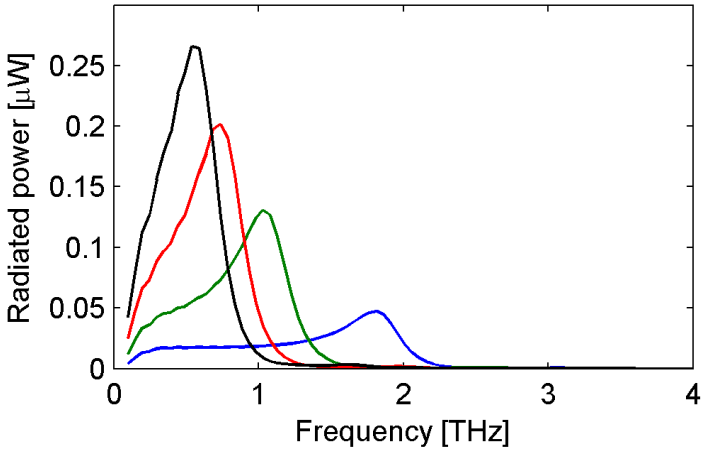

Figure 4.25: Radiated power as a function of frequency for graphennas with lengths of 10, 20, 30 and 40 µm (right to left) and electron mobility μ_g = 10000 cm^2/Vs, fed by a photoconductive source.

mismatch slightly increases and the resonant frequency moves to higher values, where the photoconductive source has a lower output power. Overall, the increase in the antenna radiation efficiency dominates and increasing the chemical potential applied to the graphene layer yields a higher radiated power. This is shown in Figure 4.26, which plots the radiated power by graphennas with a fixed length of 30 µm and width of 5 µm, and an applied chemical potential with values of 0.2, 0.4, 0.7 and 1 eV, from left to right. A radiated power of up to 1.3 µW is obtained with a chemical potential of 1 eV.

Figure 4.27 shows how the power radiated by the graphenna scales with respect to the average optical power fed into the photoconductive source. The antenna length and width are of 30 and 5 µm, respectively, the electron mobility μ_g = 10000 cm^2/Vs and the chemical potential μ_c = 0.4 eV. The radiated power scales linearly with respect to the power of the laser input up to an optical power of around 100 mW, when the radiated power begins to saturate. Increasing the applied bias voltage to the photoconductive source (set to 10 V, 30 V and 50 V, from bottom to top) also enhances the power radiated by the graphenna.

Finally, a different antenna geometry that is commonly used in photoconductive antennas due to its wideband behavior, the bowtie antenna, is considered. Figure 4.28 shows the average power radiated by graphene bowtie antennas with

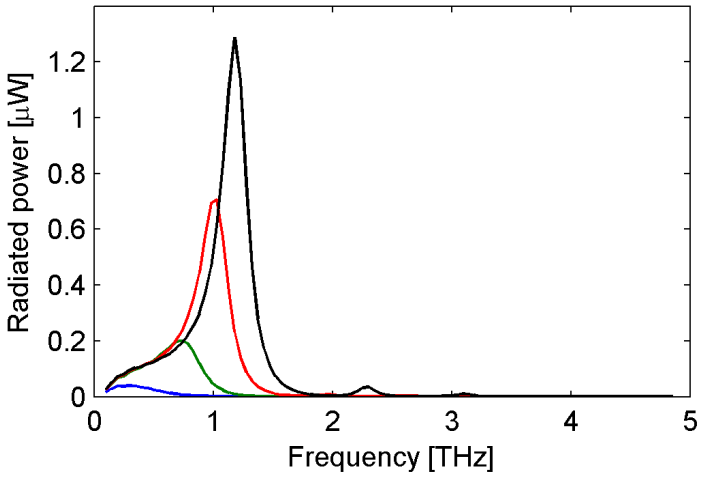

Figure 4.26: Radiated power as a function of frequency for graphennas with a length of 30 µm and chemical potentials of 0.2, 0.4, 0.7 and 1 eV (left to right), fed by a photoconductive source.

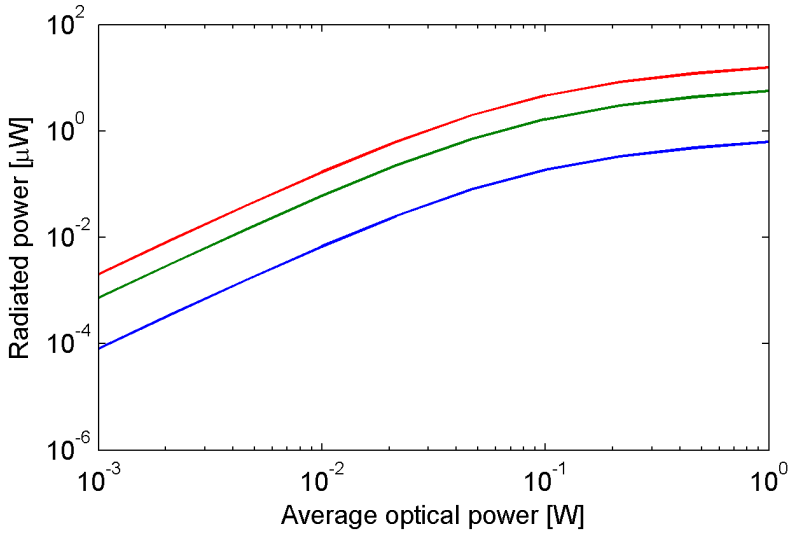

Figure 4.27: Maximum radiated power by the graphenna as a function of the average optical power in the photoconductive source. The bias voltage is set to 10, 30 and 50 V (bottom to top).

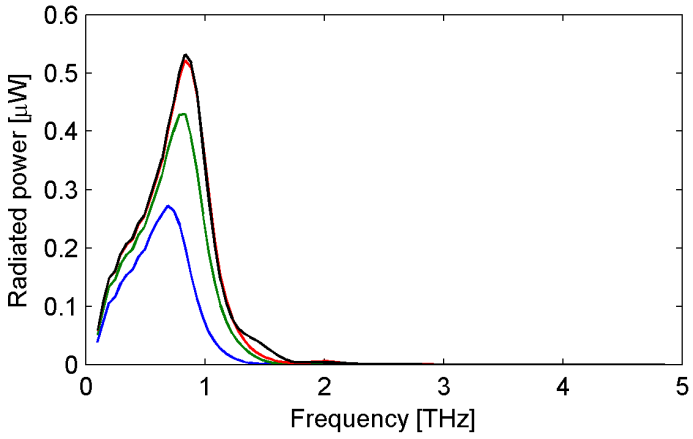

Figure 4.28: Radiated power as a function of frequency for graphene bowtie antennas with a width of 5, 10, 15 and 20 µm (bottom to top), fed by a photoconductive source.

a fixed length $L = 30$ µm, electron mobility $\mu_g = 10000$ cm^2/Vs and chemical potential $\mu_c = 0.4$ eV, and different widths of 5, 10, 15 and 20 µm, from bottom to top. The radiated power is found to increase with the antenna width, as expected due to its larger area, whereas the antenna resonant frequency is relatively independent of its width. Comparing the radiated power of two graphennas with the same configuration but different geometry, one a bowtie antenna with a width of 10 µm (Figure 4.28) and the other a planar dipole with a width of 5 µm and (Figure 4.25), which have approximately the same area, the radiated power by the bowtie antenna is found to be approximately twice that of the dipole antenna. This result confirms that, due to its wideband nature, the bowtie antenna is capable to radiate a higher fraction of the power generated by the photoconductive source and it is therefore better suited to maximize the output power of a photoconductive antenna.

4.7 Summary and concluding remarks

Graphene RF plasmonic antennas, or *graphennas*, are envisaged to allow nanosystems to transmit and receive information, creating a novel paradigm known as graphene-enabled wireless communications. In this chapter, a simple model for a

graphenna, made of a rectangular graphene patch based on a dielectric substrate, is considered. The propagation of SPP waves in graphene has been modeled by means of its dispersion relation and the graphene conductvity. This study has also allowed obtaining the scattering, absorption and extinction cross sections of a graphenna, both analytically and by simulation.

Moreover, a numerical parametric study of the radiation properties of graphennas confirmed that a graphenna with dimensions of a few micrometers resonates in the terahertz band, consistently with the theoretical models. Moreover, the dependence of the antenna resonant frequency on several parameters, such as the dimensions of the graphene patch and the dielectric substrate, the chemical potential of graphene and its relaxation time, have been observed. The radiation pattern of a graphenna has been found to be very similar to that of an equivalent metallic antenna. These results show that graphennas can be tuned in a wide range by changing their dimensions or applying an external electrostatic bias.

Furthermore, the scalability of the resonant frequency in graphennas and miniaturized metallic antennas has been compared as a function of their length. The results proved that the resonant frequency in graphennas increases more slowly than in metallic antennas as their length is reduced. In particular, the derived scaling trends have shown that, when considering submicrometer-length antennas, the resonant frequency of graphennas is up to two orders of magnitude lower than that of metallic antennas with the same size.

Finally, the feasibility of feeding graphennas with photoconductive terahertz sources has been shown, achieving a radiated power in the order of 1 µW. This approach helps overcoming the two main challenges presented by the experimental demonstration of graphennas: the impedance mismatch between the terahertz source and the antenna, and the low antenna radiation efficiency. The obtained results show that graphennas radiate terahertz pulses with a power in the same order of magnitude than traditional metallic photoconductive antennas, while presenting a better scalability than metallic antennas when their dimensions are reduced to the micrometer range.

The provided models, results and guidelines may be useful for designers of future graphennas, which will allow the implementation of wireless communications among nanosystems.

Chapter 5

The terahertz channel in graphene-enabled wireless communications

Described in Chapter 4, graphene RF plasmonic antennas, or *graphennas*, radiate EM waves with a frequency lying in the terahertz band, i.e., from 0.1 to 10 THz. Thanks to this unique property, graphennas are envisaged to allow the implementation of wireless communications among nanosystems, enabling the paradigm of GWC.

This chapter explores the wireless terahertz channel at very short transmission ranges (below 1 meter), which is the expected operation environment of future graphennas. First, Section 5.1 analyzes the effects of molecular absorption, an additional attenuation process caused by the absorption of terahertz radiation by several molecules present in the atmosphere [188]. Second, Section 5.2 evaluates the scaling trends of the channel capacity of wireless communications to the nanoscale, comparing the scenario of GWC with that of traditional wireless communications [189]. Finally, Section 5.3 summarizes this section.

5.1 Effects of molecular absorption in short-range terahertz communications

In the last years, the terahertz band has been widely analyzed for its applications in the fields of imaging [190, 191] and spectroscopy [192, 193], but it is still a relatively unexplored frequency band from the communications perspective. A channel model oriented for ultra-short-range wireless communications in the terahertz band has been used to calculate its information capacity [121].

In what follows, a communication channel in the terahertz frequency band is considered, focusing on transmission distances from one centimeter to several meters. Based on a channel model for short-range wireless communications in the terahertz band [121], the impact of molecular absorption on the performance of GWC is studied. In particular, several performance metrics are derived from the impulse response of molecular absorption in the time and frequency domains, as well as their scalability with respect to the transmission distance [188]. A sample scenario where this study may be useful is that of Graphene Wireless Networks-on-Chip (GWNoC) [25], a novel approach that considers GWC to share information among the cores in a multiprocessor.

5.1.1 System model

In this work, a scenario of GWC where the transmission distance ranges from one centimeter up to several meters is considered. The channel is modeled as a standard medium with 10% of water vapor molecules. Moreover, given the target application, EM waves are assumed to propagate unidirectionally following a ray tracing model [119]; therefore, the free-space propagation loss is not considered. A single point-to-point wireless link is assumed, where communication is performed by the transmission of extremely short (subpicosecond-length) pulses. This scheme allows using the whole terahertz frequency band and maximizes the achievable data rate, in the order of Tbits/s.

In this context, focusing on the phenomenon of molecular absorption in the terahertz band, the channel is analyzed from both the frequency domain and, most importantly, the time domain. This dual analysis allows the evaluation of

different performance metrics of molecular absorption. For instance, from the frequency domain, the *available bandwidth* for transmission can be computed, defined as the frequency band where the attenuation caused by molecular absorption is below a given threshold.

As previously described in Section 1.3.2, molecular absorption can be expressed as [121]:

$$A_{\text{abs}}(f,d) = \frac{1}{\tau_m} = e^{k(f)d} \tag{5.1}$$

where f is the frequency, d is the distance, τ_m is the transmittance of the medium and k is the medium absorption coefficient. The channel transfer function of molecular absorption can be then obtained from Eq. (5.1) as $H(f,d) = 1/A_{\text{abs}}(f,d)$. The impulse response of molecular absorption is the inverse Fourier transform of the channel transfer function: $h(t,d) = \mathcal{F}^{-1}\left[1/A_{\text{abs}}(f,d)\right]$. The time-domain response of molecular absorption allows the calculation of several relevant performance metrics [194], such as:

- *Response amplitude:* the amplitude $c_{\max}$ of the molecular absorption impulse response is defined as the maximum value of its instantaneous power: $c_{\max} = \max_t |h(t,d)|^2$. A high amplitude value means that the energy is highly concentrated around the response peak. In most applications, receiving a signal with a high amplitude allows for a precise detection of the transmitted information.

- *Response width:* the width t_{w} of the impulse response is defined as the time interval during which the impulse response has a higher value than half the response peak, i.e., $t_{\text{w}} = t_0 : (h(t_0,d) < c_{\max}/2) \wedge (\forall t : t < t_0 \rightarrow h(t,d) \geq c_{\max}/2)$. A high response width means that the molecular absorption distorts the transmitted pulses by increasing its width. Due to this pulse widening effect, molecular absorption might reduce the achievable data rate in GWC.

- *Response energy:* the energy E_{p} of the impulse response is defined as the integral of its instantaneous power over time: $E_{\text{p}} = \int_t |h(t,d)|^2 \text{d}t$. The energy

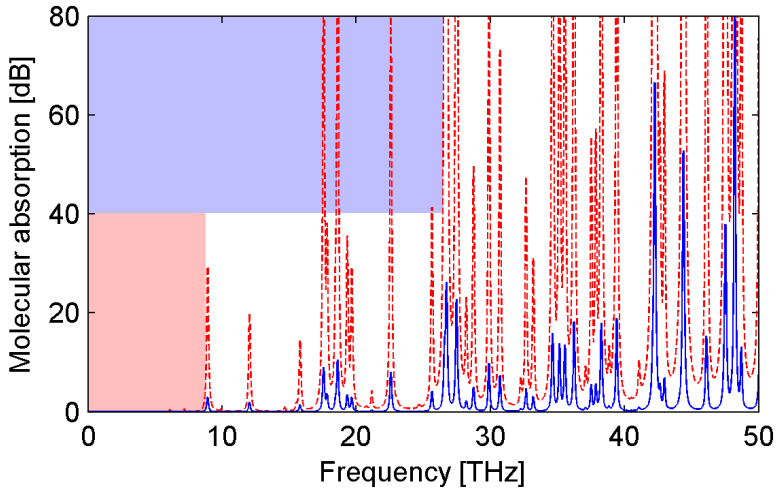

Figure 5.1: Molecular absorption in dB as a function of frequency for transmission distances of 1 cm (blue solid line) and 10 cm (red dashed line). The top blue (bottom red) background shows the frequency region which determines the available bandwidth for a transmission distance of 1 cm (10 cm).

value indicates how molecular absorption affects the energy of the transmitted pulses. A high pulse energy will improve the detection performance of non-coherent receivers in GWC.

5.1.2 Results

Quantitative results which show some properties of the short-range terahertz channel with molecular absorption as obtained next, as well as design parameters in a GWC system. Figure 5.1 shows the molecular absorption of the terahertz channel as a function of frequency, for transmission distances of 1 cm and 10 cm. The molecular absorption is highly dependent on the transmission distance, derived from its exponential dependence with the distance, as shown in Eq. (5.1). In this particular case, both the number of absorption peaks and their amplitude notably increase when the transmission distance changes from 1 to 10 cm.

As observed in Figure 5.1, molecular absorption creates several peaks of very high attenuation. These absorption peaks will create a limitation in the available bandwidth in GWC (defined in Section 5.1.1). In order to quantify the available

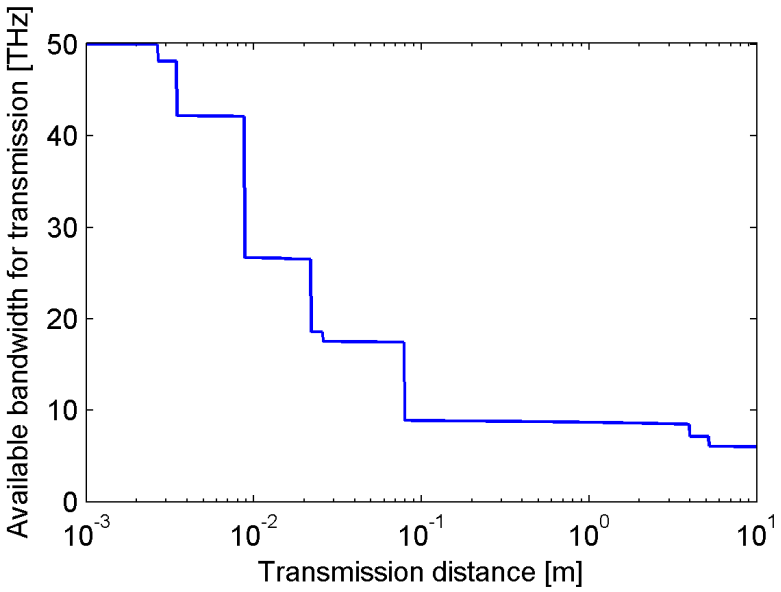

Figure 5.2: Available bandwidth in the frequency band from 0 to 50 THz due to molecular absorption, as a function of the transmission distance.

bandwidth as a function of the transmission distance, the range of frequencies within the 0 to 50 THz band at which the value of molecular absorption is below 10 dB is considered. Figure 5.1 shows graphically the range of frequencies which determine the available bandwidth for transmission distances of 1 cm (27 THz, top blue background) and 10 cm (9 THz, bottom red background). Figure 5.2 shows a semi-log plot of the scalability of the available bandwidth with respect to the transmission distance. A rapid decrease of the bandwidth as the distance increases, with several steps of different sizes corresponding to the molecular absorption peaks, is observed. For instance, molecular absorption has a negligible effect at short transmission distances and the whole 50 THz band is usable for distances up to 2.5 mm. On the other hand, for distances greater than 5 m, less than 6 THz are available for a molecular absorption-free transmission.

As mentioned in the previous section, the expression of the frequency-dependent molecular absorption can be used to obtain the channel impulse response due to molecular absorption. Figure 5.3 shows both the channel transfer function and the impulse response of molecular absorption for two transmission distances: 10 cm and 1 m. For a transmission distance of 10 cm (red dashed line), the channel

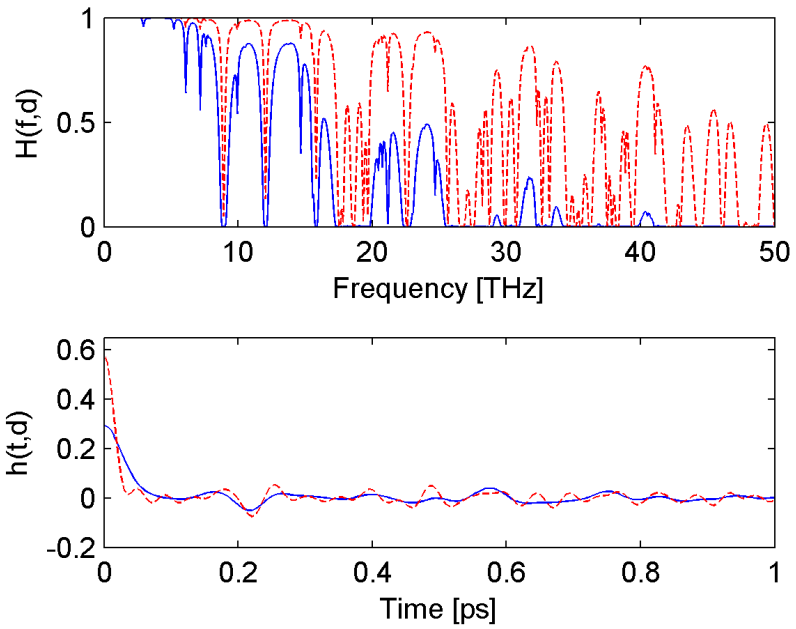

Figure 5.3: Channel transfer function $H(f, d)$ (top) and channel impulse response $h(t, d)$ (bottom) of the molecular absorption for transmission distances of $d =$ 10 cm (red dashed line) and $d = 1$ m (blue solid line).

transfer function shows a significant spectral content throughout most of the frequency band; whereas, when the distance is increased to 1 m (blue solid line), the molecular absorption blocks almost all the frequency components above 25 THz of the transmitted signal. Furthermore, this attenuation of the high-frequency components of the signal causes the channel impulse response to lower peak amplitude, a larger width and a smoother shape for the higher transmission distance. Assuming that the transmitted signals consist of subpicosecond pulses [91], the main implication of the dispersive behavior of the channel impulse response is that molecular absorption distorts the transmitted pulses, decreasing their amplitude and increasing their width. These effects are studied in more detail next.

Figure 5.4 shows a semi-log plot of the width of the molecular absorption impulse response t_{w} as a function of the transmission distance d. A clear dependence of the width of the impulse response on the distance between transmitter and receiver is observed, with a scaling trend of $t_{\mathrm{w}} = \Theta\left(\sqrt[5]{d}\right)$ (notice the logarithmic

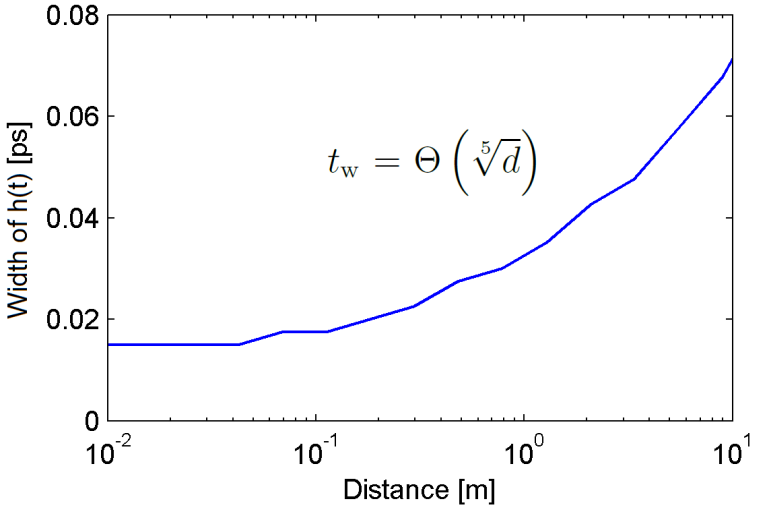

Figure 5.4: Semi-log plot of the width of the channel impulse response due to molecular absorption, as a function of the transmission distance.

horizontal axis in Figure 5.4). In particular, in order to achieve a communication throughput in the order of 1 Tbit/s, the received pulses will need to have a width of less than 1 ps. This result shows that, for instance, for a transmission distance of 3 m, the distortion introduced by molecular absorption is limited to 0.05 ps, thereby reducing the maximum achievable throughput by around 5 %. In short, the width of the impulse response allows, given a target throughput, to derive the maximum transmission distance, as limited by molecular absorption.

The amplitude of the channel impulse response $c_{\max}$ is related to the attenuation caused by molecular absorption to a signal propagating in the terahertz channel. Figure 5.5 shows that, as expected, the amplitude of the impulse response decreases as the transmission distance increases, with a scaling trend of $c_{\max} = \Theta\left(1/\sqrt{d}\right)$. For instance, the amplitude decreases by a factor of 10 when the transmission distance changes from 1 cm to 1 m. This substantial decrease indicates that the amplitude of the transmitted pulses will be highly attenuated by molecular absorption, thereby potentially impairing their detection by the receiver.

Another important metric to consider is how molecular absorption affects the energy of the transmitted signals. Since molecular absorption has been found to

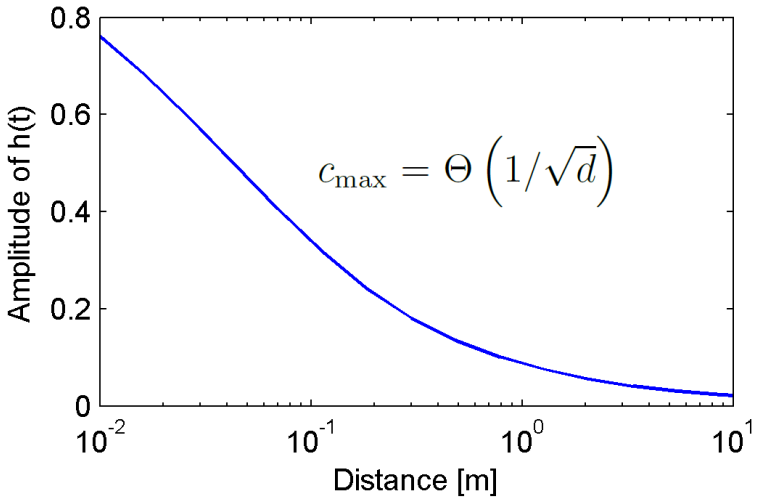

Figure 5.5: Semi-log plot of the amplitude of the channel impulse response due to molecular absorption, as a function of the transmission distance.

attenuate the transmitted signals (Figure 5.5) but also to increase their width (Figure 5.4), it is not clear how the signal energy measured by the receiver will scale with the transmission distance. Figure 5.6 shows that the energy of the channel impulse response due to molecular absorption decreases with respect to the distance, with a scaling trend of $E_{\mathrm{p}} = \Theta\left(1/\sqrt[3]{d}\right)$. This result shows that the reduction of the signal energy occurs at a lower pace than that of its amplitude; by comparision, the energy decreases only by a factor of 4 when increasing the transmission distance by two orders of magnitude, from 1 cm to 1 m. As a consequence, an non-coherent detection scheme based on the signal energy may be better suited than a coherent detector in GWC affected by molecular absorption.

For the sake of comparison, in a scenario of an ideal free-space wireless communication channel with no molecular absoprtion, the channel impulse response would be a delta function independently of the transmission distance. To summarize the results of this section, Table 5.1 compares the scalability of the analyzed performance metrics of molecular absorption in GWC to the case of ideal free-space wireless communications, as a function of the transmission distance d.

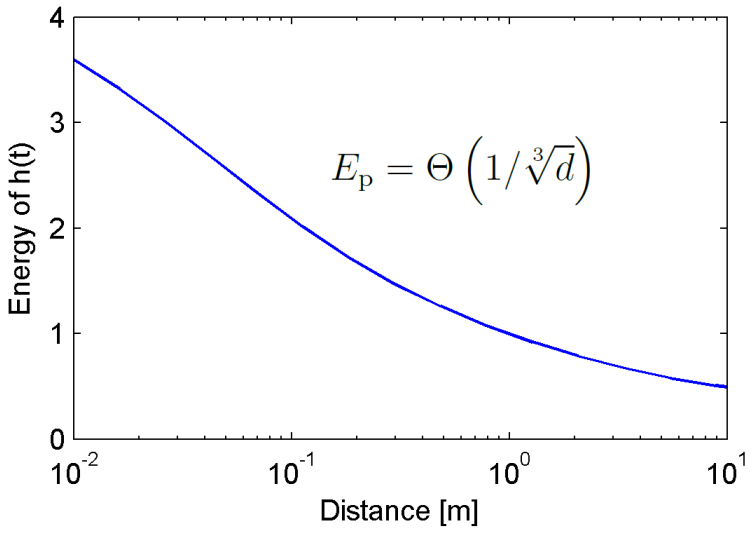

Figure 5.6: Semi-log plot of the energy of the channel impulse response due to molecular absorption, as a function of the transmission distance.

Metric	**Molecular absorption**	**No molecular absorption**
Width of the impulse response	$\Theta\left(\sqrt[5]{d}\right)$	$\Theta\left(1\right)$
Amplitude of the impulse response	$\Theta\left(1/\sqrt{d}\right)$	$\Theta\left(1\right)$
Energy of the impulse response	$\Theta\left(1/\sqrt[3]{d}\right)$	$\Theta\left(1\right)$

Table 5.1: Scalability of the performance metrics of molecular absorption in GWC.

5.2 Scalability of the channel capacity in GWC to the nanoscale

The scalability of the channel capacity is next analyzed in a scenario of GWC [189], such as the one shown in Figure 5.7. In particular, the dependencies between key scale parameters when the system size shrinks to the nanoscale are investigated. The main contributions of this section can be summarized as follows:

1. Analytical expressions for the scalability of the channel capacity of wireless communications towards the nanoscale are derived as a function of three key scale parameters: the antenna length L, the transmission distance d and the transmitted power P_T (see Figure 5.7). The case in which the radiating element is a graphenna is compared to that of a metallic antenna. The obtained results show important differences, giving graphennas a scalability advantage over metallic antennas.

2. Based on the previous analytical model, quantitative values of the capacity expressions are obtained by assuming realistic parameters, comparing the cases when a graphenna and a metallic antenna are used to transmit the information.

3. Design guidelines which indicate how the antenna transmission distance and the transmitted power need to scale as a function of the antenna length in order to keep the network feasible are derived. These results establish a general framework which may serve as a guide for designers of future GWC networks.

5.2.1 Graphene-enabled wireless communications

GWC exhibit several important differences with respect to traditional wireless communications techniques. Three of the most relevant features of GWC are described next. First, the propagation of SPP waves in graphennas, which cause them to resonate in the terahertz band, is examined. Second, the effects of molecular absorption and noise, two novel characteristics of the wireless channel in the terahertz band, are described. Finally, the potential impact of the huge available bandwidth in GWC is discussed.

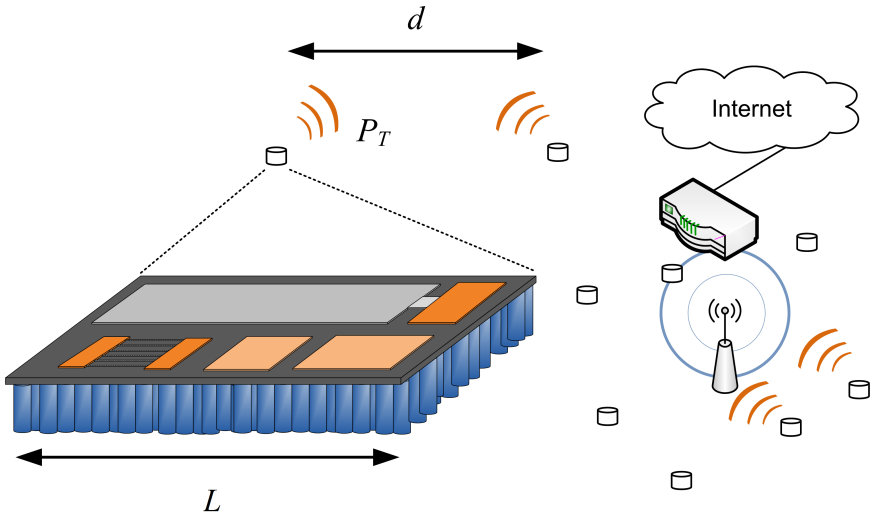

Figure 5.7: Schematic diagram of a GWC network (right) and a magnified individual nanosystem (left). The scale parameters, namely the antenna length L, the transmission distance d and the transmitted power P_T, are shown.

Antenna resonant frequency

The propagation speed of EM waves in commonly-used metallic antennas is related to the speed of light c. For instance, the wave propagation speed in resonant metallic patch antennas is $v_p = c/\sqrt{\varepsilon_r}$, where ε_r is the dielectric constant of the substrate, and the antenna length is typically around half a wavelength: $L \approx \lambda/2$. As a consequence, the resonant frequency of such an antenna, given by $f_R = v_p/\lambda \approx c/\left(2\sqrt{\varepsilon_r}L\right)$, is inversely proportional to its length. This relationship imposes a limit in the minimum size of a RF antenna (i.e., with a resonant frequency up to the terahertz band), in the order of 100 µm, which prevents the possibility of integrating them into nanosystems just a few µm in size.

In order to overcome this issue, nanomaterials such as graphene offer the possibility of building much smaller antennas due to their novel plasmonic properties. Indeed, graphene has been shown to support the propagation of SPP waves at frequencies as low as the terahertz band. In particular, as previously described in Section 4.5.2, the dispersion relation of SPP waves in graphene causes graphennas to have not only a much lower resonant frequency than their metallic counterparts, but their resonant frequency also scales better as the antenna length is reduced.

The results depicted in Figure 4.20 showed that, whereas the resonant frequency of gold antennas is inversely proportional to their length: $f_{Rm} = \Theta(1/L)$, the resonant frequency of graphennas scales inversely proportional to the square root of the antenna length: $f_{Rg} = \Theta\left(1/\sqrt{L}\right)$. In consequence, graphennas just a few µm long resonate in the terahertz band, at a much lower frequency than metallic antennas with the same size.

Throughout this section, the subindex m denotes the parameters corresponding to a metallic antenna, and the subindex g the case in which a graphenna is considered.

Molecular absorption and noise

As previously introduced in Section 1.3.2, molecular absorption and molecular noise are processes by which part of the energy of EM waves in the terahertz band is converted into internal kinetic energy of the excited molecules in the medium. As a consequence, these two phenomena need to be taken into account when analyzing the physical channel in a scenario of GWC.

Bandwidth and channel capacity

Since a graphenna is able to radiate EM waves in the terahertz band, the corresponding bandwidth associated to this frequency and, ultimately, the capacity of the GWC will be extremely high (up to Tbits/s). One may think that such a large capacity will not be needed, since it is envisaged that a single nanosystem will have low throughput requirements. However, that network designers may take advantage of this large channel capacity in order to design novel protocols specifically adapted to GWC networks.

In traditional wireless networks, the channel capacity is usually the bottleneck that limits the network throughput. In consequence, many networking protocols are designed to require a low bandwidth in order to maximize the network throughput. In contrast, the envisaged huge channel capacity in GWC opens the door to new protocols that take advantage of a virtually unlimited available bandwidth to optimize other performance metrics which may be more relevant in GWC networks, such as reducing the energy consumption or the complexity

of the nanosystems.

5.2.2 Channel capacity at the nanoscale

The goal of this section is to find analytical expressions for the scalability of the channel capacity of wireless communications towards the nanoscale, as a function of three key scale parameters: (i) the antenna length L, (ii) the transmission distance d, and (iii) the total transmitted power P_T. This analysis is performed for two scenarios: (i) when the transmitters use metallic antennas to radiate the EM signal, and (ii) when graphennas are used (with their unique features introduced in Section 5.2.1). The first scenario is taken as a reference in order to evaluate the results obtained in the latter case.

As previously outlined, a graphenna is able to radiate EM waves in the terahertz band. In consequence, the physical channel in GWC in the very short range will have a very large bandwidth [121] and a highly frequency-dependent behavior. In order to compute its capacity, the channel needs to be divided in narrow sub-bands so that, in each sub-band, the channel attenuation and the noise power spectral density can be considered locally flat. The total channel capacity is then obtained as the combined capacity of all its sub-bands. The capacity of a single sub-band C_i is expressed using the Shannon limit theorem [195]:

$$C_i = B_i \log_2 \left(1 + \frac{S_i}{A_i N_i}\right) \tag{5.2}$$

where B_i is the width of the frequency band, S_i the power radiated by the transmitter in this band, A_i the sub-band attenuation and N_i the noise power in the frequency band.

The total channel capacity C [196] can be obtained by taking the limit of the sub-band capacity when $B_i \to 0$ and integrating it over the whole frequency band, which leads to the following expression [197]:

$$C = \max_{S(f):\int_B S(f)df \leq P_T} \int_B \log_2 \left(1 + \frac{S(f)}{A(f)N(f)}\right) df \tag{5.3}$$

where $S(f)$ is the transmitted power spectral density, $A(f)$ stands for the channel attenuation, $N(f)$ is the noise power spectral density at the receiver and B is the

system bandwidth. Note that (5.3) also applies when the noise is not white but frequency-dependent, such as molecular noise.

In order to find an expression for the channel capacity C as a function of the scale parameters, the magnitudes that determine the channel capacity according to (5.3) are first considered: the transmitted power spectral density $S(f)$, the channel attenuation $A(f)$, the noise power spectral density $N(f)$ and the system bandwidth B. Next, each of them is expressed as a function of the scale parameters L, d and P_T, for the two previously mentioned scenarios, considering a graphenna and a metallic antenna, respectively. Finally, these results are combined to find an analytical expression for the channel capacity C.

Transmitted power spectral density

An expression for the spectral density of the radiated power by the transmitting antenna is derived next. Assuming that the transmitter had a full knowledge of the wireless channel, the optimal power allocation would be achieved through waterfilling. However, since that knowledge would require a feedback loop to send this information from the receiver back to the transmitter, it is conservatively assumed that the transmitter does not have any knowledge of the channel. In this case, the optimal modulation is known as flash signaling, an asymptotic form of on-off signaling where the *on* level has unbounded power and the duty cycle is vanishingly small [198]. In this case, the input signal has a flat power spectral density over the entire frequency band:

$$S(f) = \begin{cases} P_T/B & \text{if } 0 < f < B, \\ 0 & \text{otherwise.} \end{cases} \tag{5.4}$$

where P_T is the total power radiated by the transmitting antenna.

A modulation scheme based on very short Gaussian pulses specially suited for GWC [181] is a promising candidate to modulate the EM waves radiated by graphennas because of the simplicity to generate and detect pulses (there is no carrier) and its high spectral efficiency (a very short Gaussian pulse virtually occupies the whole frequency band). This approach actually constitutes a realistic implementation of flash signaling for GWC and it is accurately approximated by

the previous model.

Channel attenuation

The most promising applications of GWC, such as WNSN and GWNoC, have expected transmission distances in the order of several millimeters. This value, although low compared to traditional wireless communication systems, is around one order of magnitude larger than the wavelength of terahertz EM waves. In consequence, graphennas will operate in far field conditions and, therefore, macroscale physical channel models can applied to analyze GWC. The total attenuation, or path loss, in a GWC system can be expressed as [121]:

$$A = A_{spread} A_{abs} \tag{5.5}$$

where A_{spread} is the spreading loss and A_{abs} is the molecular absorption loss.

The molecular absorption loss, introduced in Section 5.2.1, can be modeled by the following analytical expression [121]:

$$A_{abs} = \frac{1}{\tau_m} = e^{k(f)d} \tag{5.6}$$

where τ_m is defined as the transmittance of the medium and k is the medium absorption coefficient. In the targeted scenario, where the transmission distance tends to zero, the value of the molecular absorption loss tends to 1:

$$\lim_{d \to 0} A_{abs} = \lim_{d \to 0} e^{k(f)d} = 1 \tag{5.7}$$

Therefore, the molecular absorption loss will have a negligible effect in the envisaged scenarios of GWC. The total attenuation is then obtained considering only the spreading loss, given in the Fraunhofer region by the well-known expression for the free-space path loss:

$$A = A_{spread} = \left(\frac{4\pi f d}{c} \right)^2 \tag{5.8}$$

The antenna gain is expressed as a function of the effective area and the wavelength as $G = 4\pi A_{eff}/\lambda^2$. Since, in a resonant patch antenna, both A_{eff}

and λ^2 are proportional to the squared antenna length L^2, the gain is a constant with respect to the scale parameters. Therefore, the values of the gain of the transmitting and receiving antennas will not influence this scalability analysis.

Noise power spectral density

Finally, there are two main contributors to the ambient noise in the terahertz channel: thermal noise and molecular noise (introduced in Section 5.2.1) [121]. The total noise power spectral density $N(f)$ is obtained in the general case as

$$N(f,d) = \frac{2Rhf}{e^{\frac{hf}{k_B T}} - 1} \tag{5.9}$$

where R is the resistor value, h the Planck's constant, k_B the Boltzmann constant and T the total temperature. For frequencies below a few terahertz ($hf \ll k_B T$), this expression can be approximated by the following:

$$N(f,d) = k_B(T_{sys} + T_{mol}(f,d)) \tag{5.10}$$

where the total temperature is expressed as $T = T_{sys} + T_{mol}(f,d)$, corresponding to the system temperature and the molecular noise temperature, respectively. The molecular noise temperature can be expressed as follows [121]:

$$T_{mol}(f,d) = T_0\varepsilon = T_0(1-\tau_m) = T_0(1-e^{-k(f)d}) \tag{5.11}$$

where T_0 is the standard temperature, ε is known as the emissivity of the medium, τ_m is the transmittance of the medium and k the medium absorption coefficient. As it happened with molecular absorption, molecular noise tends to disappear when the transmission distance is small:

$$\lim_{d\to 0} T_{mol}(f,d) = \lim_{d\to 0} T_0(1-e^{-k(f)d}) = 0 \tag{5.12}$$

In consequence, the main contributor to the noise power spectral density in the terahertz channel at the nanoscale is the thermal noise. Approximating the system temperature by the standard temperature $T_0 = 293$ K, a constant noise

power spectral density in the whole frequency band, denoted by N_0, is obtained:

$$N(f,d) = k_B T_{sys} = k_B T_0 = N_0 \tag{5.13}$$

Bandwidth

As just observed, when the transmission distance is sufficiently small, molecular absorption and noise become negligible and the channel bandwidth is the whole terahertz band. Therefore, the total available bandwidth will be limited by the antenna bandwidth, which can be obtained as $B = f_R/Q$, where f_R is the antenna resonant frequency and Q its quality factor. The resonant frequency of metallic and graphene antennas, previously derived in Section 5.2.1, can be expressed as:

$$f_{Rm} = \frac{k_1'}{L} \tag{5.14}$$

$$f_{Rg} = \frac{k_2'}{\sqrt{L}} \tag{5.15}$$

where k_1' and k_2' are proportionality constants and L is the antenna length. The quality factor of metallic and graphene antennas does not depend significantly with the antenna size [65]. Therefore, new proportionality constants can be defined as $k_1 = k_1'/Q$ and $k_2 = k_2'/Q$ to obtain an expression of the system bandwidth as a function of the scale parameters:

$$B_m = \frac{k_1}{L} \tag{5.16}$$

$$B_g = \frac{k_2}{\sqrt{L}} \tag{5.17}$$

Expression of the channel capacity

Now, the expressions obtained in (5.4), (5.8) and (5.13) are combined with the definition of the channel capacity (5.3) to obtain the capacity of a nanoscale wireless communication channel:

$$
\begin{aligned}
C(B,d,P_T) &= \int_0^B \log_2\left(1+\frac{P_T/B}{\left(\frac{4\pi fd}{c}\right)^2 N_0}\right) df \\
&= \frac{B}{\log 2}\log\left(1+\frac{c^2 P_T}{(4\pi d)^2 B^3 N_0}\right) \\
&+ \frac{c\sqrt{P_T}}{2\log(2)\pi d\sqrt{N_0 B}}\arctan\frac{4\pi d B^{3/2}\sqrt{N_0}}{c\sqrt{P_T}}
\end{aligned}
\tag{5.18}
$$

Recalling the previous expressions for the bandwidth (5.16) and (5.17), the channel capacity C can be expressed as a function of the three key scale parameters: the antenna length L, the transmission distance d and the transmitted power P_T (c, N_0, k_1 and k_2 are constants):

$$
\begin{aligned}
C_m(L,d,P_T) &= \frac{k_1}{\log(2)L}\log\left(1+\frac{c^2 L^3 P_T/d^2}{(4\pi)^2 N_0 k_1^3}\right) \\
&+ \frac{c\sqrt{LP_T/d^2}}{2\log(2)\pi\sqrt{N_0 k_1}}\arctan\frac{4\pi\sqrt{N_0 k_1^3}}{c\sqrt{L^3 P_T/d^2}}
\end{aligned}
\tag{5.19}
$$

$$
\begin{aligned}
C_g(L,d,P_T) &= \frac{k_2}{\log(2)\sqrt{L}}\log\left(1+\frac{c^2 L^{3/2} P_T/d^2}{(4\pi)^2 N_0 k_2^3}\right) \\
&+ \frac{c\sqrt[4]{L}\sqrt{P_T/d^2}}{2\log(2)\pi\sqrt{N_0 k_2}}\arctan\frac{4\pi\sqrt{N_0 k_2^3}}{cL^{3/4}\sqrt{P_T/d^2}}
\end{aligned}
\tag{5.20}
$$

where the factor P_T/d^2 has been isolated in both expressions. The capital importance of this quotient on the scalability of the channel capacity to the nanoscale will be seen in Section 5.2.3.

Quantitative results

In order to obtain quantitative results of the channel capacity as a function of L and d, realistic values are assigned to the parameters in equations (5.19) and (5.20), considering an envisaged scenario of GWC. Next follows a description of these values and the rationale behind the choices made.

First, the values of the constants k_1' and k_2' are obtained from the results of the antenna resonant frequency in Figure 4.20 as $k_1' = 1.7 \cdot 10^8$ and $k_2' = 4 \cdot 10^9$. Unity gain antennas and a quality factor $Q = 5$ are considered [171]. In consequence, the proportionality constants will be $k_1 = 3.4 \cdot 10^7$ and $k_2' = 8 \cdot 10^8$.

Regarding the transmitted power, a power spectral density of 10^{-10} W/Hz over a bandwidth of 1 THz is considered. With respect to molecular absorption and noise, the medium absorption coefficient of a standard atmosphere has been found to have a maximum value of approximately $k_{max} = 3.5$ m^{-1} [121]. Then, considering typical transmission distances for GWC of up to $d_{max} = 1$ cm, the maximum value of molecular absorption in a realistic GWC scenario is $A_{abs} = e^{k_{max} d_{max}} \approx 1.036$, which is negligible in comparison with the attenuation due to the much larger spreading loss. This result confirms that molecular absorption will not have a significant effect on communication in short-range wireless communications, as previously obtained analytically. Similarly, the contribution of molecular noise is also negligible in comparison with thermal noise: $T_{mol} = T_0(1 - e^{-k_{max} d_{max}}) \approx 0.034 T_0$. With respect to thermal noise, its spectral density has a value of $N_0 = k_B T_0 \approx 1.38 \cdot 10^{-23} \cdot 293$ W/Hz.

Finally, a realistic range of values for the antenna length L and the transmission distance d are selected. For the former, the interval between 0.05 and 5 µm is chosen, and from 1 to 10 mm for the latter. In both cases, the chosen values are inspired by the range of envisaged values for nanosystems. A summary of the selected parameters is shown in Table 5.2. The resulting quantitative values for the channel capacity are shown in Figure 5.8 for a metallic antenna, and in Figure 5.9 for a graphenna.

The results obtained when evaluating equations (5.19) and (5.20) show that the behavior of the channel capacity at the nanoscale differs significantly depending on whether the use of graphennas or metallic antennas is considered. On the one hand, the absolute value of the channel capacity is up to one order of magnitude higher when metallic antennas are used. On the other hand, while metallic antennas show a peak in the channel capacity for a value of L of a few µm, when considering graphennas the channel capacity increases monotonically as L decreases. This observation indicates that, thanks to the unique properties of plasmonic EM waves in graphene, the channel capacity in GWC scales bet-

Parameter	Symbol	Value
Antenna length	L	0.05–5 µm
Transmission distance	d	1–10 mm
Total power radiated by the transmitter	P_T	100 W
Proportionality constant in metallic antennas	k_1	$3.4 \cdot 10^7$
Proportionality constant in graphennas	k_2	$8 \cdot 10^8$
Boltzmann constant	k_B	$1.38 \cdot 10^{-23}$ J/K
Standard temperature	T_0	293 K

Table 5.2: Values chosen for the parameters in a typical scenario of GWC.

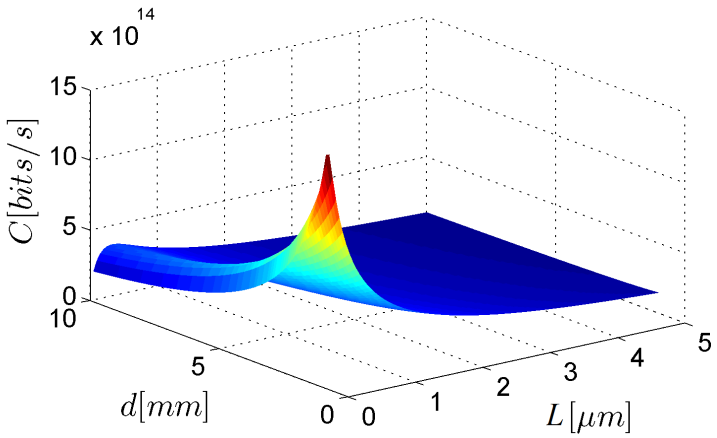

Figure 5.8: Quantitative values of the channel capacity C as a function of the antenna length L and the transmission distance d, when a metallic antenna is considered.

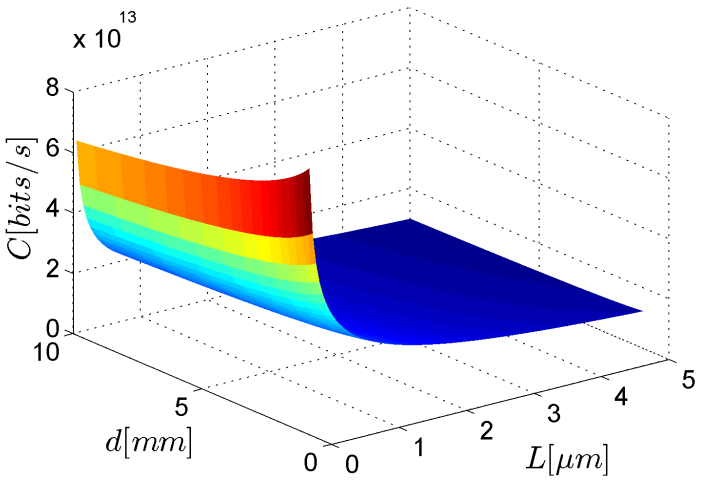

Figure 5.9: Quantitative values of the channel capacity C as a function of the antenna length L and the transmission distance d, when a graphenna is considered.

ter as the dimensions shrink than what is observed when conventional metallic antennas are considered.

Finally, note that these results assume that the transmitted power has a constant value, which might not be realistic in some scenarios. For this reason, an analytical approach is taken next and the limits of the channel capacity of wireless communications are computed when the values of the three considered scale parameters, L, d and P_T, all tend to zero.

5.2.3 Limits of the channel capacity

The objective here is to find closed-form expressions for the channel capacity expressions given by (5.19) and (5.20) in the limit when all three scale parameters tend to zero, i.e., $L \to 0$, $d \to 0$ and $P_T \to 0$. Unfortunately, these limits are not unique, but they depend upon the relationships among L, d and P_T. Thus, in order to find an analytical expression for the capacity of a nanoscale wireless channel, a given relationship among the scale parameters needs to be assumed. Following an approach as general as possible, d and P_T are expressed as a function

of L as follows:

$$d = k_3 L^{\alpha} \tag{5.21}$$

$$P_T = k_4 L^{\beta} \tag{5.22}$$

where k_3 and k_4 are constants and α and β are real positive exponents. In other words, when the antenna length L decreases, both the transmission distance d and the transmitted power P_T are assumed to shrink as well, at relative rates α and β, respectively. Under these assumptions, the channel capacity can be expressed as a function of a single scale parameter, in this case L, obtaining the following expressions:

$$C_m(L) = \frac{k_{11}}{L} \log\left(1 + k_{12} L^{\beta - 2\alpha + 3}\right) + k_{13} L^{\frac{\beta - 2\alpha + 1}{2}} \arctan\left(k_{14} L^{-\frac{\beta - 2\alpha + 3}{2}}\right) \tag{5.23}$$

$$C_g(L) = \frac{k_{21}}{\sqrt{L}} \log\left(1 + k_{22} L^{\beta - 2\alpha + \frac{3}{2}}\right) + k_{23} L^{\frac{\beta - 2\alpha + 1/2}{2}} \arctan\left(k_{24} L^{-\frac{\beta - 2\alpha + 3/2}{2}}\right) \tag{5.24}$$

where k_{ij}, $i \in [1, 2]$, $j \in [1, 4]$ are constants w.r.t. L. The limits when $L \to 0$ of the previous expressions are functions of the parameters α and β:

$$\lim_{L \to 0} C_m(L) = \begin{cases} \infty & \text{if } \beta - 2\alpha > -1, \\ \text{constant} & \text{if } \beta - 2\alpha = -1, \\ 0 & \text{if } \beta - 2\alpha < -1. \end{cases} \tag{5.25}$$

$$\lim_{L \to 0} C_g(L) = \begin{cases} \infty & \text{if } \beta - 2\alpha > -1/2, \\ \text{constant} & \text{if } \beta - 2\alpha = -1/2, \\ 0 & \text{if } \beta - 2\alpha < -1/2. \end{cases} \tag{5.26}$$

where the term $\beta - 2\alpha$ in the expressions above stems from the quotient $P_T/d^2 = \Theta\left(L^{\beta - 2\alpha}\right)$ that appears repeatedly in the capacity expressions (5.19) and (5.20).

The *feasible region* of the network is defined as the scenario in which the chan-

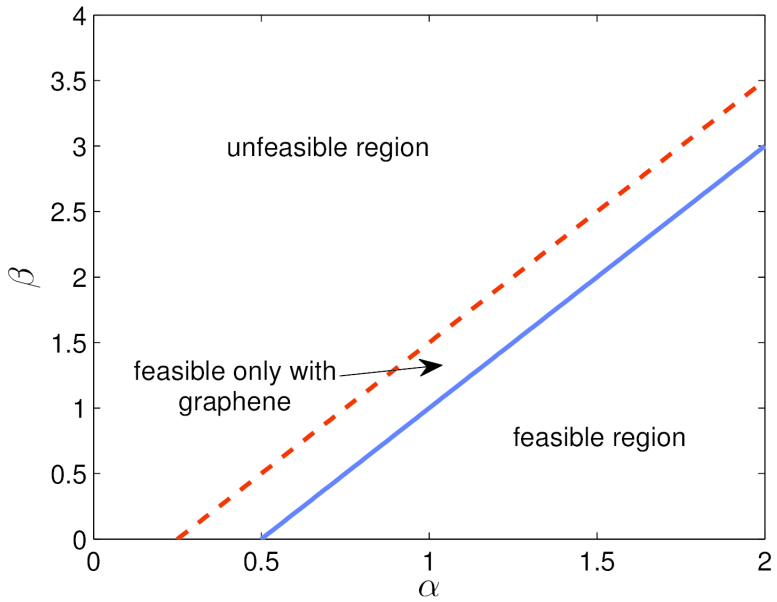

Figure 5.10: Feasible area of the channel capacity as a function of α and β. The blue solid line corresponds to the case in which a metallic antenna is considered, and the red dashed line to a graphenna.

nel capacity does not tend to zero when the network shrinks, i.e., the conditions under which $\lim_{L\to 0} C(L) > 0$. When the feasible regions in the cases of metallic antennas and graphennas are compared, three clearly differentiated regions as a function of α and β are identified, as shown in Figure 5.10:

- The region $\beta - 2\alpha \geq -1/2$ is feasible both when metallic antennas and graphennas are used.
- The region $-1 \leq \beta - 2\alpha < -1/2$ is feasible only when graphennas are used.
- The region $\beta - 2\alpha < -1$ is never feasible.

The following conclusions can be extracted: (i) the quotient P_T/d^2 will be a key parameter in the scalability of GWC, since it will determine the feasibility of the network, (ii) the unique propagation properties of plasmonic EM waves in graphennas yield a larger feasible region as compared to when metallic antennas are used, and (iii) this scalability advantage of graphennas allows a reduction of

the quotient P_T/d^2 up to a factor $\Theta\left(L^{1/2}\right)$ with respect to metallic antennas as the network dimensions shrink.

5.2.4 Scalability guidelines

Several enormous challenges need to be faced by the scientific community when designing wireless communications among nanosystems. First, as it occurs in traditional wireless networks, power consumption is envisaged to become a bottleneck in the performance of GWC networks. Hence, one of these challenges is the fabrication of nanoscale power sources able to provide energy to nanosystems. In this direction, researchers have started working on novel nanomaterials and techniques to create nanobatteries [199], as well as nanoscale energy-harvesting modules [200].

Besides the power source, another important challenge of GWC networks is the expectedly large density of nanosystems required to cover a certain region. Indeed, because of the very limited transmission range of nanosystems, and since the number of nodes N needed to cover a fixed 3-dimensional space scales with their transmission range as $N = \Theta\left(d^{-3}\right)$, it seems likely that a huge number of nodes will be required to build a GWC network. The cost of manufacturing such a large quantity of nanosystems may compromise the feasibility of the network.

With this concern in mind, an additional condition for the network feasibility is established. Besides the constraint introduced in the previous section that the channel capacity does not tend to zero when the network shrinks, i.e., $\lim_{L\to 0} C(L) > 0$, the total number of nanosystems N is restricted to be inversely proportional to the volume of a single nanosystem V, i.e., $N \propto 1/V$. The rationale behind this choice is that, in this scenario, the combined volume of all the nanosystems NV (and thus their cost) will be constant. Since the volume of a nanosystem scales as $V = \Theta\left(L^3\right)$, this condition results in $\Theta\left(d^{-3}\right) = \Theta\left(L^{-3}\right)$. From this expression, the necessary condition for the network feasibility is $d = \Theta(L)$. In other words, all the network dimensions, i.e., the nanosystem size and the transmission distance, must shrink proportionally. Note that the same condition would be obtained assuming a 2-dimensional scenario, where the number of nanosystems is inversely proportional to the area of a single nanosystem.

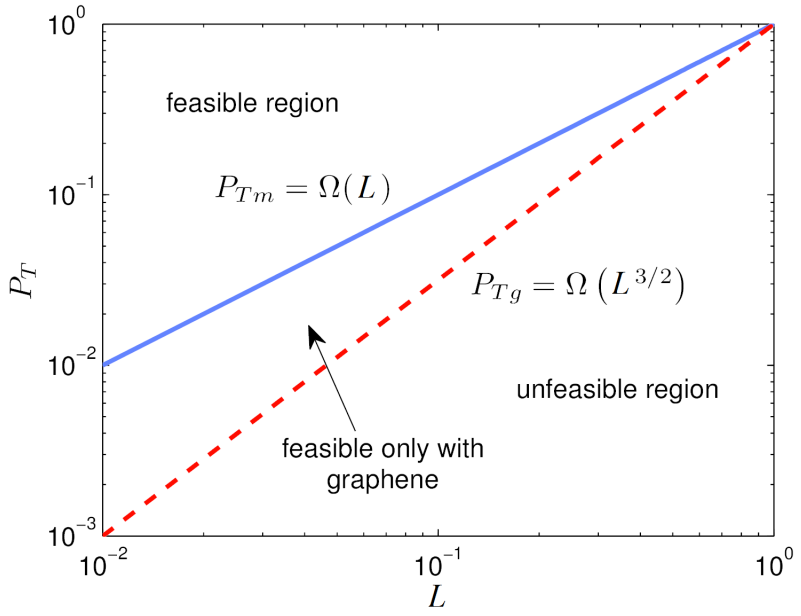

Figure 5.11: Log-log plot comparing the scalability of the transmitted power by a metallic antenna (P_{T_m}, blue solid line), compared to a graphenna (P_{T_g}, red dashed line), as a function of the antenna length L. The transmission distance scales as $d = \Theta(L)$.

In this scenario, which corresponds to $\alpha = 1$, the feasible region of the network corresponds to the values $\beta \leq 1$ when a metallic antenna is considered, and $\beta \leq 3/2$ with a graphenna. In other words, with a metallic antenna, the transmitted power needs to scale at most linearly with the antenna length, as $P_{T_m} = \Omega(L)$; however, graphennas allow a faster decrease in the transmitted power, at a rate $P_{T_m} = \Omega\left(L^{3/2}\right)$. Both cases are compared in Figure 5.11. In consequence, graphennas achieve a scaling advantage of $\Theta\left(L^{1/2}\right)$ with respect to metallic antennas. The following scalability guideline is extracted: the use of graphennas allows relaxing the requirements for nano-batteries and nano-energy harvesting modules that will power nanosystems; for instance, when the antenna size is reduced by two orders of magnitude, the required energy is *one order of magnitude smaller* when using graphennas instead of metallic antennas.

5.3 Summary and concluding remarks

The operation range of graphennas lies in the terahertz range, a frequency band which has not been widely explored for short distances of up to a few meters. In this chapter, two important aspects of the terahertz wireless channel at the very short range are explored.

First, at the small scale of GWC, the phenomenon of molecular absorption will have a key impact on the atmospheric propagation of electromagnetic waves and, in consequence, in the communication performance of GWC. Molecular absorption is analyzed from both the frequency and the time domain, and in particular how its effects scale with respect to the transmission distance. The results show that, on the one hand, for short transmission distances (below one meter), the effects of molecular absorption in the communication performance of GWC are reduced and can in most cases be neglected. On the other hand, for transmission distances greater than a few meters, molecular absorption presents a noticeable impairment in the propagation of terahertz wireless signals and its effects should be considered in order to achieve the target throughput rates of Tbits/s. Moreover, several performance metrics of GWC affected by molecular absorption are evaluated and they are found to show unique scaling trends with respect to traditional wireless communications, with implications in the design of GWC networks. For instance, the results show that in GWC receivers using an energy detection scheme may scale better with respect to the transmission distance than receivers based on amplitude detection.

Second, the scalability of the channel capacity in wireless communications to the nanoscale is analyzed. The focus is set on the unique characteristics of GWC, which affect their performance with respect to traditional wireless communications with minituarized metallic antennas. In this chapter, the impact of three of the novel properties of GWC is identified and analyzed: the propagation of SPP waves in graphennas, molecular absorption and molecular noise. The results show that, while the influence of the two latter effects tends to disappear as the transmission distance shrinks, the unique plasmonic properties of graphennas have a great impact on the channel capacity in GWC. This impact is evaluated both graphically, by plotting quantitative values of the channel capacity as a function

of the antenna length and the transmission distance, and analytically, by computing the limits on the channel capacity when the network size tends to zero. In both cases, the channel capacity is found to scale better as the dimensions shrink when graphennas are used with respect to the case of metallic antennas. By deriving conditions to ensure the *feasibility* of GWC networks, the scalability advantage derived from the use of graphennas is quantified as a function of the transmitted power and the transmission distance.

Finally, guidelines are derived which indicate *how* network parameters need to scale in order to keep the network feasible. Two necessary conditions for the network feasibility are found: (i) the transmission distance needs to scale as $\Theta(L)$, and (ii) the transmitted power needs to scale as $\Omega(L)$ when metallic antennas are used, and as $\Omega\left(L^{3/2}\right)$ when graphennas are used. Therefore, graphennas present a scalability advantage in the transmitted power of $\Theta\left(L^{1/2}\right)$. In other words, when the antenna length is reduced by two orders of magnitude, the required energy is one order of magnitude smaller when using graphennas with respect to the metallic case.

These results provide a general framework for the design of modulations, protocols and architectures for future GWC networks that take advantage of the unique characteristics in the physical channel of GWC, while minimizing its impairments in order to optimize the communication performance of these networks.

Chapter 6

Conclusions and future work

In this thesis, the scalability limits of communication networks to the nanoscale have been explored with the objective of determining the feasibility of wireless communications among nanosystems. The focus has been set in the two main paradigms that have been proposed so far to implement nanonetworks, namely, Diffusion-based Molecular Communication (DMC) and Graphene-enabled Wireless Communications (GWC).

For each of these paradigms, a simple modulation based on the transmission of very short pulses has been defined. Under this modulation scheme and following a general model with as few assumptions as possible, several performance metrics were analyzed. Furthermore, their scalability trends to the nanoscale, i.e., when the system dimensions and the transmission distance tend to zero, were derived.

In the case of DMC, two detection schemes were proposed in Chapter 2: amplitude detection and energy detection. The identified performance metrics were the pulse delay, amplitude and width in the amplitude detection scenario, and the pulse delay, energy and duration in the energy detection case. The scalability of these metrics with respect to the transmission distance d, summarized in Table 6.1, was found to differ significantly from the case of traditional wireless communications.

These results show that DMC networks present novel challenges and principles with respect to traditional wireless networks, as described in Chapter 3. For instance, the amplitude of the transmitted pulses in DMC decreases faster with respect to the transmission distance than in traditional wireless communications,

Performance metric	DMC	Traditional wireless communications
Pulse delay	$\Theta(d^2)$	$\Theta(d)$
Pulse amplitude	$\Theta(1/d^3)$	$\Theta(1/d^2)$
Pulse width	$\Theta(d^2)$	$\Theta(1)$
Pulse energy	$\Theta(1/d)$	$\Theta(1/d^2)$
Pulse duration	$\Theta(d^2)$	$\Theta(1)$

Table 6.1: Scalability of relevant performance metrics in DMC compared to traditional wireless communications, with respect to the transmission distance d.

but their energy does so at a slower pace. Given these results, the proposed energy detection scheme seems the most suitable to combat the high attenuation of the DMC channel. However, even though the pulse width and duration show the same scaling trend with respect to the transmission distance, the value of the pulse duration is always higher than the pulse width in a given scenario. In consequence, the reception of a pulse with energy detection will take a longer time than with amplitude detection. Therefore, in terms of achievable throughput, amplitude detection represents a more advantageous choice than energy detection.

These unique scaling trends of DMC networks will require the design of novel networking protocols and schemes specially adapted to DMC network scenarios. For instance, the high propagation delay of the DMC channel will prevent the use of the common handshake-based synchronization protocols; instead, innovative solutions such as the bio-inspired quorum sensing approach will be needed.

An evaluation of the scalability of these performance metrics in DMC with respect to the nanosystem size would require a profound analysis of the capabilities of the nanosystems themselves. An initial approach considered the process of calcium signaling among living cells [201], a similar communication system occurring in an actual biological scenario. In this scenario, several parameters have been measured, including the molecular concentration inside cells as well as in the extracellular environment, the size of transmitters and receivers, and the average distance among them. This type of study may allow the accurate modeling of an artificial DMC network and the evaluation of its performance. However, despite the advances in synthetic biology, it is still unknown how nanosystems with molecular communication capabilities will be engineered. The design of these en-

Performance metric	GWC	Traditional wireless communications
Resonant frequency	$\Theta\left(1/\sqrt{L}\right)$	$\Theta\left(1/L\right)$
Amplitude of $h(t,d)$	$\Theta\left(1/\sqrt{d}\right)$	$\Theta\left(1\right)$
Width of $h(t,d)$	$\Theta\left(\sqrt[5]{d}\right)$	$\Theta\left(1\right)$
Energy of $h(t,d)$	$\Theta\left(1/\sqrt[3]{d}\right)$	$\Theta\left(1\right)$
Channel capacity	$\Theta\left(L^{3/4}/d\right)$	$\Theta\left(L/d\right)$

Table 6.2: Scalability of relevant performance metrics in GWC compared to traditional wireless communications, with respect to the antenna length L and the transmission distance d.

gineered nanosystems will require the joint work of biologists, chemists, engineers and computer scientists to define their parameters and operating principles. This endeavor, which represents an interesting direction for future work, will allow deriving the scalability of the performance metrics in DMC with respect to the nanosystem size.

Chapter 4 analyzes the physical principles which govern the propagation of SPP waves in graphennas. The study of the unique plasmonic properties of graphene in the terahertz band allows determining the radiation performance of graphennas. Of particular interest is the scalability of the antenna resonant frequency as its size shrinks to the nanoscale. As depicted in Figure 4.20, whereas the resonant frequency of metallic antennas scales inversely proportional to their length, graphennas show a distinct scalability advantage with a resonant frequency which scales inversely proportional to the square root of the antenna length. This result is shown in Table 6.2. In other words, when the antenna size is reduced by a factor of 4, a metallic antenna will resonate at a frequency 4 times higher, whereas the resonant frequency of a graphenna will only increase by a factor of 2. Due to the reduced free-space attenuation for lower frequencies, this property will allow graphennas to reach longer transmission ranges than metallic antennas with the same size.

Furthermore, in Chapter 5, the effects of molecular absorption in the short-range terahertz channel, which corresponds to the expected operating scenario of graphennas, are analyzed. Due to molecular absorption, molecules present in

the standard atmosphere absorb part of the energy of the terahertz EM waves radiated by graphennas, causing impairments in the performance of GWC. The study of the channel impulse response of molecular absorption $h(t, d)$ allows quantifying this loss by deriving several performance metrics, namely, the amplitude, width and energy of the impulse response. A comparison of the scalability of these metrics in GWC with the case of ideal free-space wireless communications (see Table 6.2) shows how the performance of GWC will degrade due to the phenomenon of molecular absorption.

Finally, Chapter 5 includes a study of the scalability of the channel capacity of GWC to the nanoscale. Starting from the Shannon–Hartley theorem, an analytical expression of the channel capacity of GWC is derived and compared to its equivalent in traditional wireless communications. In both scenarios, the channel capacity is found to depend on three key design parameters: the antenna length L, the transmission distance d and the transmitted power P_T. Under the assumption that the transmitted power scales proportionally to the antenna length, i.e., $P_T = \Theta(L)$, the scalability limits of the channel capacity to the nanoscale in GWC and traditional wireless communications are found as $C_g = \Theta\left(L^{3/4}/d\right)$ and $C_m = \Theta\left(L/d\right)$, respectively.

Two main conclusions can be extracted from these results. On the one hand, a key difference in the scalability of the channel capacity with respect to the antenna length is observed. While in both GWC and traditional wireless communications the channel capacity becomes smaller when the antenna shrinks, the capacity reduction in GWC is slower. Therefore, the channel capacity of GWC shows a scalability advantage with respect to traditional wireless communications as the antenna size is reduced. This result is derived from the unique scaling trends observed in the resonant frequency of graphennas due to their novel plasmonic properties in the terahertz band.

On the other hand, as expected, the dependence of the channel capacity on the transmission distance is the same in GWC and traditional wireless communications. Despite the unique properties of the the propagation of SPP waves in graphennas, the wireless propagation of EM waves is analogous in both scenarios, and the effects of molecular absorption and noise tend to disappear when the transmission distance tends to zero.

Naturally, the antenna length is not the only dimension which will affect the performance of GWC networks. Nanosystems are composed of a number of components, such as nano-processor, nano-memory and nano-battery, as shown in Figure 1.1. For instance, tiny supercapacitors have been proposed to implement the energy unit of nanosystems [202]. The energy that can be stored by a supercapacitor scales as a function of its dimensions, which depend on the nanosystem size. Another example concerns the trade-off between readout speed and storage density of memories. Indeed, as the size of memories shrinks to the atomic scale, the data rate at which their information can be read drops dramatically [203]. Therefore, a thorough study of all the components of nanosystems is required to find the scalability trends of GWC as a function of the size of the whole nanosystem. This study is left for future work.

In summary, this thesis examines the scalability of wireless communication networks to the nanoscale. The focus is set in the two main communication paradigms which have been proposed to implement nanonetworks, namely, DMC and GWC. Key performance metrics are defined in each scenario and their scalability as a function of the nanosystem size and the transmission distance is evaluated. These results establish a general framework which may serve designers as a guide to implement wireless communication networks among nanosystems.

Appendix A

N3Sim, a simulation framework for diffusion-based molecular communication

In order to validate the analytical results derived in this thesis, the simulation framework *N3Sim* [204, 205, 206, 207] was used. This tool allows the simulation of DMC networks molecule-by-molecule, with multiple transmitters and receivers suspended in a 3-dimensional fluid medium.

In what follows, Section A.1 briefly describes how a model of DMC is implemented in the simulator and Section A.2 reviews the related work. Section A.3 outlines the architecture of the simulation framework *N3Sim* and Section A.4 describes the collision detection implemented in *N3Sim*. In Section A.5, some sample results are presented in order to illustrate its functionalities. Finally, Section A.6 summarizes this appendix and points to future work directions in this area. The interested reader can find more details about *N3Sim*, as well as a complete user manual and the freely available source code, in the website of the research group N3Cat [208].

A.1 Diffusion-based molecular communication

Diffusion is the process by which particles suspended in a fluid experience a random endless movement. The basic diffusion process is based on Brownian motion, which is due to interactions among the fluid particles and the suspended particles. The microscopic dynamics of this process are extremely complex. It was Einstein in 1905 who first suggested equations to describe this process from a macroscopic point of view. Einstein showed that the concentration of Brownian particles $c(x,t)$ satisfies the diffusion equation:

$$\frac{\partial c(x,t)}{\partial t} = D\frac{\partial^2 c(x,t)}{\partial x^2} \tag{A.1}$$

where $D = K_b T/6\pi R\nu$ is the diffusion coefficient, which depends on the Boltzmann constant K_b, the temperature T, the particle radius R and the fluid viscosity ν. Assuming that Q particles start from the origin at the initial time $t = 0$, the 3-dimensional diffusion equation has the following solution:

$$c(x,t) = \frac{Q}{(4\pi Dt)^{3/2}} e^{-x^2/4Dt} \tag{A.2}$$

The first moment of the particle movement is zero, meaning that the Brownian particle is equally likely to move to the left as it is to move to the right. The second moment, which expresses the mean squared displacement of the Brownian particles, is given by

$$\overline{x^2} = 2Dt \tag{A.3}$$

The same equation can be applied to obtain the displacement in the y and z axes, since each dimension has an independent contribution to the displacement. By means of these equations, the stochastic movement of a particle affected by Brownian motion can be accurately modeled.

Diffusion-based Molecular Communication (DMC), previously introduced in Section 1.3.1, aims to characterize the previously-described scenario of molecular signaling. In DMC, the evolution of the molecular concentration throughout space and time is modeled as a diffusion process. Depending on the scenario, different diffusion models may be used, which can be grouped into two categories: normal

diffusion and anomalous diffusion [39].

On the one hand, *normal diffusion* refers to the case when the movement of the emitted molecules can be modeled by Brownian motion [40], which is valid when viscous forces dominate the motion of the emitted molecules and the interactions among them can be neglected. In this case, the movement of each of the molecules is uncorrelated and the diffusion process can therefore be macroscopically modeled with Fick's laws of diffusion [41].

On the other hand, *anomalous diffusion* appears when interactions among the emitted molecules affect their diffusion process. For instance, in a particular case of molecular signaling known as calcium signaling [36], based on the use of positive-charged calcium ions (Ca^{2+}), the electrostatic forces among these ions impact their diffusion process. Another example of anomalous diffusion includes the case when the concentration of emitted particles is very high and the collisions among them affect their movement, a scenario known as *collective diffusion* [42]. These effects may increase or reduce the displacement of suspended particles, processes known as superdiffusion and subdiffusion, respectively. In these cases, the diffusion process can no longer be modeled by Fick's laws of diffusion and it needs to be analyzed with other methods, such as correlated random walk [43].

The signal propagation in the scenarios of normal diffusion and anomalous diffusion is compared in Section A.5.1.

A.2 Related work

Several authors have developed analytical models of the physical channel of DMC [209, 49, 135, 210]. However, to the best of our knowledge, a validation of these models is missing. In order to validate these theoretical models, either an experimental study or simulations are needed. Despite the latest advances in synthetic biology, an experimental setup of molecular communication is still very challenging to build; consequently, simulation currently seems the most feasible choice. A simulator would allow to recreate an environment of DMC and measure the relevant metrics to evaluate its performance, such as channel attenuation, delay and throughput. The simulator outputs could be then compared with the results from the analytical models in order to assess their validity and to create

novel, more accurate models.

The field of molecular dynamics considers the simulation of the physical movements of atoms and molecules in a given scenario. Molecular dynamics simulators typically consider very accurate models of atoms and molecules and they are highly scalable to run in supercomputers with thousands of computing cores. Some popular simulators include NAMD [211], a parallel molecular dynamics code designed for high-performance simulation of large biomolecular systems; GROMACS [212], able to simulate the Newtonian equations of motion for systems with hundreds to millions of biochemical molecules like proteins, lipids and nucleic acids with complicated bonded interactions and LAMMPS [213], a classical molecular dynamics code that can model atomic, polymeric, biological, metallic, granular, and coarse-grained systems using a variety of force fields and boundary conditions.

Of particular note is the Green's Function Reaction Dynamics (GFRD) algorithm [214], based on the decomposition of the the many-body problem of a reaction-diffusion system into one- and two-body problems that can be solved analytically via Green's functions. These Green's functions are then used to set up an event-driven algorithm which can be up to 5 orders of magnitude faster than using Brownian Dynamics, while modeling the stochastic character of the interactions among particles.

Despite the numerous capabilities and high efficiency of these simulators, they have not been designed with the application of DMC in mind. As a consequence, they are not able to compute fundamental magnitudes from a communication perspective such as signal amplitude, delay, throughput or noise. Therefore, some authors have developed new simulation frameworks specifically oriented for DMC. Several early molecular communication simulators are restricted to very simple scenarios where the transmitter releases a single particle [215, 216]. Moreover, diffusion is only modeled by means of Brownian motion (i.e., only normal diffusion is considered).

Funnycells [217] simulates populations of infected and antibody cells which compete with each other to infect/immunize as many cells as possible by releasing molecules into the environment. The medium is assumed to be sufficiently viscous so that the molecules stay immobile; the diffusion process is not implemented.

NanoNS [218] is an interesting simulation framework which has been built as a module of the well-known network simulator ns-2. This is a useful approach in order to facilitate the future study of the higher layers of a molecular communication network. However, some aspects of NanoNS restrict its applicability to a general case of molecular communication. First, it is based on Fick's laws of diffusion to determine the flux of particles between adjacent volume cells. This is a useful abstraction of the diffusion process, but it does not allow the simulation of anomalous diffusion or other effects, such as the noise due to Brownian motion [135]. Second, NanoNS models the diffusion process and the reception process with a single equation in the simulator algorithm, which makes it difficult to analyze separately these two key processes in a molecular communication system.

Another interesting simulator [63] models a generic set of nanosystems in a given environment. Communication may occur by means of a number of techniques, such as electromagnetic waves or calcium ions. Several configuration parameters allow to recreate different types of biological environments. The mobility model of both nanosystems and information carriers can also be personalized.

N3Sim (available for download at `www.n3cat.upc.edu/n3sim`) is the first open-source simulation framework for DMC which includes both the cases of normal and anomalous diffusion. *N3Sim* has allowed the identification of important properties of DMC [219], the evaluation of modulation techniques and the validation of a physical channel model for DMC [130]. More recently, *N3Sim* enabled the simulation of scenarios of molecular harvesting and resource-constrained DMC [201].

In what follows, a high level overview of *N3Sim*, including a detailed description of the design choices and the implementation of its main features, is provided. Furthermore, simulation results in several simple scenarios are presented to illustrate the capabilities of the simulator.

A.3 Simulator architecture

N3Sim was designed in order to simulate a set of nanosystems which communicate among them through molecular diffusion in a fluid medium [49]. The informa-

tion to be sent by the transmitter nanosystems modulates the rate at which they release molecules, modeled as particles (see Section A.3.2), to the medium. For instance, the transmission of a logical bit '1' may be represented by the emission of a set of particles, and the transmission of a bit '0' by the absence of emission. These emissions create variations in the local concentration of particles, which propagate throughout the medium due to the Brownian motion and to interactions among themselves. The receivers are able to estimate the concentration of particles in their neighborhood by counting the number of particles in a volume around their location. From this measurement, they can decode the transmitted information.

Figure A.1 shows a block diagram of the steps needed to run a simulation. First, the user specifies the values of the simulation parameters in a configuration file. These parameters include the number and location of transmitters and receivers, the signal to be transmitted, the size of the emitted particles and the diffusion coefficient of the medium, amongst others. A script file allows the user to run multiple simulations automatically using only one configuration file, which is useful to easily evaluate the influence of a specific parameter (e.g., the number of transmitted particles) in the system output. Next, the diffusion simulator takes the configuration file and the automation scripts as input, and performs the actual simulation of the DMC scenario. The diffusion simulator computes the position and velocity of each particle in every time step of the simulation. When the simulation ends, its outputs are stored in receiver files (one per receiver), which contain the concentration measured by each receiver as a function of time. Last, another set of scripts may be used to organize the results from several receivers and graphically represent them into a single plot.

A.3.1 Node models

A basic structure in the simulation framework is the *node*. A node is a generic agent which can be specialized into different categories depending on its function within the system. *N3Sim* currently implements three basic node types: transmitters, receivers and harvesters.

The transmitter is defined by its location in the simulation space and its size,

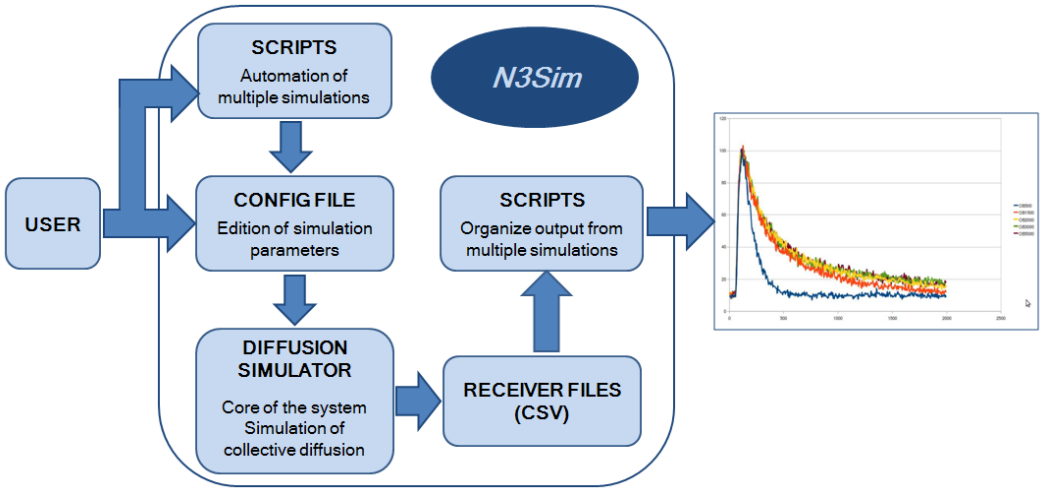

Figure A.1: Block diagram of the simulation framework *N3Sim*.

which determines its influence space (i.e., the region where it may release particles). Every transmitter modulates the information to be sent into an associated waveform, which defines its particle release pattern. This waveform may be chosen among a number of predefined waveforms, such as a square pulse, a Gaussian pulse or a pulse train. A custom waveform may be defined by the user as well.

The receiver can be modeled as a sphere or cube able to measure the instantaneous number of particles within its detection range, from which the local concentration can be estimated. This model is an idealization of the ligand-receptor binding mechanism found in nature [220]. Many receiver parameters are customizable; for instance, after the receiver has detected a group of particles, it can either absorb them or be completely transparent to the particles.

N3Sim also allows the user to place multiple transmitters and receivers in the simulation field, thereby simulating a multipoint-to-multipoint communication. The user just needs to define the characteristics of each transmitter and receiver, namely, its position, shape and size, which can be different for each of them. This allows the study of several communication aspects, such as the feasibility of broadcast molecular communication, or the nature of interferences when more than one transmitter emits at the same time.

Finally, the third type of nodes in *N3Sim* is the harvester node. Molecular harvesters have the ability of collecting molecules from their local neighborhood.

These molecules are then stored into a *molecule reservoir* with a fixed capacity, and they may be used in future transmissions [201]. Three main harvesting methods have been implemented in *N3Sim*:

1. *Standard harvesting* is the basic method, in which a node harvests molecules from the environment at the highest possible rate until the molecule reservoir is full. The reservoir is emptied after an emission of molecules, after which the harvesting operation can resume.

2. *Rate-limited harvesting* requires to specify a harvest rate up to which a node can harvest particles within its reception area. For instance, if a harvester is limited to a 80% rate, only 80% of the molecules present in the neighborhood of the harvester will be collected at each time. This allows controlling the rate at which molecules in the environment will be absorbed due to the harvesting operation.

3. A node using the *unlimited harvesting* method is assumed to have an unlimited reservoir and to harvest every particle within its reception area. Therefore, *unlimited harvesting* can be considered as a special case of the *rate-limited harvesting* with a harvesting rate of 100%.

A.3.2 Particle model

The emitted particles are modeled as indivisible spheres. The main reason for this choice is the simplicity of the collision detection algorithm (see Section A.4) for this shape. Collisions between the emitted particles and the fluid molecules cause them to diffuse throughout the medium. It would be computationally infeasible to model each of these collisions individually, since the number of collisions between each particle and the fluid molecules is in the order of 10^{20} per second [221]. Fortunately, the seemingly random movement of the suspended particles caused by collisions between the particles and the smaller fluid molecules can be mathematically modeled as Brownian motion. Assuming that the particles have no inertia, Brownian motion allows to statistically calculate their movement, which can be modeled as a Gaussian random variable with zero mean and whose root

mean square displacement in each dimension after a time t is $\sqrt{2Dt}$, where D is the diffusion coefficient of the medium [222].

The high-level effect of the particles moving with a Brownian pattern is their diffusion throughout the medium, according to Fick's laws of diffusion [41]. However, Fick's laws do not take into account the influence of interactions among the particles themselves (such as collisions and electrostatic forces), and thus they are only valid when the particle concentration is very low and these interactions are neglected.

In order to simulate environments with anomalous diffusion, which cannot be modeled by Fick's laws of diffusion, *N3Sim* is able to account for the inertia of the emitted particles and the interactions among them. The most relevant interactions which affect the particle diffusion process are collisions and electrostatic forces. For simplicity, collisions among particles are considered elastic (i.e., the total kinetic energy is conserved). Electrostatic forces appear when the emitted particles are ions, which have a non-zero electric charge. Since collisions among particles only have an effect on their diffusion when the concentration is high, and electrostatic forces only appear when the emitted particles have electric charge, both interactions may be disabled in order to increase the speed of the simulation.

A.3.3 Simulation space

N3Sim can be configured to simulate either a 2-dimensional or a 3-dimensional space. One of the parameters of the simulation space is the initial particle concentration in the medium. If it is zero, both a bounded and an unbounded space can be simulated. However, if the initial particle concentration is greater than zero, the simulation space needs to be bounded, in order to avoid having an infinite number of particles.

When a bounded space is simulated, a cuboidal simulation space is assumed where particles rebound on the space limits. This model is considered to be the most realistic for prospective applications of molecular communication. For instance, in a set of communicating nanosystems located in a blood vessel, whenever a particle collides with the vessel wall (known as *tunica intima*), it will rebound. In order to avoid that the particles released by the transmitters cause

Parameter name	Units	Description
time	ns	Total time of the simulation
timeStep	ns	Duration of each time step
boundedSpace	true/false	A rectangular bounded / unbounded space is simulated
xSize	nm	Horizontal size of the simulation space
ySize	nm	Vertical size of the simulation space
bgConcentration	particles/10000 nm^2	Initial background concentration
emitters	integer	Number of emitters in the simulation
emitterRadius	nm	Radius of the influence area of the emitter
emitterType	integer (1 to 5)	Emitter type (determines the emission pattern)
receivers	integer	Number of receivers in the simulation
emitterRadius	nm	Radius of the influence area of the emitter
emitterType	integer (1 to 3)	Receiver type (determines the detection area shape)

Table A.1: Main parameters of *N3Sim*

the background concentration to increase over time, *N3Sim* includes an optional mechanism which lets some particles disappear when they reach the limits of the simulation space, according to the laws of diffusion.

Moreover, objects can also be set within the scenario in order to simulate obstacles between the transmitters and the receivers. This allows recreating, for example, a scenario where a group of bacteria is crossing the medium and it obstructs the way between transmitters and receivers.

Table A.1 outlines some of the most relevant parameters that need to be configured to configure a simulation with *N3Sim*. A complete list of all the simulation parameters and their detailed description can be found in the website `http://www.n3cat.upc.edu/tools/n3sim/ParameterList`

A.4 Collision detection

The problem of detecting collisions between n bodies with random movement is well-known and widely studied in the algorithmic domain. Due to their high computational cost, these algorithms represent a bottleneck in most of the applications that have to implement it.

Besides dealing with the n-body interaction, which is in itself a problem with a computational cost of $O(n^2)$, the problem of collision detection has an additional requirement. Collisions must be solved sequentially in time, since each collision changes the trajectory of the particles involved and may cause new potential collisions. In consequence, the collision detection process is mostly sequential. Since it is not possible to find a collision until the previous one has been solved, it is difficult to parallelize any significant part of the algorithm.

A.4.1 State of the art

A naive solution for the collision detection problem is to iterate through all pairs of objects, testing possible collisions, choosing the first one, solving it, move all particles to the time of this collision and repeat the process until end time is reached. The time complexity of the algorithm is $O(n_c * n^2)$, where n_c is the number of collisions and n is the number of objects. This high computation cost would cause the collision detection algorithm to become a bottleneck for the application performance.

There are algorithms that try to reduce this the computational cost of collision detection by leveraging the temporal and spatial coherence of collisions. Spatial coherence is the property that objects are more likely to collide with other objects in their neighborhood; as a consequence, the number of colliding object pairs at any time is much smaller than the total number of pairs. Temporal coherence means that the particles positions changes relatively little over small time intervals; therefore, calculations from previous frames can be reused to avoid unnecessary recomputation.

A well-known collision detection algorithm is *Baraff's algorithm*, also known as *sweep and prune* [223], which detects collisions *a posteriori*, i.e., after they have occurred. Baraff's algorithm takes advantage of spatial coherence as follows. For

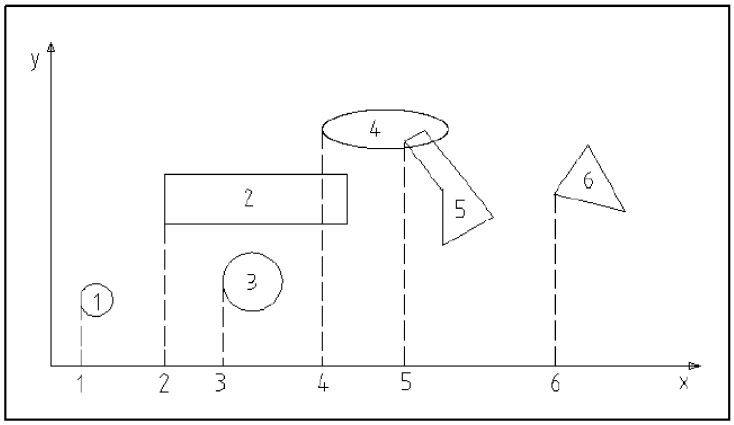

Figure A.2: Schematic description of Baraff's algorithm for collision detection. The position of an object is given by its lowest x coordinate.

each frame, the algorithm first sorts the objects by their lowest x coordinate, as shown in Figure A.2. Then, performing an appropriate iteration over the objects list (each object must be checked with all the others), most of the pairs of objects can be easily dismissed. As it can be seen in Figure A.2, for two objects to overlap (which means they have collided) it is necessary (but not sufficient) that their projections on each axis overlap. When looking for collisions, each object is compared only with the following ones in the sorted list. It is easy to see that, if the current object in consideration does not overlap with a given object, it will not overlap with any of the following objects in the sorted list. This way, a large number of object pairs can be ruled out a priori, saving a significant time.

Baraff's algorithm also takes advantage of the temporal coherence in the following way. After solving the collisions of a frame, the objects list must be sorted again, since objects may have changed their positions. Since the position changes are small, the list will be almost sorted and the sorting algorithm will be more efficient.

A.4.2 Algorithm implemented in N3Sim

The algorithm implemented in *N3Sim* is a variation of Baraff algorithm, which allows using it as an *a priori* algorithm to ensure that no collisions will be missed.

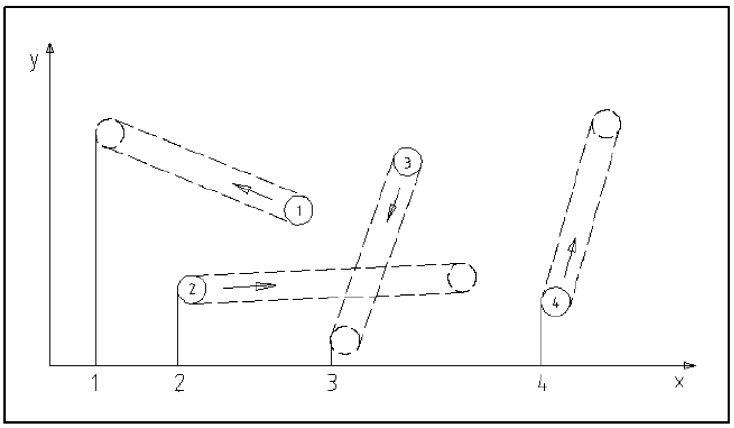

Figure A.3: Schematic description of the algorithm used for collision detection in *N3Sim*. Objects are sorted by the minimum x coordinate of their trajectories.

The modification of Baraff's algorithm has two parts. First, instead of searching the overlap between two objects, the overlap between their trajectories will be considered. Second, it will be necessary to save all possible collisions found, sorted by time, into a data structure in order to take advantage of the temporal coherence.

Figure A.3 shows that for two particles to collide it is necessary (but not sufficient) that the projections of their trajectories overlap on each axis. It follows the same reasoning than Baraff's algorithm, substituting objects by their trajectories.

Following this analogy, the first step is to sort the objects list by the minimum x dimension of their trajectories. As in Baraff's algorithm, each object is tested against the next ones in the list, discarding all of the following when the trajectories of two objects do not overlap. Collisions are stored in a data structure known as collisions queue, sorted by collision time. This way, the cost to obtain the next collision is always $O(1)$.

Once the collisions queue has been created, the algorithm consists in obtaining the next collision and solving it until the queue is empty. Once a collision is solved, one must consider that the trajectories of the objects involved in the collision will have changed. As a consequence, two effects need to be taken into account: first, the objects list will no longer be sorted, and second, the previous collisions involving the objects of the recently solved collision are no longer valid.

To solve the first problem, it is evident that the objects list must be sorted again. As in Baraff's algorithm, an insertion sort algorithm is used because the list is almost sorted (just two objects are unsorted and they are almost at the right position in the list). Regarding the second problem, all collisions involving the objects of the solved collision must be deleted from the collisions queue. Searching through the collisions queue to delete such collisions would have a high time cost; instead, a tag system is used. Each object has a tag, an integer that is incremented each time the object is in a collision that is solved. On the other hand, each collision has two tags, one per object. These tags take the value of the object tag when the collision is created. Then, when a collision is retrieved from the collision queue to be solved, if the collision tags and the object tag do not match, it means that these objects have been in a previous collision; then, the current collision must be discarded and the next one must be solved. Following this procedure, the cost of discarding collisions is $O(1)$.

Finding the new collisions for the objects involved in a collision means to compare the object with the rest of the objects in the sorted list (as it is done in the first part of the algorithm) and to save the new collisions into the collisions queue. The cost of this step is $O(n \log(n))$, $O(n)$ to compare the object with the object in the list and $O(\log(n))$ to save each collision in the collisions queue.

Finally the data structures that store collisions have been modified to improve the memory costs. The problem that leads to these changes was that in simulations of large time steps and high number of collisions there were too many false collisions (collisions with invalid tags as explained in the previous section). These produced that the collisions queue grew too much. To avoid this problem, a list of collisions is associated with each object. This list is deleted and recalculated when a particle has a collision. This way, the memory cost is kept constant.

A.4.3 Cost analysis

This collision detection algorithm implemented in *N3Sim* is summarized in the following table, where n is the number of objects and n_c is the number of collisions:

Stage	Operation	Time cost
1	**Pre-processing**	
1a	Sort objects list	$O(n)$
1b	Create collisions queue	$O(n^2 \log(n))$
2	**Processing**	
2	While collisions queue is not empty	n_c times
2a	Obtain first collision	$O(1)$
2b	Solve collision	$O(1)$
2c	Sort objects list	$O(n)$
2d	Delete invalid collisions	$O(1)$
2e	Find new collisions	$O(n \log(n))$

In conclusion, the total computation cost of the collision detection algorithm for each time step is:

$$C = O(n^2 \log(n)) + n_c O(n \log(n)) \tag{A.4}$$

Similarly to the original Baraff's algorithm, there is a high pre-processing cost of $O(n^2 \log(n))$, but then the cost of detecting each collision is reduced from $O(n^2)$ (for a naive algorithm) to $O(n \log(n))$.

The number of collisions n_c is approximately:

$$n_c \approx O(n \cdot c \cdot t) \tag{A.5}$$

where c is the concentration of particles and t is the simulation time. If a fixed space is considered, the particle concentration is proportional to the number of particles, then

$$n_c \approx O(n \cdot c \cdot t) = O\left(n \cdot \frac{n}{area} \cdot t\right) = O(n^2 \cdot t) \tag{A.6}$$

and

$$C = O(n^2 \log(n)) + n_c O(n \log(n)) = O(n^2 \log(n)) + t \cdot O(n^3 \log(n)) \tag{A.7}$$

The memory cost depends on the number of collisions. As outlined earlier, the number of collisions depends linearly on the number of particles, concentration and time. The relevant time in terms of memory is a time step t_s, which is the time during which the algorithm will store the collisions. Therefore, the memory cost in *N3Sim* has the following expression:

$$C_{mem} = O(n \cdot c \cdot t_s) = O(n^2 \cdot t_s) \tag{A.8}$$

A.4.4 Cost evaluation

Some sample simulations performed to validate the previously calculated expressions of the scalability of collision detection, as a function of the number of particles, are described next. In particular, the computational cost of the collision detection algorithm used in *N3Sim* (explained in Section A.4.2) is compared to a naive algorithm following a brute force approach. The closed simulation space has a square shape, dimensions of 100x100 nm and contains a number of particles ranging from 1000 to 10000, in intervals of 1000 particles. The simulation time is 10 µs. All tests have been performed on an Intel i7-920 CPU with 8 GB of RAM running Java (OpenJDK) version 1.7.0_25 on a Linux kernel version 3.8.0-29. Figure A.4 shows a comparison of the total duration of the simulations as a function of the number of particles present in the environment. As expected, the *N3Sim* collision detection algorithm (blue stars) shows a significant improvement in the simulation time with respect to the naive algorithm (green dots). Moreover, Figure A.4 confirms the scalability advantage of the *N3Sim* algorithm, which improves the cost to detect a collision from $O(n^2)$ (for a naive algorithm) to $O(n \log(n))$.

A.5 Simulation results

As previously mentioned, *N3Sim* can simulate a broad range of scenarios, from very simple ones, consisting of a single receiver and a transmitter which releases defined patterns of particles, to more complex ones containing multiple nodes with particle harvesting capabilities and with different particle release patterns. These

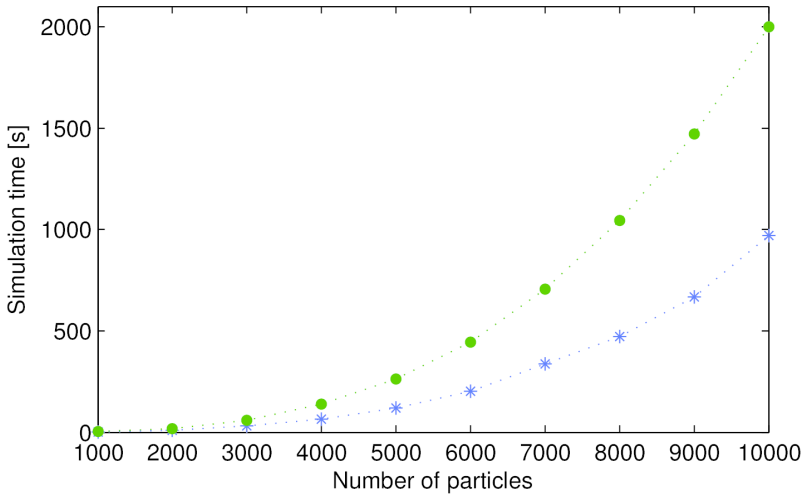

Figure A.4: Comparison of the computational cost of the collision detection algorithm used in *N3Sim* (blue stars) and a brute force approach (green dots) as a function of the number of particles.

scenarios can be run inside a bounded or an unbounded space, with or without a background concentration of particles. In order to illustrate the capabilities of the simulator, the results of several simple simulations of a point-to-point DMC in a 2-dimensional space are shown.

A.5.1 Normal and anomalous diffusion

A simple modulation for DMC is considered, based on the transmission of molecular pulses consisting in the release of a number of molecules at the same time instant [130]. A simulation is performed in which *N3Sim* computes the particle concentration measured by the receiver when a pulse of 10^5 particles is transmitted, with the purpose of comparing the cases of normal diffusion and anomalous diffusion (described in Section 1.3.1). A transmission distance of 50 µm, a receiver radius of 5 µm and a diffusion constant $D = 1$ nm^2/ns are considered.

Figure A.5 shows a scenario of normal diffusion, where interactions among the emitted particles are neglected. When the transmitted signal reaches the receiver location, it is distorted and has a long tail due to the effects of diffusion. As expected in a scenario of normal diffusion, the particle concentration measured

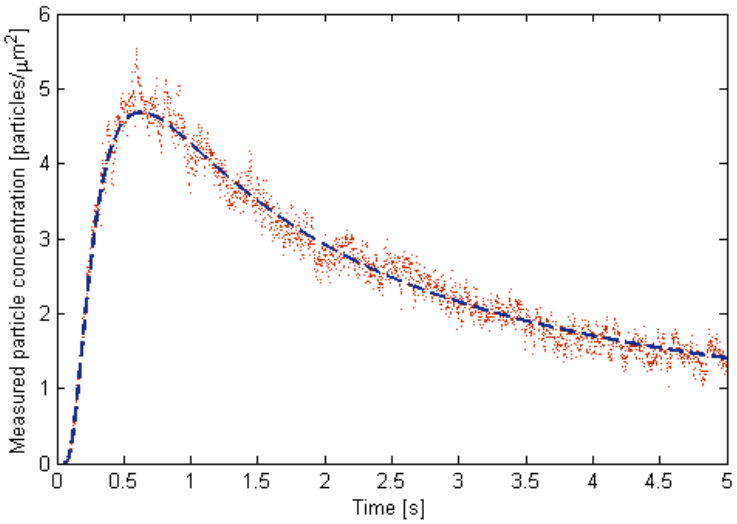

Figure A.5: Received signal when a molecular pulse is transmitted in a scenario of normal diffusion. The red dots show the particle concentration at the receiver as measured by *N3Sim*, and the blue dashed line shows the analytical results of Fick's laws of diffusion.

by the receiver (red dots), matches the analytical result of Fick's laws of diffusion (blue dashed line).

Figure A.6 shows the results of a simulation with the same parameters, but in an environment of anomalous diffusion. In this case, *N3Sim* simulates the collisions among the emitted particles and their inertia. As observed in the figure, the measured particle concentration (red dots) no longer matches the results of Fick's laws of diffusion (blue dashed line). In conclusion, the collisions among the emitted particles and their inertia yield a scenario of superdiffusion, i.e., the particles diffuse faster than predicted by Fick's laws.

A.5.2 Pulse shapes

Figure A.7 shows the transmission of a Gaussian pulse and the received signal, defined as the number of particles detected by a receiver as a function of time, at 500 and 1000 nm from the transmitter location, respectively. A scenario of normal diffusion is considered. As it happened in the previous case, the molecular channel alters the shape of the transmitted pulse. As the transmission distance

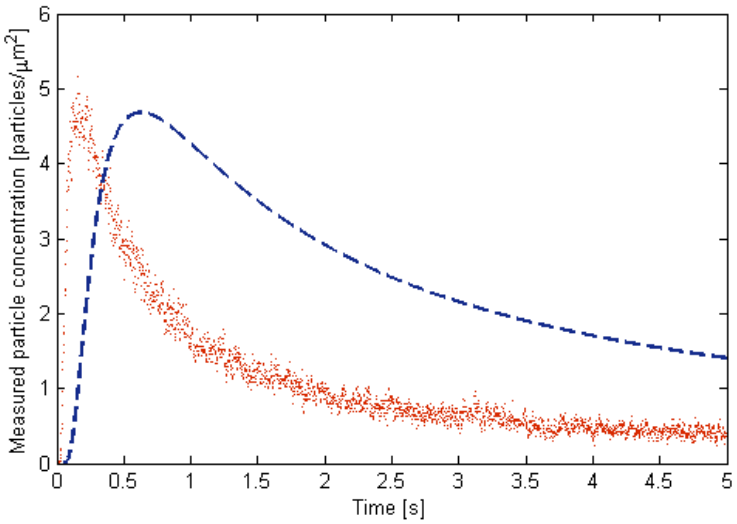

Figure A.6: Received signal when a molecular pulse is transmitted in a scenario of anomalous diffusion. The red dots show the particle concentration at the receiver as measured by *N3Sim*, and the blue dashed line shows the analytical results of Fick's laws of diffusion.

increases, the received pulse has a lower amplitude, a wider shape and a longer tail, due to the effect of diffusion.

Figure A.8 depicts the molecular channel response to a square pulse. In this case, the distortion of the pulse shape by the molecular channel is even more pronounced. At a distance of 1000 nm, the square pulse is indistinguishable from the Gaussian pulse. This suggests that, in this environment, a modulation based on Gaussian pulses might be more suitable than one based on square pulses.

A.5.3 Train of pulses

Using the previously-described pulse-based modulation scheme, a stream of information may be sent by transmitting a train of molecular pulses (e.g., different molecule types may be used to encode bits '0' and '1'). Figure A.9 shows the received signal when a train of pulses is transmitted from a distance of 50 µm, with the same parameters than in the previous simulations. Again, the particle concentration measured by the receiver is plotted as a function of time. Since the DMC channel is linear and time-invariant [219], the received signal corre-

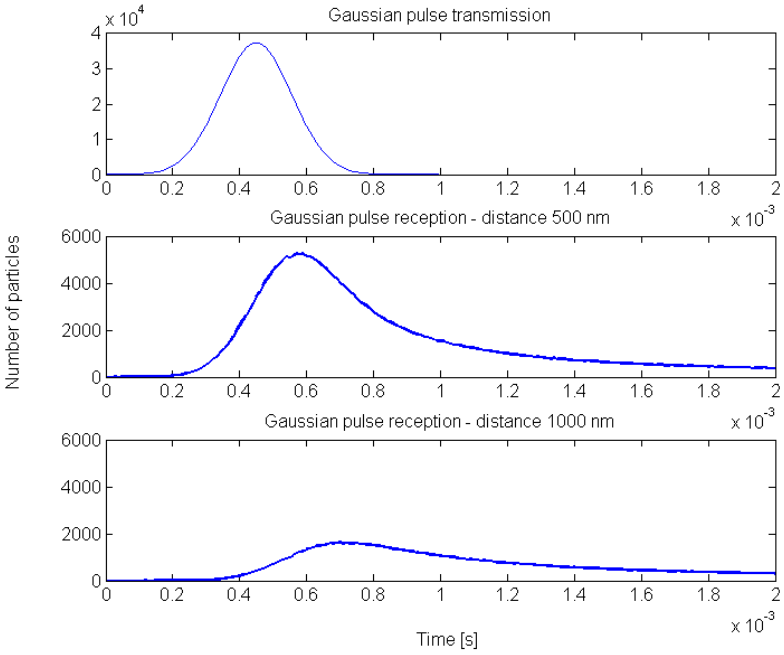

Figure A.7: Transmission of a Gaussian-shaped molecular pulse.

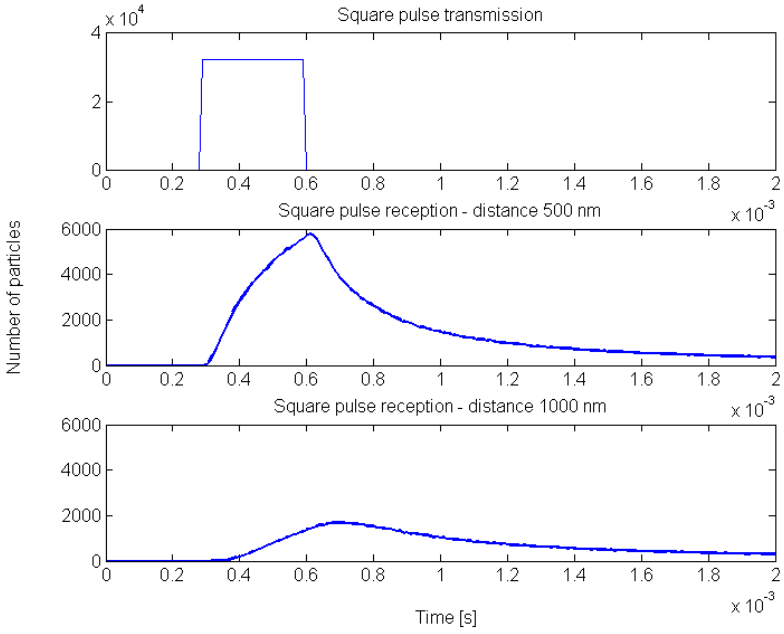

Figure A.8: Transmission of a square-shaped molecular pulse.

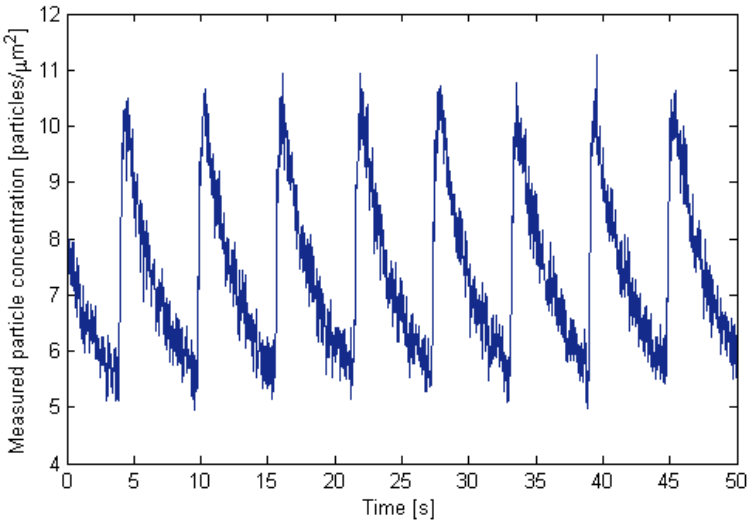

Figure A.9: Received signal when a train of molecular pulses is transmitted, in a scenario of normal diffusion.

sponds to a train of pulses such as that shown in Figure A.5. The minimum time among pulses is determined by the pulse width, which in its turn solely depends on the medium diffusion coefficient and the transmission distance [130]. Therefore, the medium characteristics and the distance between transmitter and receiver nanosystems will ultimately determine the achievable throughput with this modulation scheme.

A.5.4 Molecular harvesting

The implementation of nodes with particle harvesting capabilities is an important feature of *N3Sim*. With their internal reservoirs, harvesting nodes can accumulate particles for future usage. Figure A.10 represents the consecutive charge and drain operations of the particle reservoir of a harvesting node. In this scenario, the harvesting node is continuously capturing particles from the environment during the execution of the simulation using the standard harvesting method. A pulse containing 1000 particles is released whenever the reservoir has enough particles. Figure A.10 shows that the first harvesting operation (corresponding to the first peak) requires a longer charge time than the consecutive harvesting

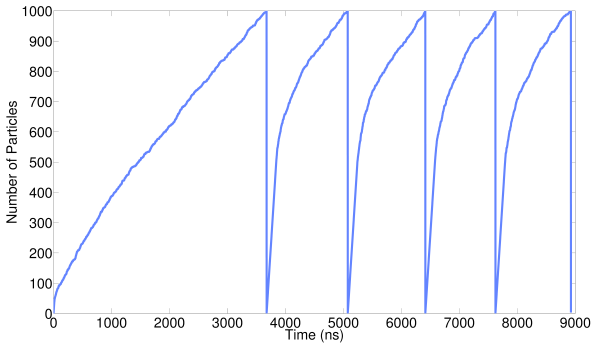

Figure A.10: Charge/drain operations of the reservoir of a harversting node.

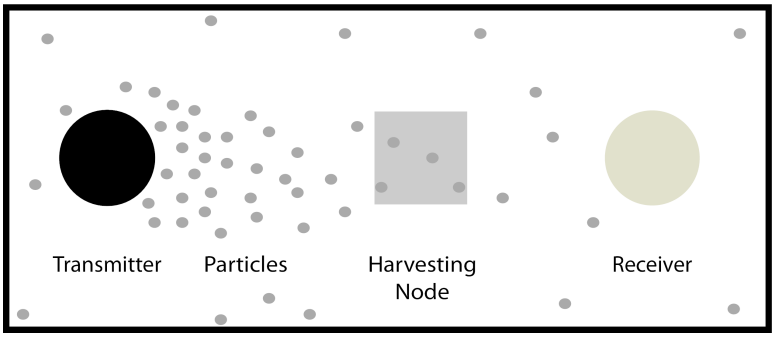

Figure A.11: Schematic diagram of a setup containing a transmitter, a receiver and a harvesting node.

operations. The reason for this behavior is that the following harvesting operations are able to collect remaining particles from the previous pulse transmissions, thereby achieving a higher harvesting rate.

The impact of harvesting operation over the particle reception performance of a distant receiver is an interesting subject which can be easily evaluated using *N3sim*. A basic setup containing a transmitter, a receiver and a harvesting node, as shown in Figure A.11, can be utilized for this purpose. A two-dimensional bounded space is used with dimensions of 5000 nm by 5000 nm. The center-to-center distance between the transmitter and harvester node is 400 nm. Similarly, the distance between the receiver and harvester nodes is also 400 nm. The radius of all three nodes is 100 nm.

In this scenario, how the harvesting operation affects the signal at the receiver location can be measured by observing the maximum number of particles mea-

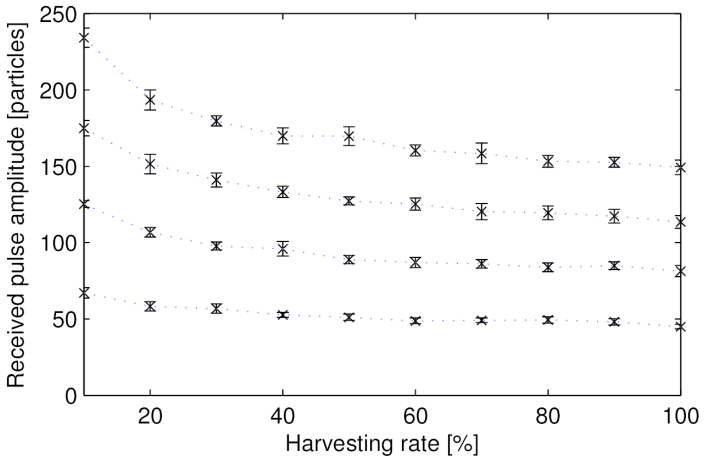

Figure A.12: Amplitude of the signal measured by the receiver, when a molecular pulse with an amplitude ranging from 25000 particles (bottom line) to 100000 particles (top line) is transmitted, as a function of the harvesting rate.

sured by the receiver during the simulation, after a pulse with a given amplitude is transmitted. This metric is illustrated in Figure A.12, which evaluates the reception performance of the receiver when the transmitter emits a pulse with an amplitude ranging from 25000 particles (bottom line) to 100000 particles (top line), in intervals of 25000 particles. The harvesting node collects particles from the environment at a rate ranging from 10% to 100%, in 10% intervals. The averaged results of 10 simulation runs, along with the 95% confidence intervals, show that, independently of the amplitude of the transmitted pulse, increasing the harvesting rate causes the received signal to decrease. This decrease, due to the absorption of part of the transmitted signal by the harvesting node, is particularly significant when the harvesting rate changes from 10% to 40%, after which the amplitude of the received signal remains relatively constant. In any case, there is a trade-off between the received signal and the harvesting rate; higher pulse amplitudes along with low harvesting rates result in the highest signal amplitude at the receiver location.

Figure A.13 shows the same experiment using an *unlimited harvesting* node. Therefore, the observed results are similar with those in the previous simulation for a harvesting rate of 100%. As expected, the signal measured by the receiver increases almost linearly with respect to the amplitude of the transmitted pulses.

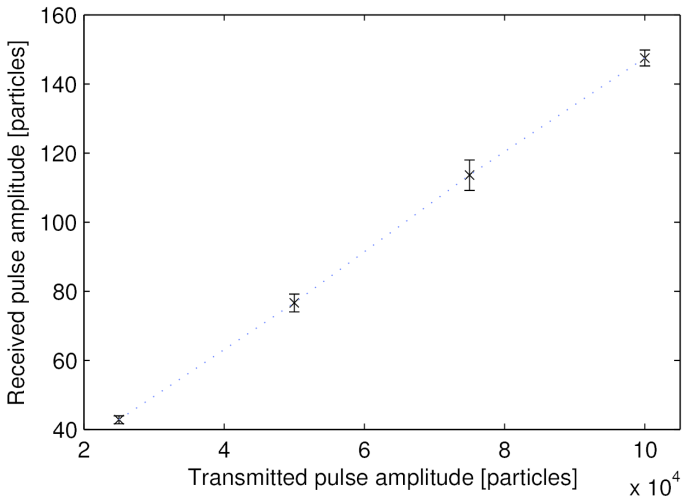

Figure A.13: Amplitude of the signal measured by the receiver, as a function of the transmitted pulse amplitude, when using an unlimited harvesting node.

Next, two important metrics that can be also observed using *N3Sim*, namely, the *maximum pulse frequency* and the *achievable throughput*, are analyzed. The considered scenario in this case is slightly different than that of the previous simulations. In particular, the transmitter node is enhanced with standard harvesting capabilities, so there are two nodes with harvesting capabilities in total. There exists an initial background concentration of particles homogeneously distributed over the bounded simulation space. Having no particles inside its reservoir at the beginning, the transmitting node continuously harvests particles, and emits a pulse of 1000 particles as soon as its reservoir charge reaches this level. Analogously to the scenario depicted in Figure A.11, a harvesting node, using the rate-limited harvesting method, is located between the transmitter and receiver nodes.

In this context, the *maximum pulse frequency* is defined as the number of pulses that the transmitter node can emit per unit of time, which is mainly limited by the rate at which the transmitter is able to harvest particles from the environment. The *achievable throughput* is defined as the number of pulses that are successfully detected by the receiver node per unit of time. The receiver decodes the received pulses by means of amplitude detection [131]; i.e., a pulse is correctly detected if the maximum particle concentration measured by the

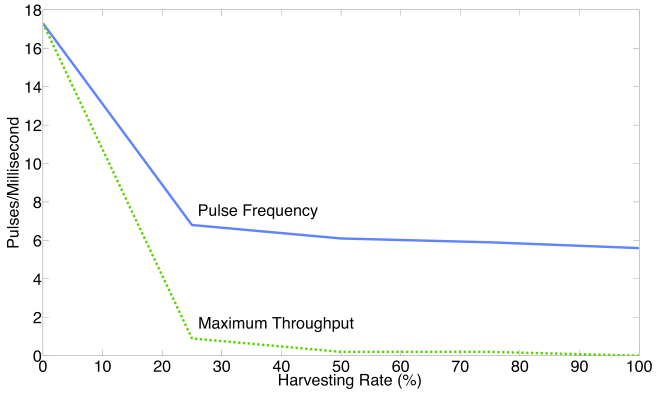

Figure A.14: Maximum pulse frequency at the transmitter (blue solid line) and achievable throughput at the receiver (green dashed line), for different harvesting rates.

receiver exceeds a given threshold. The main difference between these two metrics is that, in some cases, not all transmitted pulses will be correctly detected by the receiver, due to the random diffusion noise or to the absorption of particles by the harvesting node. Therefore, the achievable throughput will always be lower or equal to the maximum pulse frequency.

Figure A.14 shows the maximum pulse frequency of the transmitter (blue solid line) and the achievable throughput as measured by the receiver (green dashed line), as a function of the harvesting rate. The harvesting operation has a devastating impact on both of these metrics, as they sharply decrease when the harvesting rate changes from 0% to 25%. As a consequence, the harvester node should have a low harvesting rate (below 25%) in order to allow for a successful communication in the considered scenario.

A.6 Summary and concluding remarks

N3Sim is a simulation framework which allows the design and evaluation of physical-layer protocols, modulations, resource management schemes and nanosystem components, amongst others, in a DMC scenario. In the considered scenario, transmitters encode the information by releasing particles into the medium, thus causing a variation in their local concentration. The movement of these particles

is modeled as Brownian motion, taking into account their inertia and the interactions among them. Receivers decode the information by sensing the particle concentration in their neighborhood.

Several results of simple simulations of a point-to-point DMC have been shown to illustrate the capabilities of the simulator. Of particular importance is the ability of *N3Sim* to simulate DMC environments with molecular harvesting, where nodes are able to collect molecules from the environment in order to use them in future transmissions.

N3Sim does not scale well to large scenarios with a high background concentration, since it needs to compute the motion and the interactions among every single particle in the simulation space. Therefore, in order to design higher-level protocols (such as MAC or routing schemes) for complex scenarios, there may be the need for a higher-level simulator (which could be integrated into a network simulator, such as ns-3) with a better scalability at the cost of precision. This simulator would not account for every individual particle, but for the distribution of the particle concentration throughout time and space, in a scenario of either normal or anomalous diffusion. A comparison of the computational efficiency of N3Sim with respect to state-of-the-art simulators would also be useful.

Another future research line considers modifying *N3Sim* in order to simulate other scenarios of molecular communication. Examples include medium-range communications based on flagellated bacteria [224, 28], which move following the concentration of attractants diffused in the medium by nanosystems, and taking into account the electrostatic forces among particles.

Appendix B

Derived publications and theses

B.1 Publications derived from this thesis

B.1.1 Journal publications

- I. Llatser, A. Cabellos-Aparicio, E. Alarcón, J. M. Jornet, H. Lee and J. Solé-Pareta, "Scalability of the Channel Capacity of Graphene-enabled Wireless Communications to the Nanoscale", submitted to *IEEE Transactions on Communications*.

- I. Llatser, A. Mestres, S. Abadal, E. Alarcón, H. Lee and A. Cabellos-Aparicio, "Time and Frequency Domain Analysis of Molecular Absorption in Short-range Terahertz Communications", submitted to *IEEE Antennas and Wireless Propagation Letters*.

- I. Llatser, D. Demiray, A. Cabellos-Aparicio, D. T. Altilar and E. Alarcón, "N3Sim: Simulation Framework for Diffusion-based Molecular Communication Nanonetworks", submitted to *Simulation Modelling Practice and Theory (Elsevier)*.

- A. Cabellos-Aparicio, I. Llatser, E. Alarcón, A. Hsu and T. Palacios, "Use of THz Photoconductive Sources to Characterize Graphene RF Plasmonic Antennas", submitted to *Journal of Applied Physics*.

- I. Llatser, A. Cabellos-Aparicio, M. Pierobon and E. Alarcón, "Detection Techniques for Diffusion-based Molecular Communication", to appear in *IEEE Journal on Selected Areas in Communications (JSAC)*.

- I. Llatser, C. Kremers, D. N. Chigrin, J. M. Jornet, M. C. Lemme, A. Cabellos-Aparicio and E. Alarcón, "Radiation Characteristics of Tunable Graphennas in the Terahertz Band", *Radioengineering Journal*, vol. 21, no. 4, pp. 946–953, December 2012.

- I. Llatser, A. Cabellos-Aparicio and E. Alarcón, "Networking Challenges and Principles in Diffusion-based Molecular Communication", *IEEE Wireless Communications*, vol. 19, no. 5, pp. 36–41, October 2012.

- I. Llatser, C. Kremers, A. Cabellos-Aparicio, J. M. Jornet, E. Alarcón and D. N. Chigrin, "Graphene-based Nano-patch Antenna for Terahertz Radiation", in *Photonics and Nanostructures - Fundamentals and Applications*, vol. 10, no. 4, pp. 353–358, May 2012.

- I. Llatser, I. Pascual, N. Garralda, A. Cabellos-Aparicio and E. Alarcón, "N3Sim: A Simulation Framework for Diffusion-based Molecular Communication", *IEEE TC on Simulation Newsletter*, no. 8, pp. 3–4, March 2011.

B.1.2 Conference publications

- I. Llatser, C. Kremers, A. Cabellos-Aparicio, E. Alarcón and D. N. Chigrin, "Comparison of the Resonant Frequency in Graphene and Metallic Nanoantennas", in *AIP Conference Proceedings*, vol. 1475, pp. 143-145, Bad Honnef (Germany), October 2012.

- I. Llatser, S. Abadal, R. Gómez Cid-Fuentes, J. M. Jornet, A. Cabellos-Aparicio, E. Alarcón, J. Solé-Pareta and I. F. Akyildiz, "Prospects of Graphene-enabled Wireless Communications", in *Proc. of GRAPHENE 2012*, Brussels (Belgium), April 2012.

- I. Llatser, C. Kremers, D. N. Chigrin, J. M. Jornet, M. C. Lemme, A. Cabellos-Aparicio and E. Alarcón, "Characterization of Graphene-based Nanoantennas in the Terahertz Band", in *Proc. of the Sixth European Conference*

on Antennas and Propagation (EuCAP), Prague (Czech Republic), March 2012.

- I. Llatser, I. Pascual, N. Garralda, A. Cabellos-Aparicio, M. Pierobon, E. Alarcón and J. Solé-Pareta, "Exploring the Physical Channel of Diffusion-based Molecular Communication by Simulation", in *Proc. of IEEE GLOBECOM*, Houston (USA), December 2011.

- I. Llatser, C. Kremers, A. Cabellos-Aparicio, J. M. Jornet, E. Alarcón and D. N. Chigrin, "Scattering of Terahertz Radiation on a Graphene-based Nano-antenna", in *AIP Conference Proceedings*, vol. 1398, pp. 144–146, Bad Honnef (Germany), October 2011.

- I. Llatser, E. Alarcón and M. Pierobon, "Diffusion-based Channel Characterization in Molecular Nanonetworks", in *Proc. of the 1st IEEE International Workshop on Molecular and Nano Scale Communication (MoNaCom)*, held in conjunction with *IEEE INFOCOM*, Shanghai (China), April 2011.

- S. Abadal, J. M. Jornet, I. Llatser, A. Cabellos-Aparicio, E. Alarcón and I. F. Akyildiz, "Wireless Nanosensor Networks using Graphene-based Nano-Antennas", in *Proc. of GRAPHENE 2011*, Bilbao (Spain), April 2011.

B.2 Co-supervised master theses

- Sergi Abadal, "Cooperative Signal Amplification for Molecular Communication in Nanonetworks". Defended in September 2011.

- Iñaki Pascual, "NanoSim: Simulation Tool for Diffusion-based Molecular Communication in Nanonetworks". Defended in June 2011.

- Nora Garralda, "Simulation-based Evaluation of the Diffusion-based Physical Channel in Molecular Nanonetworks". Defended in April 2011.

References

[1] K. E. Drexler, *Nanosystems: Molecular machinery, manufacturing, and computation*. Wiley, 1992.

[2] R. A. Freitas, "Nanotechnology, nanomedicine and nanosurgery.," *International Journal of Surgery*, vol. 3, pp. 243–6, Jan. 2005.

[3] C. M. J. Pieterse and M. Dicke, "Plant interactions with microbes and insects: from molecular mechanisms to ecology," *Trends in plant science*, vol. 12, pp. 564–9, Dec. 2007.

[4] J. Han, J. Fu, and R. B. Schoch, "Molecular sieving using nanofilters: past, present and future," *Lab on a chip*, vol. 8, pp. 23–33, Jan. 2008.

[5] I. F. Akyildiz and J. M. Jornet, "Electromagnetic wireless nanosensor networks," *Nano Communication Networks*, vol. 1, pp. 3–19, May 2010.

[6] I. F. Akyildiz, F. Brunetti, and C. Blázquez, "Nanonetworks: A new communication paradigm," *Computer Networks*, vol. vol, no. 12, pp. 52no12pp2260–2279, 2008.

[7] I. F. Akyildiz, J. M. Jornet, and M. Pierobon, "Nanonetworks: A New Frontier in Communications," *Communications of the ACM*, vol. 54, p. 84, Nov. 2011.

[8] S. Bush, *Nanoscale Communication Networks*. Artech House, 2010.

[9] S. Luryi, J. Xu, and A. Zaslavsky, "Scaling Limits of Silicon CMOS and Non-silicon opportunities," in *Future Trends in Microelectronics*, pp. 203–211, Wiley, 2007.

[10] I. F. Akyildiz and F. Fekri, "Monaco: fundamentals of molecular nano-communication networks," *IEEE Wireless Communications*, vol. 19, no. 5, pp. 12–18, 2012.

[11] T. Nakano, A. W. Eckford, and T. Haraguchi, *Molecular Communication*. Cambridge University Press, 2013.

[12] "Nano Communication Networks Journal (Elsevier)." `http://www.elsevier.com/wps/locate/nanocomnet`.

[13] "3rd IEEE International Workshop on Molecular and Nano Scale Communication (MoNaCom), held in conjunction with the IEEE International Conference on Communications 2013." `http://monacom.tssg.org/`.

[14] S. C. Goldstein, J. D. Campbell, and T. C. Mowry, "Programmable matter," *Computer*, vol. 38, no. 6, pp. 99–101, 2005.

[15] J. Riu, A. Maroto, and F. X. Rius, "Nanosensors in environmental analysis," *Talanta*, vol. 69, pp. 288–301, Apr. 2006.

[16] C. Li, E. Thostenson, and T. Chou, "Sensors and actuators based on carbon nanotubes and their composites: A review," *Composites Science and Technology*, vol. 68, pp. 1227–1249, May 2008.

[17] P. Tallury, A. Malhotra, L. M. Byrne, and S. Santra, "Nanobioimaging and sensing of infectious diseases," *Advanced drug delivery reviews*, vol. 62, pp. 424–37, Mar. 2010.

[18] H.-Y. Yeh, M. V. Yates, W. Chen, and A. Mulchandani, "Real-time molecular methods to detect infectious viruses.," *Seminars in cell & developmental biology*, vol. 20, pp. 49–54, Feb. 2009.

[19] C. Falconi, A. Damico, and Z. Wang, "Wireless Joule nanoheaters," *Sensors and Actuators B: Chemical*, vol. 127, pp. 54–62, Oct. 2007.

[20] A. Jordan, P. Wust, R. Scholz, B. Tesche, H. Fähling, T. Mitrovics, T. Vogl, J. Cervós-Navarro, and R. Felix, "Cellular uptake of magnetic fluid particles and their effects on human adenocarcinoma cells exposed to AC mag-

netic fields in vitro," *International journal of hyperthermia*, vol. 12, no. 6, pp. 705–22, 1996.

[21] R. Fernández-Pacheco, C. Marquina, J. Gabriel Valdivia, M. Gutiérrez, M. Soledad Romero, R. Cornudella, A. Laborda, A. Viloria, T. Higuera, A. Garcia, J. A. García de Jalón, and M. Ricardo Ibarra, "Magnetic nanoparticles for local drug delivery using magnetic implants," *Journal of Magnetism and Magnetic Materials*, vol. 311, pp. 318–322, Apr. 2007.

[22] I. F. Akyildiz and J. M. Jornet, "The Internet of nano-things," *IEEE Wireless Communications*, vol. 17, no. 6, pp. 58–63, 2010.

[23] "Guardian Angels for a smarter life." `http://www.ga-project.eu`.

[24] S. Abadal, A. Cabellos-Aparicio, J. A. Lázaro, E. Alarcón, and J. Solé-Pareta, "Graphene-enabled hybrid architectures for multiprocessors: Bridging nanophotonics and nanoscale wireless communication," in *ICTON*, 2012.

[25] S. Abadal, E. Alarcón, M. C. Lemme, M. Nemirovsky, and A. Cabellos-Aparicio, "Graphene-enabled Wireless Communication for Massive Multicore Architectures," *IEEE Communications Magazine*, 2012.

[26] M. J. Berridge, "The AM and FM of calcium signaling," *Nature*, vol. 386, pp. 759–760, Feb. 1997.

[27] K. Darchini and A. S. Alfa, "Molecular communication via microtubules and physical contact in nanonetworks: A survey," *Nano Communication Networks*, vol. 4, pp. 73–85, June 2013.

[28] M. Gregori, I. Llatser, A. Cabellos-Aparicio, and E. Alarcón, "Physical channel characterization for medium-range nano-networks using flagellated bacteria," *Computer Networks*, Oct. 2010.

[29] P. Lio' and S. Balasubramaniam, "Opportunistic routing through conjugation in bacteria communication nanonetwork," *Nano Communication Networks*, vol. 3, pp. 36–45, Mar. 2012.

[30] S. Balasubramaniam and P. Lio', "Multi-hop conjugation based bacteria nanonetworks.," *IEEE Transactions on Nanobioscience*, vol. 12, pp. 47–59, Mar. 2013.

[31] M. Gregori, I. Llatser, A. Cabellos-Aparicio, and E. Alarcón, "Physical channel characterization for medium-range nanonetworks using catalytic nanomotors," *Nano Communication Networks*, vol. 1, pp. 102–107, June 2010.

[32] L. Parcerisa and I. F. Akyildiz, "Molecular communication options for long range nanonetworks," *Computer Networks*, vol. 53, no. 16, pp. 2753–2766, 2009.

[33] S. Abadal and I. F. Akyildiz, "Automata modeling of Quorum Sensing for nanocommunication networks," *Nano Communication Networks*, vol. 2, pp. 74–83, Mar. 2011.

[34] S. Balasubramaniam, N. T. Boyle, A. Della-Chiesa, F. Walsh, A. Mardinoglu, D. Botvich, and A. Prina-Mello, "Development of artificial neuronal networks for molecular communication," *Nano Communication Networks*, vol. 2, pp. 150–160, June 2011.

[35] E. Carafoli, "Calcium signaling: a tale for all seasons.," *Proc. of the National Academy of Sciences of the United States of America*, vol. 99, pp. 1115–22, Feb. 2002.

[36] D. E. Clapham, "Calcium signaling," *Cell*, vol. 131, pp. 1047–58, Dec. 2007.

[37] M. Kuran, T. Tugcu, and B. Edis, "Calcium signaling: Overview and research directions of a molecular communication paradigm," *IEEE Wireless Communications*, vol. 19, no. 5, pp. 20–27, 2012.

[38] H. ShahMohammadian, G. G. Messier, and S. Magierowski, "Optimum receiver for molecule shift keying modulation in diffusion-based molecular communication channels," *Nano Communication Networks*, vol. 3, pp. 183–195, Sept. 2012.

[39] L. Vlahos, H. Isliker, Y. Kominis, and K. Hizanidis, "Normal and anomalous diffusion: A tutorial," *Order and Chaos*, vol. 10, no. March 2008, pp. 1–40, 2008.

[40] I. Karatzas and S. E. Shreve, *Brownian motion and stochastic calculus*. Springer, 1991.

[41] J. Philibert, "One and a Half Century of Diffusion: Fick, Einstein, before and beyond," *Diffusion Fundamentals*, vol. 4, no. 6, pp. 1–19, 2006.

[42] A. Ladd, H. Gang, J. Zhu, and D. Weitz, "Time-dependent collective diffusion of colloidal particles.," *Physical review letters*, vol. 74, pp. 318–321, Jan. 1995.

[43] J. Gillis, "Correlated random walk," *Mathematical Proceedings of the Cambridge Philosophical Society*, vol. 51, no. 4, pp. 639–651, 1955.

[44] M. Pierobon and I. F. Akyildiz, "Noise Analysis in Ligand-Binding Reception for Molecular Communication in Nanonetworks," *IEEE Transactions on Signal Processing*, vol. 59, no. 9, pp. 4168–4182, 2011.

[45] T. Suda, M. J. Moore, T. Nakano, R. Egashira, A. Enomoto, S. Hiyama, and Y. Moritani, "Exploratory research on molecular communication between nanomachines," in *Genetic and Evolutionary Computation Conference (GECCO), Late Breaking Papers*, 2005.

[46] A. Einolghozati, M. Sardari, and F. Fekri, "Molecular communication between two populations of bacteria," *2012 IEEE Information Theory Workshop*, pp. 437–441, Sept. 2012.

[47] A. Einolghozati and M. Sardari, "Data gathering in networks of bacteria colonies: Collective sensing and relaying using molecular communication," in *NetSciCom*, 2012.

[48] B. Krishnaswamy, C. Henegar, and J. Bardill, "When Bacteria Talk: Time Elapse Communication for Super-Slow Networks," in *IEEE ICC*, 2013.

[49] M. Pierobon and I. F. Akyildiz, "Information Capacity of Diffusion-based Molecular Communication in Nanonetworks," in *IEEE INFOCOM Mini-conference*, (Shanghai), IEEE, 2011.

[50] B. Atakan and O. B. Akan, "On molecular multiple-access, broadcast, and relay channels in nanonetworks," in *International Conference on Bio-Inspired Models of Network, Information and Computing Sytems*, 2008.

[51] D. Arifler, "Capacity Analysis of a Diffusion-Based Short-Range Molecular Nano-Communication Channel," *Computer Networks*, vol. 55, pp. 1426–1434, Dec. 2011.

[52] A. Einolghozati and M. Sardari, "Capacity of diffusion-based molecular communication with ligand receptors," in *Information Theory Workshop*, 2011.

[53] A. Einolghozati, M. Sardari, and F. Fekri, "Collective sensing-capacity of bacteria populations," in *Information Theory Proceedings (ISIT)*, pp. 437–441, Ieee, Sept. 2012.

[54] K. V. Srinivas, R. Adve, and A. W. Eckford, "Molecular communication in fluid media: The additive inverse gaussian noise channel," *IEEE Transactions on Information Theory*, vol. 58, no. 7, pp. 4678–4692, 2012.

[55] M. Pierobon and I. F. Akyildiz, "Intersymbol and co-channel interference in diffusion-based molecular communication," *IEEE International Conference on Communications (ICC)*, pp. 6126–6131, June 2012.

[56] M. u. Kuran, H. B. Yilmaz, T. Tugcu, and I. F. Akyildiz, "Interference effects on modulation techniques in diffusion based nanonetworks," *Nano Communication Networks*, vol. 3, pp. 65–73, Mar. 2012.

[57] M. u. Kuran, H. B. Yilmaz, T. Tugcu, and B. Özerman, "Energy model for communication via diffusion in nanonetworks," *Nano Communication Networks*, vol. 1, pp. 86–95, June 2010.

[58] N.-R. Kim and C.-B. Chae, "Novel Modulation Techniques using Isomers as Messenger Molecules for Molecular Communication via Diffusion," in *IEEE International Workshop on Molecular and Nanoscale Communications (MoNaCom)*, 2012.

[59] M. u. Kuran, H. B. Yilmaz, T. Tugcu, and I. F. Akyildiz, "Modulation Techniques for Communication via Diffusion in Nanonetworks," in *IEEE International Conference in Communications*, 2011.

[60] A. Guney, B. Atakan, and O. B. Akan, "Mobile ad hoc nanonetworks with collision-based molecular communication," *IEEE Transactions in Mobile Computing*, vol. 11, no. 3, pp. 353–366, 2012.

[61] D. Malak and O. B. Akan, "Molecular communication nanonetworks inside human body," *Nano Communication Networks*, vol. 3, pp. 19–35, Mar. 2012.

[62] L. Felicetti, M. Femminella, and G. Reali, "Establishing digital molecular communications in blood vessels," in *First International Black Sea Conference on Communications and Networking (BlackSeaCom)*, pp. 54–58, Ieee, July 2013.

[63] L. Felicetti, M. Femminella, and G. Reali, "A simulation tool for nanoscale biological networks," *Nano Communication Networks*, vol. 3, pp. 2–18, Mar. 2012.

[64] S. Balasubramaniam, S. Ben-Yehuda, S. Pautot, A. Jesorka, P. Lio', and Y. Koucheryavy, "A review of experimental opportunities for molecular communication," *Nano Communication Networks*, vol. 4, pp. 43–52, June 2013.

[65] I. Llatser, C. Kremers, A. Cabellos-Aparicio, J. M. Jornet, E. Alarcón, and D. N. Chigrin, "Graphene-based nano-patch antenna for terahertz radiation," *Photonics and Nanostructures - Fundamentals and Applications*, vol. 10, pp. 353–358, May 2012.

[66] I. Llatser, C. Kremers, A. Cabellos-Aparicio, J. M. Jornet, E. Alarcón, and D. N. Chigrin, "Scattering of terahertz radiation on a graphene-based nano-antenna," *AIP Conference Proceedings*, vol. 1398, pp. 144–146, 2011.

[67] A. Geim and K. Novoselov, "The rise of graphene," *Nature materials*, vol. 6, pp. 183–91, Mar. 2007.

[68] A. H. Castro-Neto, F. Guinea, N. Peres, K. Novoselov, and A. Geim, "The electronic properties of graphene," *Reviews of Modern Physics*, vol. 81, no. 1, pp. 109–162, 2009.

[69] Y. H. Wu, T. Yu, and Z. X. Shen, "Two-dimensional carbon nanostructures: Fundamental properties, synthesis, characterization, and potential applications," *Journal of Applied Physics*, vol. 108, no. 7, p. 071301, 2010.

[70] M. C. Lemme, T. J. Echtermeyer, M. Baus, and H. Kurz, "A Graphene Field-Effect Device," *IEEE Electron Device Letters*, vol. 28, pp. 282–284, Apr. 2007.

[71] J. Moon, D. Curtis, M. Hu, D. Wong, C. McGuire, P. Campbell, G. Jernigan, J. Tedesco, B. VanMil, R. Myers-Ward, C. Eddy, and D. Gaskill, "Epitaxial-Graphene RF Field-Effect Transistors on Si-Face 6H-SiC Substrates," *IEEE Electron Device Letters*, vol. 30, pp. 650–652, June 2009.

[72] F. Schwierz, "Graphene transistors," *Nature Nanotechnology*, May 2010.

[73] L. Liao, Y.-C. Lin, M. Bao, R. Cheng, J. Bai, Y. Liu, Y. Qu, K. L. Wang, Y. Huang, and X. Duan, "High-speed graphene transistors with a self-aligned nanowire gate," *Nature*, vol. 467, pp. 305–308, Sept. 2010.

[74] Y.-M. Lin, C. Dimitrakopoulos, K. A. Jenkins, D. B. Farmer, H.-Y. Chiu, A. Grill, and P. Avouris, "100-ghz transistors from wafer-scale epitaxial graphene," *Science*, vol. 327, no. 5966, pp. 662–662, 2010.

[75] M. C. Lemme, "Current status of graphene transistors," *Solid State Phenomena*, vol. 156-158, pp. 499–509, 2010.

[76] Y. Wu, Y.-m. Lin, A. A. Bol, K. A. Jenkins, F. Xia, D. B. Farmer, Y. Zhu, and P. Avouris, "High-frequency, scaled graphene transistors on diamond-like carbon," *Nature*, vol. 472, no. 7341, pp. 74–78, 2011.

[77] R. Cheng, J. Bai, L. Liao, H. Zhou, Y. Chen, L. Liu, Y.-C. Lin, S. Jiang, Y. Huang, and X. Duan, "High-frequency self-aligned graphene transistors with transferred gate stacks," *Proceedings of the National Academy of Sciences*, vol. 109, no. 29, pp. 11588–11592, 2012.

[78] T. Palacios, A. Hsu, and H. Wang, "Applications of graphene devices in RF communications," *IEEE Communications Magazine*, vol. 48, pp. 122–128, June 2010.

[79] S. Koswatta, A. Valdes-Garcia, M. Steiner, Y.-M. Lin, and P. Avouris, "Ultimate RF performance potential of carbon electronics," *IEEE Transactions on Microwave Theory and Techniques*, vol. 59, no. 10, pp. 2739–2750, 2011.

[80] X. Yang, G. Liu, A. A. Balandin, and K. Mohanram, "Triple-mode single-transistor graphene amplifier and its applications," *ACS nano*, vol. 4, no. 10, pp. 5532–5538, 2010.

[81] H. Wang, A. Hsu, J. Wu, J. Kong, and T. Palacios, "Graphene-based ambipolar RF mixers," *IEEE Electron Device Letters*, vol. 31, no. 9, pp. 906–908, 2010.

[82] H. Wang, A. Hsu, K. K. Kim, J. Kong, and T. Palacios, "Gigahertz ambipolar frequency multiplier based on cvd graphene," in *2010 IEEE International Electron Devices Meeting (IEDM)*, pp. 23.6.1 –23.6.4, Dec. 2010.

[83] J. Moon, D. Curtis, D. Zehnder, S. Kim, D. Gaskill, G. Jernigan, R. Myers-Ward, C. Eddy, P. Campbell, K. Lee, and P. Asbeck, "Low-Phase-Noise Graphene FETs in Ambipolar RF Applications," *IEEE Electron Device Letters*, vol. 32, no. 3, pp. 270–272, 2011.

[84] Y.-M. Lin, A. Valdes-Garcia, S.-J. Han, D. B. Farmer, I. Meric, Y. Sun, Y. Wu, C. Dimitrakopoulos, A. Grill, P. Avouris, and K. a. Jenkins, "Wafer-scale graphene integrated circuit.," *Science*, vol. 332, pp. 1294–7, June 2011.

[85] P. Avouris, Y. Wu, and W. Zhu, "Graphene devices and semiconductor field effect transistors in 3D hybrid integrated circuits," Jan. 18 2012. US Patent App. 13/352,737.

[86] Y.-M. Lin and J.-B. Yau, "Metal-free integrated circuits comprising graphene and carbon nanotubes," Dec. 27 2012. US Patent 20,120,326,129.

[87] P. Avouris, Z. Chen, and V. Perebeinos, "Carbon-based electronics.," *Nature nanotechnology*, vol. 2, pp. 605–15, Oct. 2007.

[88] J. Perruisseau-Carrier, "Graphene for Antenna Applications: Opportunities and Challenges from Microwaves to THz," in *Loughborough Antennas & Propagation Conference*, 2012.

[89] G. W. Hanson, "Fundamental transmitting properties of carbon nanotube antennas," *IEEE Transactions on Antennas and Propagation*, vol. 53, pp. 3426–3435, Nov. 2005.

[90] P. J. Burke, S. Li, and Z. Yu, "Quantitative theory of nanowire and nanotube antenna performance," *IEEE Transactions on Nanotechnology*, vol. 5, no. 4, pp. 314–334, 2006.

[91] J. M. Jornet and I. F. Akyildiz, "Graphene-Based Nano-Antennas for Electromagnetic Nanocommunications in the Terahertz Band," in *European Conference on Antennas and Propagation*, (Barcelona), 2010.

[92] J. M. Jornet and I. F. Akyildiz, "Graphene-based Plasmonic Nano-antenna for Terahertz Band Communication in Nanonetworks," *IEEE Journal on Selected Areas in Communications*, p. 0, 2013.

[93] M. Tamagnone, J.-S. Gómez-Díaz, J. R. Mosig, and J. Perruisseau-Carrier, "Analysis and design of terahertz antennas based on plasmonic resonant graphene sheets," *Journal of Applied Physics*, vol. 112, no. 11, p. 114915, 2012.

[94] M. Tamagnone, J.-S. Gómez-Díaz, J. R. Mosig, and J. Perruisseau-Carrier, "Reconfigurable terahertz plasmonic antenna concept using a graphene stack," *Applied Physics Letters*, vol. 101, no. 21, pp. 11–14, 2012.

[95] J.-S. Gómez-Díaz and J. Perruisseau-Carrier, "Microwave to THz Properties of Graphene and Potential Antenna Applications," in *International Symposium on Antennas and Propagation*, pp. 239–242, 2012.

[96] L. Ju, B. Geng, J. Horng, C. Girit, M. Martin, Z. Hao, H. a. Bechtel, X. Liang, A. Zettl, Y. R. Shen, and F. Wang, "Graphene plasmonics for tunable terahertz metamaterials," *Nature Nanotechnology*, vol. 6, pp. 630–634, Sept. 2011.

[97] H. Yan, X. Li, B. Chandra, G. Tulevski, Y. Wu, M. Freitag, W. Zhu, P. Avouris, and F. Xia, "Tunable infrared plasmonic devices using graphene/insulator stacks," *Nature Nanotechnology*, vol. 7, no. 5, pp. 330–334, 2012.

[98] I. Crassee, M. Orlita, M. Potemski, A. Walter, M. Ostler, T. Seyller, I. Gaponenko, J. Chen, and A. Kuzmenko, "Intrinsic terahertz plasmons and magnetoplasmons in large scale monolayer graphene," *Nano letters*, vol. 12, no. 5, pp. 2470–2474, 2012.

[99] A. Y. Nikitin, F. Guinea, F. J. Garcia-Vidal, and L. Martin-Moreno, "Surface plasmon enhanced absorption and suppressed transmission in periodic arrays of graphene ribbons," *Physical Review B*, vol. 85, no. 8, p. 081405, 2012.

[100] F. H. L. Koppens, D. E. Chang, and J. García de Abajo, "Graphene plasmonics: A platform for strong light-matter interaction." Aug. 2011.

[101] A. A. Dubinov, V. Y. Aleshkin, V. Mitin, T. Otsuji, and V. Ryzhii, "Terahertz surface plasmons in optically pumped graphene structures.," *Journal of Physics: Condensed Matter*, vol. 23, p. 145302, Apr. 2011.

[102] P. Tassin, T. Koschny, M. Kafesaki, and C. M. Soukoulis, "A comparison of graphene, superconductors and metals as conductors for metamaterials and plasmonics," *Nature Photonics*, vol. 6, pp. 259–264, Mar. 2012.

[103] Z. Fei, A. Rodin, G. O. Andreev, W. Bao, a. S. McLeod, M. Wagner, L. M. Zhang, Z. Zhao, M. Thiemens, G. Dominguez, M. M. Fogler, A. H. Castro-

Neto, C. N. Lau, F. Keilmann, and D. N. Basov, "Gate-tuning of graphene plasmons revealed by infrared nano-imaging," *Nature*, vol. 487, pp. 82–5, July 2012.

[104] B. Wang, X. Zhang, X. Yuan, and J. Teng, "Optical coupling of surface plasmons between graphene sheets," *Applied Physics Letters*, vol. 100, no. 13, p. 131111, 2012.

[105] a. Y. Nikitin, F. Guinea, F. J. García-Vidal, and L. Martín-Moreno, "Edge and waveguide terahertz surface plasmon modes in graphene microribbons," *Physical Review B*, vol. 84, pp. 2–5, Oct. 2011.

[106] T. J. Echtermeyer, L. Britnell, P. Jasnos, A. Lombardo, R. Gorbachev, A. Grigorenko, A. Geim, A. Ferrari, and K. Novoselov, "Strong plasmonic enhancement of photovoltage in graphene," *Nature Communications*, vol. 2, p. 458, 2011.

[107] M. Jablan, H. Buljan, and M. Soljačić, "Plasmonics in graphene at infrared frequencies," *Physical Review B*, vol. 80, pp. 1–7, Dec. 2009.

[108] A. Vakil and N. Engheta, "Transformation optics using graphene," *Science*, vol. 332, pp. 1291–4, June 2011.

[109] C. Gan, H. Chu, and E. Li, "Synthesis of highly confined surface plasmon modes with doped graphene sheets in the midinfrared and terahertz frequencies," *Physical Review B*, vol. 85, no. 12, 2012.

[110] W. L. Barnes, "Surface plasmon-polariton length scales: a route to sub-wavelength optics," *Journal of Optics A: Pure and Applied Optics*, vol. 8, pp. S87–S93, Apr. 2006.

[111] V. Giannini, A. Berrier, S. A. Maier, J. A. Sánchez-Gil, and J. G. Rivas, "Scattering efficiency and near field enhancement of active semiconductor plasmonic antennas at terahertz frequencies.," *Optics express*, vol. 18, pp. 2797–807, Feb. 2010.

[112] I. K. Sendur, O. Karabasoglu, E. A. Baran, and G. Kiziltas, "Optimization of Plasmonic Nano-Antennas," *MRS Proceedings*, vol. 1077, Feb. 2011.

[113] T. Seok, A. Jamshidi, M. Kim, and S. Dhuey, "Radiation engineering of optical antennas for maximum field enhancement," *Nano letters*, vol. 11, pp. 2606–2610, July 2011.

[114] P. Bharadwaj, B. Deutsch, and L. Novotny, "Optical Antennas," *Advances in Optics and Photonics*, vol. 1, p. 438, Aug. 2009.

[115] L. Novotny and B. Hecht, *Principles of Nano-Optics*. Cambridge: Cambridge University Press, 2006.

[116] Y. Huang, L.-S. Wu, M. Tang, and J. Mao, "Design of a Beam Reconfigurable THz Antenna with Graphene-Based Switchable High Impedance Surface," *IEEE Transactions on Nanotechnology*, 2012.

[117] J. Perruisseau-Carrier, M. Tamagnone, J.-S. Gómez-Díaz, and F.-E. Carrasco-Yepez, "Graphene antennas: can integration and reconfigurability compensate for the loss?," in *European Microwave Conference*, 2013.

[118] M. Tamagnone and J.-S. Gómez-Díaz, "High-impedance frequency-agile THz dipole antennas using graphene," in *European Conference on Antennas and Propagation*, no. Eucap, pp. 533–536, 2013.

[119] R. Piesiewicz, C. Jansen, D. Mittleman, T. Kleine-Ostmann, M. Koch, and T. Kurner, "Scattering analysis for the modeling of thz communication systems," *Antennas and Propagation, IEEE Transactions on*, vol. 55, no. 11, pp. 3002–3009, 2007.

[120] R. Piesiewicz, T. Kleine-Ostmann, N. Krumbholz, D. Mittleman, M. Koch, J. Schoebei, and T. Kurner, "Short-Range Ultra-Broadband Terahertz Communications: Concepts and Perspectives," *IEEE Antennas and Propagation Magazine*, vol. 49, pp. 24–39, Dec. 2007.

[121] J. M. Jornet and I. F. Akyildiz, "Channel Modeling and Capacity Analysis for Electromagnetic Wireless Nanonetworks in the Terahertz Band," *IEEE Transactions on Wireless Communications*, vol. 10, no. 10, pp. 3211–3221, 2011.

[122] R. Dennard, F. Gaensslen, V. Rideout, E. Bassous, and a.R. Leblanc, "Design Of Ion-implanted MOSFET's with Very Small Physical Dimensions," *Proceedings of the IEEE*, vol. 87, pp. 668–678, Apr. 1999.

[123] M. Wautelet, "Scaling laws in the macro- , micro- and nanoworlds," *European Journal of Physics*, vol. 22, no. 6, pp. 601–611, 2001.

[124] D. Foty, "Perspectives on scaling theory and CMOS technology - understanding the past, present, and future," in *IEEE International Conference on Electronics, Circuits and Systems*, pp. 631–637, 2004.

[125] P. Gupta and P. R. Kumar, "The capacity of wireless networks," *IEEE Transactions on Information Theory*, vol. 46, no. 2, pp. 388–404, 2000.

[126] O. Lévêque and I. E. Telatar, "Information-Theoretic Upper Bounds on the Capacity of Large Extended Ad Hoc Wireless Networks," *IEEE Transactions on Information Theory*, vol. 51, no. 3, pp. 858–865, 2005.

[127] H. E. Gamal, "On the Scaling Laws of Dense Wireless Sensor Networks: The Data Gathering Channel," *IEEE Transactions on Information Theory*, vol. 51, no. 3, pp. 1229–1234, 2005.

[128] J. Ahn and B. Krishnamachari, "Fundamental Scaling Laws for Energy-Efficient Storage," in *ACM International Symposium on Mobile Ad Hoc Networking and Computing (MobiHoc)*, pp. 334–343, 2006.

[129] A. El Gamal, J. Mammen, B. Prabhakar, and D. Shah, "Optimal throughput-delay scaling in wireless networks - part I: the fluid model," *IEEE Transactions on Information Theory*, vol. 52, pp. 2568–2592, June 2006.

[130] I. Llatser, E. Alarcón, and M. Pierobon, "Diffusion-based Channel Characterization in Molecular Nanonetworks," in *IEEE International Workshop on Molecular and Nanoscale Communications (MoNaCom)*, pp. 467–472, 2011.

[131] I. Llatser, C. Kremers, D. N. Chigrin, J. M. Jornet, M. C. Lemme, A. Cabellos-Aparicio, and E. Alarcón, "Radiation Characteristics of Tunable Graphennas in the Terahertz Band," *Radioengineering*, vol. 21, no. 4, pp. 946–953, 2012.

[132] T. S. Ursell, "The Diffusion Equation. A Multi-dimensional Tutorial," tech. rep., California Institute of Technology, Pasadena, 2007.

[133] W. H. Bossert and E. O. Wilson, "The analysis of olfactory communication among animals.," *Journal of theoretical biology*, vol. 5, pp. 443–69, Nov. 1963.

[134] B. S. Donahue and R. Abercrombie, "Free diffusion coefficient of ionic calcium in cytoplasm," *Cell Calcium*, vol. 8, no. 6, pp. 437–448, 1987.

[135] M. Pierobon and I. F. Akyildiz, "Diffusion-based Noise Analysis for Molecular Communication in Nanonetworks," *IEEE Transactions on Signal Processing*, vol. 59, no. 6, pp. 2532–2547, 2011.

[136] N. Garralda, I. Llatser, A. Cabellos-Aparicio, E. Alarcón, and M. Pierobon, "Diffusion-based physical channel identification in molecular nanonetworks," *Nano Communication Networks*, vol. 2, pp. 196–204, July 2011.

[137] R. M. Corless, G. H. Gonnet, D. E. G. Hare, D. J. Jeffrey, and D. E. Knuth, "On the Lambert W function," *Advances in Computational Mathematics*, vol. 5, pp. 329–359, Dec. 1996.

[138] A. Papoulis and S. U. Pillai, *Probability, random variables, and stochastic processes*. Mcgraw-Hill Publ.Comp, 2002.

[139] I. Llatser, A. Cabellos-Aparicio, and E. Alarcón, "Networking Challenges and Principles in Diffusion-based Molecular Communication," *IEEE Wireless Communications*, vol. 19, no. 5, pp. 36–41, 2012.

[140] R. V. Solé and J. Macia, "Synthetic biocomputation: The possible and the actual," in *European Conference on Artificial Life (ECAL)*, no. 7, pp. 29–36, 2011.

[141] S. Abadal and I. F. Akyildiz, "Bio-Inspired Synchronization for Nanocommunication Networks," in *IEEE GLOBECOM*, pp. 5375–5379, 2011.

[142] S. Abadal, I. Llatser, E. Alarcón, and A. Cabellos-Aparicio, "Cooperative Signal Amplification for Molecular Communication in Nanonetworks," in *IEEE International Workshop on Molecular and Nanoscale Communications (MoNaCom)*, 2012.

[143] N. Tayebi, Y. Zhang, R. Chen, Q. Tran, R. Chen, Y. Nishi, Q. Ma, and V. Rao, "An Ultraclean Tip-Wear Reduction Scheme for Ultrahigh Density Scanning Probe-Based Data Storage," *ACS Nano*, vol. 4, no. 10, pp. 5713–5720, 2010.

[144] S. Jain, K. Fall, and R. Patra, "Routing in a delay tolerant network," *ACM SIGCOMM*, vol. 34, p. 145, Oct. 2004.

[145] M. Miller and B. Bassler, "Quorum sensing in bacteria," *Annual Reviews in Microbiology*, vol. 55, no. 1, pp. 165–199, 2001.

[146] M. J. Moore, T. Nakano, A. Enomoto, and T. Suda, "Measuring Distance From Single Spike Feedback Signals in Molecular Communication," *IEEE Transactions on Signal Processing*, vol. 60, pp. 3576–3587, July 2012.

[147] C. Cetinkaya and F. Orsun, "Cooperative medium access protocol for dense wireless networks," in *The Third Annual Mediterranean Ad Hoc Networking Workshop*, pp. 197–207, 2004.

[148] I. Llatser, C. Kremers, D. N. Chigrin, J. M. Jornet, M. C. Lemme, A. Cabellos-Aparicio, and E. Alarcón, "Characterization of Graphene-based Nano-antennas in the Terahertz Band," in *European Conference on Antennas and Propagation*, 2012.

[149] K. F. Mak, M. Y. Sfeir, Y. Wu, C. H. Lui, J. a. Misewich, and T. F. Heinz, "Measurement of the optical conductivity of graphene.," *Physical review letters*, vol. 101, p. 196405, Nov. 2008.

[150] L. Falkovsky and a. a. Varlamov, "Space-time dispersion of graphene conductivity," *The European Physical Journal B*, vol. 56, pp. 281–284, May 2007.

[151] G. W. Hanson, "Dyadic Greens functions and guided surface waves for a surface conductivity model of graphene," *Journal of Applied Physics*, vol. 103, no. 6, p. 064302, 2008.

[152] N. Peres, R. Ribeiro, and A. H. Castro-Neto, "Excitonic effects in the optical conductivity of gated graphene," *Physical review letters*, vol. 105, no. 5, p. 55501, 2010.

[153] V. Gusynin, S. Sharapov, and J. P. Carbotte, "Magneto-optical conductivity in graphene," *Journal of Physics: Condensed Matter*, vol. 19, p. 026222, Jan. 2007.

[154] Z. Q. Li, E. a. Henriksen, Z. Jiang, Z. Hao, M. Martin, P. Kim, H. L. Stormer, and D. N. Basov, "Dirac charge dynamics in graphene by infrared spectroscopy," *Nature Physics*, vol. 4, pp. 532–535, June 2008.

[155] a. Kuzmenko, E. van Heumen, F. Carbone, and D. van der Marel, "Universal Optical Conductance of Graphite," *Physical Review Letters*, vol. 100, pp. 2–5, Mar. 2008.

[156] P. Sharma, J.-S. Gómez-Díaz, A. M. Ionescu, and J. Perruisseau-Carrier, "Determination of minimum conductivity of graphene from contactless microwaves measurements," in *IEEE International Conference on Nanotechnology*, Ieee, Aug. 2012.

[157] M. Y. Han, B. Ozyilmaz, Y. Zhang, and P. Kim, "Energy band-gap engineering of graphene nanoribbons.," *Physical Review Letters*, vol. 98, p. 206805, May 2007.

[158] L. Falkovsky and S. Pershoguba, "Optical far-infrared properties of a graphene monolayer and multilayer," *Physical Review B*, vol. 76, no. 15, p. 153410, 2007.

[159] N. Rouhi, S. Capdevila, D. Jain, K. Zand, Y. Y. Wang, E. Brown, L. Jofre, and P. J. Burke, "Terahertz graphene optics," *Nano Research*, vol. 5, pp. 667–678, Sept. 2012.

[160] J. Horng, C. Chen, and B. Geng, "Intraband optical transitions in graphene," in *Conference on Lasers and Electro-Optics (CLEO)*, pp. 1–2, 2011.

[161] J.-S. Gómez-Díaz, J. Perruisseau-Carrier, P. Sharma, and A. Ionescu, "Non-Contact Characterization of Graphene Surface Impedance at Micro and Millimeter Waves," *Journal of Applied Physics*, 2012.

[162] S. Mikhailov and K. Ziegler, "Nonlinear electromagnetic response of graphene: frequency multiplication and the self-consistent-field effects," *Journal of Physics: Condensed Matter*, vol. 20, no. i, p. 384204, 2008.

[163] "EM Software and Systems, FEKO." `http://www.feko.info`.

[164] P. Chen and A. Alu, "Atomically thin surface cloak using graphene monolayers," *ACS nano*, no. 7, pp. 5855–5863, 2011.

[165] C. Xu, Y. Jin, L. Yang, J. Yang, and X. Jiang, "Characteristics of electro-refractive modulating based on Graphene-Oxide-Silicon waveguide.," *Optics express*, vol. 20, pp. 22398–405, Sept. 2012.

[166] S. Tongay, K. Berke, M. Lemaitre, Z. Nasrollahi, D. B. Tanner, a. F. Hebard, and B. R. Appleton, "Stable hole doping of graphene for low electrical resistance and high optical transparency.," *Nanotechnology*, vol. 22, p. 425701, Oct. 2011.

[167] P. George, J. Strait, and J. Dawlaty, "Ultrafast optical-pump terahertz-probe spectroscopy of the carrier relaxation and recombination dynamics in epitaxial graphene," *Nano letters*, vol. 8, no. 12, pp. 4248–4251, 2008.

[168] M. Trushin and J. Schliemann, "Anisotropic photoconductivity in graphene," *EPL (Europhysics Letters)*, vol. 96, no. 3, 2011.

[169] J. Hu, X. Ruan, and Y. Chen, "Thermal conductivity and thermal rectification in graphene nanoribbons: a molecular dynamics study," *Nano Letters*, vol. 9, no. 7, pp. 2730–2735, 2009.

[170] V. Ryzhii, M. Ryzhii, and T. Otsuji, "Negative dynamic conductivity of graphene with optical pumping," *Journal of Applied Physics*, vol. 101, no. 8, p. 083114, 2007.

[171] I. Llatser, C. Kremers, A. Cabellos-Aparicio, E. Alarcón, and D. N. Chigrin, "Comparison of the resonant frequency in graphene and metallic nano-antennas," in *AIP Conference Proceedings*, vol. 143, pp. 143–145, 2012.

[172] G. Lifante, *Integrated photonics: fundamentals*. Wiley, 2003.

[173] L. Novotny, "Effective Wavelength Scaling for Optical Antennas," *Physical Review Letters*, vol. 98, pp. 1–4, June 2007.

[174] H. Eisele and G. I. Haddad, "Two-terminal millimeter-wave sources," *Microwave Theory and Techniques, IEEE Transactions on*, vol. 46, no. 6, pp. 739–746, 1998.

[175] E. Brown, J. Soderstrom, C. Parker, L. Mahoney, K. Molvar, and T. McGill, "Oscillations up to 712 ghz in inas/alsb resonant-tunneling diodes," *Applied Physics Letters*, vol. 58, no. 20, pp. 2291–2293, 1991.

[176] O. Momeni and E. Afshari, "High power terahertz and millimeter-wave oscillator design: A systematic approach," *Solid-State Circuits, IEEE Journal of*, vol. 46, no. 3, pp. 583–597, 2011.

[177] R. Köhler, A. Tredicucci, F. Beltram, H. E. Beere, E. H. Linfield, A. G. Davies, D. A. Ritchie, R. C. Iotti, and F. Rossi, "Terahertz semiconductor-heterostructure laser," *Nature*, vol. 417, no. 6885, pp. 156–159, 2002.

[178] G. Scalari, C. Walther, M. Fischer, R. Terazzi, H. Beere, D. Ritchie, and J. Faist, "Thz and sub-thz quantum cascade lasers," *Laser & Photonics Reviews*, vol. 3, no. 1-2, pp. 45–66, 2009.

[179] D. Auston, K. Cheung, and P. Smith, "Picosecond photoconducting hertzian dipoles," *Applied Physics Letters*, vol. 45, no. 3, pp. 284–286, 1984.

[180] C. Berry, N. Wang, M. Hashemi, M. Unlu, and M. Jarrahi, "Significant performance enhancement in photoconductive terahertz optoelectronics by incorporating plasmonic contact electrodes," *Nature communications*, vol. 4, p. 1622, 2013.

[181] J. M. Jornet and I. F. Akyildiz, "Information Capacity of Pulse-based Wireless Nanosensor Networks," in *IEEE SECON*, (Salt Lake City, USA), 2011.

[182] A. Cabellos-Aparicio, I. Llatser, E. Alarcón, A. Hsu, and T. Palacios, "Use of thz photoconductive sources to characterize graphene rf plasmonic antennas," *submitted*, 2013.

[183] D. Liu and J. Qin, "Carrier dynamics of terahertz emission from low-temperature-grown gaas," *Applied optics*, vol. 42, no. 18, pp. 3678–3683, 2003.

[184] C. Dean, A. Young, I. Meric, C. Lee, L. Wang, S. Sorgenfrei, K. Watanabe, T. Taniguchi, P. Kim, K. Shepard, *et al.*, "Boron nitride substrates for high-quality graphene electronics," *Nature nanotechnology*, vol. 5, no. 10, pp. 722–726, 2010.

[185] M. Tani, S. Matsuura, K. Sakai, and S.-i. Nakashima, "Emission characteristics of photoconductive antennas based on low-temperature-grown gaas and semi-insulating gaas," *Applied optics*, vol. 36, no. 30, pp. 7853–7859, 1997.

[186] N. Khiabani, Y. Huang, Y.-c. Shen, and S. Boyes, "Theoretical Modeling of a Photoconductive Antenna in a Terahertz Pulsed System," *IEEE Transactions on Antennas and Propagation*, vol. 61, no. 4, pp. 1538–1546, 2013.

[187] N. Khiabani, Y. Huang, Y.-c. Shen, and S. Boyes, "Time Varying Conductance in THz Photoconductive Antennas," *Terahertz Science and Technology*, vol. 4, no. 3, pp. 116–122, 2011.

[188] I. Llatser, A. Mestres, S. Abadal, E. Alarcón, H. Lee, and A. Cabellos-Aparicio, "Time and frequency domain analysis of molecular absorption in short-range terahertz communications," *submitted*, 2013.

[189] I. Llatser, A. Cabellos-Aparicio, E. Alarcón, J. M. Jornet, H. Lee, and J. Solé-Pareta, "Scalability of the channel capacity of graphene-enabled wireless communications to the nanoscale," *submitted*, 2013.

[190] K. Kawase, Y. Ogawa, Y. Watanabe, and H. Inoue, "Non-destructive terahertz imaging of illicit drugs using spectral fingerprints," *Opt. Express*, vol. 11, no. 20, pp. 2549–2554, 2003.

[191] D. Mittleman, M. Gupta, R. Neelamani, R. Baraniuk, J. Rudd, and M. Koch, "Recent advances in terahertz imaging," *Applied Physics B: Lasers and Optics*, vol. 68, no. 6, pp. 1085–1094, 1999.

[192] A. Nahata, A. S. Weling, and T. F. Heinz, "A wideband coherent terahertz spectroscopy system using optical rectification and electro-optic sampling," *Applied physics letters*, vol. 69, no. 16, pp. 2321–2323, 1996.

[193] A. Markelz, A. Roitberg, and E. Heilweil, "Pulsed terahertz spectroscopy of dna, bovine serum albumin and collagen between 0.1 and 2.0 thz," *Chemical Physics Letters*, vol. 320, no. 1, pp. 42–48, 2000.

[194] W. Wiesbeck, G. Adamiuk, and C. Sturm, "Basic properties and design principles of uwb antennas," *Proceedings of the IEEE*, vol. 97, no. 2, pp. 372–385, 2009.

[195] C. E. Shannon, "The mathematical theory of communication. 1963.," *The Bell System Technical Journal*, vol. 27, pp. 379–423, 623–656, 1948.

[196] J. Proakis and M. Salehi, *Digital communications*. McGraw-Hill, 2008.

[197] A. Goldsmith, *Wireless Communications*. Cambridge University Press, 2005.

[198] S. Verdu, "Spectral efficiency in the wideband regime," *IEEE Transactions on Information Theory*, vol. 48, pp. 1319–1343, June 2002.

[199] F. Vullum and D. Teeters, "Investigation of lithium battery nanoelectrode arrays and their component nanobatteries," *Journal of Power Sources*, vol. 146, pp. 804–808, Aug. 2005.

[200] X. Wang, L. Zhi, and K. Müllen, "Transparent, conductive graphene electrodes for dye-sensitized solar cells," *Nano letters*, vol. 8, pp. 323–7, Jan. 2008.

[201] D. Demiray, A. Cabellos-Aparicio, E. Alarcón, D. T. Altilar, I. Llatser, L. Felicetti, G. Reali, and M. Femminella, "DIRECT : A Model for Molecular Communication Nanonetworks Based on Discrete Entities," *Nano Communication Networks*, 2013.

[202] L. Yuan, X. Xiao, T. Ding, J. Zhong, X. Zhang, Y. Shen, B. Hu, Y. Huang, J. Zhou, and Z. L. Wang, "Paper-based supercapacitors for self-powered nanosystems," *Angewandte Chemie*, vol. 124, no. 20, pp. 5018–5022, 2012.

[203] R. Bennewitz, J. N. Crain, a. Kirakosian, J.-L. Lin, J. L. McChesney, D. Y. Petrovykh, and F. J. Himpsel, "Atomic scale memory at a silicon surface," *Nanotechnology*, vol. 13, pp. 499–502, Aug. 2002.

[204] I. Llatser, I. n. Pascual, N. Garralda, A. Cabellos-Aparicio, and E. Alarcón, "N3Sim: A Simulation Framework for Diffusion-based Molecular Communication," *IEEE TC on Simulation*, no. 8, pp. 3–4, 2011.

[205] I. Llatser, N. Garralda, A. Cabellos-aparicio, M. Pierobon, E. Alarcón, and J. Solé-Pareta, "Exploring the Physical Channel of Diffusion-based Molecular Communication by Simulation," in *IEEE GLOBECOM*, pp. 566–570, 2011.

[206] I. Llatser, D. Demiray, A. Cabellos-Aparicio, D. T. Altilar, and E. Alarcón, "N3Sim: Simulation Framework for Diffusion-based Molecular Communication Nanonetworks," *Simulation Modelling Practice and Theory*, 2013.

[207] I. Llatser, D. Demiray, A. Cabellos-Aparicio, D. T. Altilar, and E. Alarcón, "N3sim: Simulation framework for diffusion-based molecular communication nanonetworks," *submitted*, 2013.

[208] "NaNoNetworking Center in Catalunya." `http://www.n3cat.upc.edu/n3sim`.

[209] A. Goldbeter, G. Dupont, and M. J. Berridge, "Minimal model for signal-induced Ca2+ oscillations and for their frequency encoding through protein phosphorylation," *Proc. of the National Academy of Sciences of the United States of America*, vol. 87, pp. 1461–5, Feb. 1990.

[210] B. Atakan and O. B. Akan, "On Channel Capacity and Error Compensation in Molecular Communication," *Springer Trans. on Computational System Biology*, pp. 59–80, 2008.

[211] J. C. Phillips, R. Braun, W. Wang, J. Gumbart, E. Tajkhorshid, E. Villa, C. Chipot, R. D. Skeel, L. Kalé, and K. Schulten, "Scalable molecular dynamics with namd," *Journal of Computational Chemistry*, vol. 26, no. 16, pp. 1781–1802, 2005.

[212] E. Lindahl, B. Hess, and D. Van Der Spoel, "Gromacs 3.0: a package for molecular simulation and trajectory analysis," *Molecular modeling annual*, vol. 7, no. 8, pp. 306–317, 2001.

[213] S. Plimpton, P. Crozier, and A. Thompson, "Lammps-large-scale atomic/molecular massively parallel simulator," *Sandia National Laboratories*, 2007.

[214] J. S. van Zon and P. R. Ten Wolde, "Green's-function reaction dynamics: A particle-based approach for simulating biochemical networks in time and space," *The Journal of chemical physics*, vol. 123, p. 234910, 2005.

[215] M. J. Moore, T. Suda, and K. Oiwa, "Molecular communication: modeling noise effects on information rate," *IEEE Transactions on Nanobioscience*, vol. 8, pp. 169–80, June 2009.

[216] S. Kadloor and R. Adve, "A Framework to Study the Molecular Communication System," in *International Conference on Computer Communications and Networks*, (San Francisco), 2009.

[217] "Funnycells." `http://www.cse.iitd.ernet.in/~aseth/assg/funnycells/funnycells.html`, 2010.

[218] E. Gul, B. Atakan, and O. B. Akan, "NanoNS: A nanoscale network simulator framework for molecular communications," *Nano Communication Networks*, vol. 1, pp. 138–156, June 2010.

[219] N. Garralda, I. Llatser, A. Cabellos-Aparicio, and M. Pierobon, "Simulation-based Evaluation of the Diffusion-based Physical Channel in Molecular Nanonetworks," in *IEEE International Workshop on Molecular and Nanoscale Communications (MoNaCom)*, pp. 443–448, 2011.

[220] J. P. Rospars, V. Krivan, and P. Lánský, "Perireceptor and receptor events in olfaction. Comparison of concentration and flux detectors: a modeling study.," *Chemical senses*, vol. 25, pp. 293–311, June 2000.

[221] J. Piasecki, "Centenary of Marian Smoluchowski's Theory of Brownian Motion," *Acta Physica Polonica Series B*, vol. 38, no. 5, p. 1623, 2007.

[222] A. Einstein, *Investigations on the theory of the brownian movement*. 1915.

[223] D. Baraff, *Dynamic Simulation of Non-Penetrating Rigid Bodies*. PhD thesis, Computer Science Department, Cornell University, 1992.

[224] M. Gregori and I. F. Akyildiz, "A New NanoNetwork Architecture using Flagellated Bacteria and Catalytic Nanomotors," *IEEE Journal on Selected Areas of Communications*, vol. 28, no. 4, pp. 612–619, 2010.